DYNAMICALLY RECONFIGURABLE OPTICAL BUFFER AND MULTICAST-ENABLED SWITCH FABRIC FOR OPTICAL PACKET SWITCHING

A Dissertation
Presented to
The Academic Faculty

By

Yong-Kee Yeo

In Partial Fulfillment
of the Requirements for the Degree
Doctor of Philosophy in the
School of Electrical and Computer Engineering

Georgia Institute of Technology

May 2007

DYNAMICALLY RECONFIGURABLE OPTICAL BUFFER AND MULTICAST-ENABLED SWITCH FABRIC FOR OPTICAL PACKET SWITCHING

Approved by:

Professor Gee-Kung Chang
School of Electrical and Computer Engineering
Georgia Institute of Technology

Professor John Copeland
School of Electrical and Computer Engineering
Georgia Institute of Technology

Professor John Buck
School of Electrical and Computer Engineering
Georgia Institute of Technology

Professor Rick Trebino
School of Physics
Georgia Institute of Technology

Professor John Barry
School of Electrical and Computer Engineering
Georgia Institute of Technology

Date Approved: 3 November 2006

ACKNOWLEDGEMENTS

I wish to express my gratitude to my thesis advisor, Professor Gee-Kung Chang, for his constant support and guidance. Under his supervision, I have managed to achieve goals that I had previously thought to be beyond my reach. I would also like to thank Dr. Jianjun Yu and the other group members of the Optical Networking Research Group for their assistance in conducting experiments. My appreciation also goes out to the members of the thesis reading committee for spending their valuable time on this dissertation. Finally, I would like to acknowledge the support from my scholarship sponsor, the Agency for Science, Technology and Research (A*Star) of Singapore. Without this scholarship, getting a Ph.D. degree might still be a dream till now.

TABLE OF CONTENTS

LIST OF TABLES

LIST OF FIGURES

LIST OF SYMBOLS

nT	n multiples of the unit time delay T
$S_{x,y}$	Optical ON-OFF reflector y in section x of the folded-path buffer
λ	Optical signal carrier wavelength
P_{in}	Signal optical power at the input of the SOA
I	SOA bias current
s	Number of sections in the folded-path buffer
n	The carrier density in one section of the SOA
n_0	The carrier density at transparency
$g(n,\lambda)$	Parabolic gain model
g_{max}	Maximum gain used for calculating $g(n,\lambda)$
$\Delta\lambda$	Difference between the wavelengths defining the half-gain positions
L	Length of the SOA active region
W	Width of the SOA active region
d	Thickness of the SOA active region
Γ	Optical confinement factor
$n1$	Refractive index of the SOA active region
$n2$	Refractive index of cladding
n_{eff}	Effective index of the guided mode

$\frac{dn1}{dn}$	Differential of *n1* with respect to carrier density
K_0	Intrinsic material loss constant
K_1	Carrier dependent absorption loss constant
A_{rad}	Linear radiative recombination coefficient
B_{rad}	Bimolecular radiative recombination coefficient
A_{nrad}	Linear non-radiative recombination coefficient
C_{aug}	Auger recombination coefficient
$R(n)$	Total recombination rate
R	Input and output facet reflectivity
ν	Optical signal frequency
τ	Lifetime of carriers in the SOA
h	Planck's constant
$P_{SOA,in}$	Average signal input power
N_T	Total number of carriers in the SOA
n_{sp}	Spontaneous noise emission factor
G_s	Device single pass gain
z	Distance along signal propagation direction
α	Material loss coefficient
K_0	Intrinsic material loss in amplifier
K_1	Absorption loss in amplifier
Δf	FWHM laser linewidth
P_{sig}	Optical signal power at receiver

Z	Transimpedance of the pre-amplifier
R_λ	Photodiode responsivity
A_v	Voltage gain of the RF post-amplifier
σ^2_{shot}	Shot noise variance
σ^2_{sig-sp}	Signal-spontaneous beat noise
σ^2_{sp-sp}	Spontaneous-spontaneous beat noise
B_o	Bandwidth of the optical filter at receiver
B_e	Bandwidth of the electrical filter at receiver
L_{recv}	Insertion loss from the variable optical attenuator
L_{fiber}	Total propagation loss in the delay lines and optical couplers
G_0	Unsaturated small signal gain of EDFA
P_{out}	Output power of the EDFA
P_{sat}	EDFA saturation output power
$n_{sp,EDFA}$	EDFA spontaneous emission factor
k	Boltzman's constant
T_{recv}	Operating temperature of the RF amplifier
F_e	Noise figure of EDFA
η_{out}	Output coupling efficiency of the SOA
$\tilde{N}^+_j(L)$	Spontaneous emission photon rate at the SOA output facet
NF^+	Noise figure in the forward direction
$\lambda_{x,y}$	Original wavelength channel y from the input fiber x
$\lambda^k_{x,y}$	Intermediate channel at position k (originally was $\lambda_{x,y}$)

Δz	Unit step along the propagation axis of the SOA
N_s^+	Forward propagation signal photon rates
N_s^-	Backward propagation signal photon rates
β	Wave propagation constant
c_0	Speed of light in vacuum
$\boldsymbol{N_j^+}$	Forward propagating spontaneous noise photon rates the *j*th frequency bin
$\boldsymbol{N_j^-}$	Backward propagating spontaneous noise photon rates the *j*th frequency bin
$\Delta\nu$	Spacing between the noise resonance frequencies

SUMMARY

The metropolitan area networks (MANs) of the future will have to support a large variety of different users with very dissimilar requirements. Large financial institutions require connection-oriented links with the highest security and reliability. On the other hand, corporate customers may want to send and receive high-bandwidth IP-based traffic between different offices, and will therefore require a different set of service level agreements. At the other end of the spectrum, home users that are connected to local ISPs can usually live with the "best effort" delivery of IP packets. Thus, to provide such diverse quality of service (QOS), the network has to set up and dismantle data transmission channels (either virtual or physical) in a highly dynamic manner.

Optical packet switching (OPS) can meet the diverse needs of a wide spectrum of MAN users, and this is because in OPS, the traffic granularity is that of multi-wavelength packets. With such a small granularity, it is easy to provide connection-oriented or connectionless services or even switch between them in a very short span of time. OPS can also be used to bridge the legacy client networks that exist today. IP, ATM and SONET networks can be inter-connected via an OPS network because the bit-rate, modulation format, and the protocol of the optical packet payload are transparent to the optical packet router. Indeed, because of this transparency, the payload can be encoded at very high bit-rates, and therefore, OPS is considered to be a highly scalable solution.

The optical packet router is an important component in the OPS network, and it is responsible for packet routing, protection switching, optical add/drop multiplexing, signal monitoring, and network provisioning. Within the router, there are various sub-components such as the switch fabric, input/output interfaces, optical buffers, as well as electronic control and signaling subsystems. The focus of this research is on the development and characterization of optical buffers and multicast-capable switch fabrics specifically designed for OPS routers.

The optical buffer is a group of delay lines or other optical signal storage media designed to provide either fixed or variable delays for optical signals in the switch. Usually, the delay can be varied by the routing processor when performing packet synchronization, contention resolution, and traffic shaping. Many optical buffering schemes have been developed and they include those that are based on slow-light, re-circulating and feed-forward buffers. Among them, only fiber delay line-based buffers are practically feasible at the moment. However, the physical size of such buffers can become very large if long delay times are required. In this research, a novel optical buffer that is based on a folded-path buffer architecture is proposed. This buffer has the most physically compact design among all the feed-forward buffers, and this is because all the redundant delay lines in the buffer have been eliminated by exploiting the ability of light to propagate bi-directionally in the same fiber without interference.

As a result of the research on folded-path buffers, the concept of a high-speed ON-OFF optical reflector is also introduced for the first time. Although it is derived from optical fiber

loop mirrors that have existed in the literature for a long time, it is different from these passive loop mirrors in that its reflective property is electrically controllable. By adding a very high-speed ON-OFF optical gate constructed using a fast-switching semiconductor optical amplifier (SOA), the mirror is transformed into a controllable ON-OFF optical reflector capable of switching in nanoseconds, and this is a performance criterion required by OPS routers. By incorporating such ON-OFF reflectors in the folded-path buffer, the delay in the buffer is now dynamically reconfigurable, even as the packet is traversing through the buffer. A substantial part of this research is devoted to the study of the ON-OFF reflectors. In particular, simulations and measurements are performed to characterize and optimize the performances of different reflector designs.

The performance of the folded-path buffer architecture is also examined in details. Experiments have been performed to study how the range of delays provided by the buffer can be increased. In addition, multiple sections of the buffer have also been cascaded for measurements to understand its performance when amplified noise accumulates in the buffer. To extend its usefulness, the architecture is also modified so that it can be used for buffering and wavelength conversion at the same time. Such dual-function buffers have not been demonstrated until now, and they will greatly enhance the importance of optical buffers in the OPS router.

The switch fabric of the OLS router is where the space switching of the packets takes place. Optical switch fabrics are used to overcome the limitations imposed by conventional electronic switch fabrics: slow switching speed and non-transparency to the modulation

format and bit-rate of the signals. One of the most important functions of the switch is the capability to broadcast or multicast the input signals to all the output ports. Currently, only fabrics that are based on the broadcast-and-select architectures have the capability to provide truly non-blocking broadcast and multicast services to all input ports at all times. However, a major drawback of these fabrics is that they are implemented using a large number of SOAs, and this result in a very high component count and energy consumption.

In this research, a new multicast-capable switch fabric is proposed. Unlike the traditional broadcast-and-select fabrics, no SOAs are used. Instead, the proposed switch uses a double-stage wavelength conversion scheme based on Four-wave mixing (FWM) in a highly-nonlinear, dispersion shifted fiber, and it is capable of providing strictly-nonblocking broadcast/multicast functionality to all input ports, simultaneously. Experiments have been conducted to study the power penalty imposed on signals as they are switched in this fabric. The gateless switch fabric will also be integrated with the folded-path buffer and a noise reduction technique to improve the integration of these two components will be proposed. Finally, the buffer and switch fabric that are proposed in this thesis are expected to perform at 40 Gbit/s and beyond. In the last part of this research, the performances of these components at high bit-rates will be studied.

Chapter 1 Optical Packet Switching

In this chapter, a short introduction to optical packet switching (OPS) will be given. In particular, the concept of optical label switching (OLS) and the optical packet router will be described in details.

1.1 Introduction to Optical Packet Switching

Ever since the advent of the Internet, data traffic has quickly over taken voice traffic to become the dominant type of information that is being transported by today's high-speed communication networks. Driven by existing applications such as the World Wide Web, Email, video conferencing, and E-commerce as well as emerging applications such as telemedicine, remote instrumentation, virtual reality gaming, and video-on-demand, IP traffic is destined to grow at a phenomenal pace. As the telecommunications industry move towards IP-centric networking model, the importance of IP-over-wavelength-division multiplexing (WDM) will grow as time progresses. IP-over-WDM is an efficient way to carry IP traffic over WDM-enabled optical networks by reducing the number of intermediate networking interfaces between the network layer and the physical layer. Presently, IP-over-WDM can be implemented via the generalized multiprotocol label switching (GMPLS), where it provides circuit switching functionalities at the granularity of a wavelength via optical cross connects (OXC). However, to cater to the requirements of future high bit-rate networks, a smaller

granularity in the form of multi-wavelength packets is needed, and this can be provided by optical packet switching (OPS).

The advantages of using OPS are as follows. First, in an OPS network, the packets are transported entirely in the optical domain without optoelectronic (OE) conversions. At most, only the label or header is converted to electrical signals for routing purposes. This implies that the information carried by the packet payload can be encoded in any format and at any bit-rate. Furthermore, the switching of the packets in a router/switch can be accomplished at very high speed and full transparency. Another consequence is that there is increased scalability and flexibility for future growth. The OPS networking hardware only need slight modification when there is an amendment in the payload bit-rate or modulation format. Second, because the granularity is of the level of multi-wavelength packets, there is increased flexibility for performing tasks such as contention resolution and traffic engineering. Thus, a wide range of services ranging from best effort delivery to dedicated wavelength channels can be provided to different types of customers.

The idea of utilizing a fiber optic network as a transport medium for data packets has been conceptualized as early as 1978 [1]. The introduction of all-optical switching and the concept of self-routing were introduced and experimentally tested in the 1980s. Most of the research conducted then was focused on using orthogonal codes embedded in the bit patterns to route data all-optically [2-5]. From the early 1990s, many large scale projects were undertaken to further explore the feasibility of OPS. These include the DARPA sponsored all-optical network (AON) project [6] , the European RACE Project R2039 ATMOS [7] , the European

Union ACTS KEOPS project [8, 9], the DARPA funded NGI project [10, 11] and most recently the IST-project DAVID funded by the European Commission [12].

In the full implementation of OPS, both the label and payload are processed and routed entirely in the optical domain. The basic impetus is to perform address lookup without resorting to OE conversion of either the label or the header. However, as the execution of complex computations and logical operations using optics and photonics is still relatively difficult, the process of address lookup is replaced by address matching using optical correlators. A set of optical correlators determines whether a packet is destined for a particular switch by correlating the address encoded into the packet with the switch's own address. If there is a match, the payload is extracted and processed. Otherwise, the packet is forwarded to the next switch. Using orthogonal codes, the address may be encoded into the payload bits themselves [2-5] or attached separately as a packet header [13]. Although the utilization of such schemes circumvents electronic label processing, numerous drawbacks are apparent. The length, format and bit-rate of the label cannot be readily changed once a particular type of decoding scheme is chosen. This is due to restrictions imposed by the optical label decoding hardware. Consequently, this makes standardization of the label format difficult, and it also limits the upgradability of the labeling scheme. Moreover, the lack of electronic processing capabilities implies that more complex algorithms cannot be used to perform traffic engineering or resolve contentions in the switch efficiently. These problems can be easily solved with optical label switching (OLS).

1.2 Optical Label Switching

Optical Label Switching (OLS) can be considered to be a particular implementation of OPS. It is conceived to integrate optical circuit, burst and packet switching by taking advantage of the small traffic granularity of optical packets and the flexibility and functionalities provided by the optical labels. Like OPS, only the packet label/header is processed for routing purposes; the payload remains in optical form throughout its lifespan in the OLS network. Using OLS, increased functionalities can be incorporated into the label, and this facilitates the future integration of other protocols such as MPLS with OPS. Another advantage of using OLS is that existing legacy client networks such as those based on SONET and ATM can integrate with the IP-over-WDM model more easily. Figure 1 depicts a hypothetical OLS network interconnecting legacy client networks and a backbone wide area network (WAN).

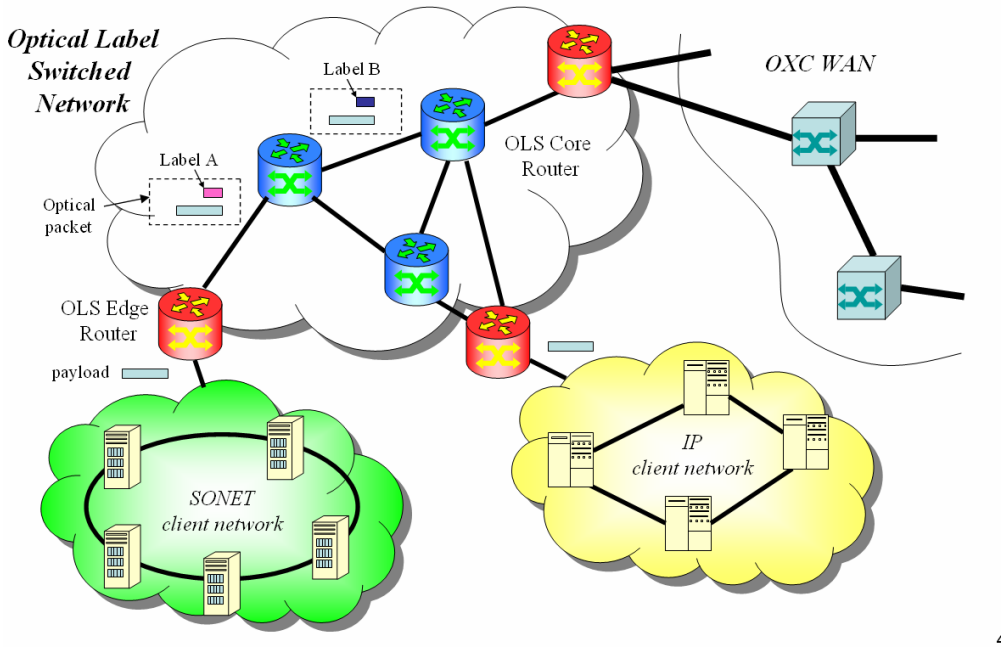

Figure 1. Hypothetical OLS network with connections to OXC WAN and client networks based on SONET and IP.

The OLS edge router's tasks include attaching or detaching a label to the client network's data, buffering, and routing in the electronic domain. Within the OLS network, the OLS core router only processes the label; the content of the payload is transparent to the router, and it can be in any format, for example, ATM cells or IP packets. At the edge of the OLS network, a special router can also be used as an interconnection to the backbone WAN. This edge router can also perform label stacking in order to connect to a different label-switched network.

1.3 Generic Core Router in a OLS Network

The primary function of the core router is to route the packets to their correct destinations. This typically involves the following steps:

1. Extraction of label from packet
2. Processing of the label to obtain routing information
3. Routing of the payload and resolve contention if necessary
4. Rewriting of the label and recombining it with the routed payload

A generic architecture of a core router that can perform these functions is shown in Figure 2. The input interface is where the optical signal enters the router, and usually if the input fibers are carrying wavelength-division-multiplexed (WDM) signals, wavelength de-multiplexers (DEMUX) can be positioned at the input interface to separate the incoming signals into discrete wavelength channels. Depending on the network requirements, the optical 3R (Re-

amplification, retiming, and reshaping) [14] process may also be applied to the input signal at this point.

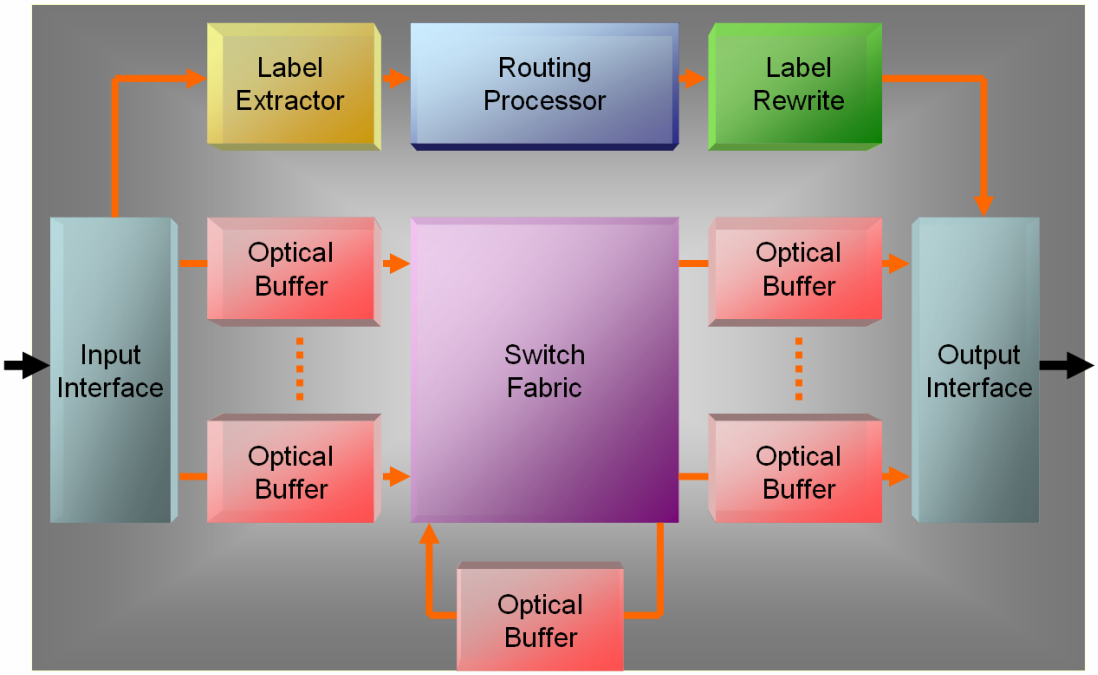

Figure 2. A generic architecture of an OLS core router.

The input interface also contains the components that are used to extract the optical label from the packet. After the label is extracted, it is usually optically erased, and the detached payload will proceed to the buffer and switch fabric. The extracted label is converted to electronic signals to obtain information such as the packet's destination address, its payload information, and its priority level. This information is then processed by the routing processor to determine which output port the payload should be switched to and when the switching should occur. If two or more packets are destined for the same port, the optical buffers will be used to temporarily store some of these packets until the contention is resolved. The routing processor will vary the delay of the buffers to ensure the packets can be

switched to their desired output ports and that none of the packets will get dropped in the worst case scenario.

The switch fabric receives commands from the routing processor on when and how to reconfigure itself. The routing processor's function is critical because it has to coordinate the timing between the different switching events in various components to ensure an error-free propagation path for the payload as it travels within the router; the switch fabric role here is passive as it merely transports the payload from its input port to its output port. Nevertheless, the switch fabric has to reconfigure itself in several nanoseconds as it is anticipated that individual optical packets as small as a few tens of nanoseconds may pass through the optical router.

After the payload is physically switched, it may be buffered again if the router at the next hop is busy. Otherwise, it will proceed to the output interface where a new label will be attached. After this, the new packet is ready to leave the router. However, sometimes it may be necessary to regenerate the packet before it makes an exit. Usually, it is the payload that requires this regeneration because severe signal degradations can occur in the buffers and the switch fabric. On the other hand, since the label is newly written, it does not require regeneration.

It can be seen that the routing processor has many tasks to perform. To summarize, its primary responsibilities comprise the following:

1. Label processing
2. Address lookup
3. Making a routing decision
4. Computing a new label
5. Controlling the buffer delay
6. Controlling the switch fabric
7. Instructing the label writer to attach a new label
8. Coordinating the switching and communication between different components

1.4 Optical Labeling Schemes

In optical label switching, the generation, processing, and rewriting of the label are some of the many challenges that must be overcome. The requirements for label generation are efficiency, scalability and flexibility. This means that the label generation process should not introduce too much latency and impose restrictions on the bit-rate and modulation format of both the label and the payload. The label rewriting process must also satisfy these requirements. Once the packet is in the network, the label and payload will be subjected to signal impairments such as crosstalk, fiber nonlinearities, and amplified spontaneous emission (ASE) noise. The labeling scheme that is chosen should not make the packet more susceptible to such impairments. Labeling schemes can be categorized by the way the label is differentiated from the payload. Diversities in time, wavelength and modulation format have been utilized by various researchers [15-34]. In general, they share a common characteristic:

the label is usually encoded at a lower bit-rate compared to the payload. The intention is to simplify OE conversions during the label extraction and rewriting process.

When the label and payload are differentiated by their time of arrival at the router, this is known as the time-serial labeling scheme. Thus, the label becomes the packet header and it precedes the payload by a guard time. Unlike the other labeling schemes, this guard time must be strictly maintained as the packet travel across the OPS network. Precise timing control is thus required during the header processing and rewriting operations, and this necessitates the use of a large number of optical and electronic delay buffers. The concept of using a low bit-rate header and a high bit-rate payload first appeared in [15]. Recently, packets with 10 Gbit/s header and 160 Gbit/s payload have also been reported by another group of researchers [16]. In all these time-serial labeling schemes, the speed of the header processing operation becomes a performance limiting factor, and it has direct influence on the header bit-rate and the amount of guard time required. To increase the header processing efficiency, methods such as a serial-to-parallel converter [17] and an optical digital-to-analog converter [18] are proposed. However, these methods assume that the header is of a particular bit-rate, size or modulation format, and this imposes limitations in terms of scalability.

For the labeling schemes using modulation format diversity, the label and payload are encoded using different formats and they are superimposed in time domain. Such a technique has been demonstrated in an earlier experiment to allow packet and circuit switching to coexist in the same optical network [19]. In OLS, this technique is sometimes known as

orthogonal labeling, and it allows the label and payload to be processed asynchronously, but does not require them to exist on separate wavelengths. In practical implementations, the label is usually extracted first followed by the payload. Different combinations of modulation formats have been reported: Intensity modulated (IM) payload with frequency shift keying (FSK) label [20, 21], IM payload with differential phase shift-keying (DPSK) label [22], dc-balanced-line-coded ASK payload with ASK label [23], IM payload with FSK label [24], FSK payload and IM label [25],and polarization-shift-keying modulated label and ASK payload [26]. The label extraction method is uniquely different for each combination but usually additional signal processing is required to remove the label before the payload can be extracted. In contrast, schemes using wavelength diversity only require a simple optical filter to separate the label and payload. A common problem with these modulation format-diversified labeling schemes is that a compromise has to be made between the extinction ratio of the label and the bit-rate or extinction ratio of the payload. Moreover, crosstalk between label and payload is also a problem that needs to be addressed.

In wavelength diversity schemes, the payload and label are differentiated by the position of their optical spectra. Two commonly used techniques are the out-of-band labeling [27, 28] and in-band labeling [29, 30]. In the former, the carrier frequencies of the label and payload are in separate wavelength channels whereas in the latter, they are closer to one another, occupying the same wavelength channel. In both schemes, the label and payload can be easily separated using optical filtering and they can be processed asynchronously. However, out-of-band labeling uses more bandwidth and dispersion in the fiber causes walk-off between label and payload. These problems can be mitigated using the in-band labeling

schemes. Initially, double sideband (DSB) sub-carrier multiplexing (SCM) is used to place the label at subcarrier frequencies while the payload occupies the baseband frequencies [29, 30]. However, this resulted in the label being subjected to the RF fading effect and the received power of the label varies periodically with transmission distance [29, 30]. Various methods have been proposed to avoid this problem: single sideband (SSB) SCM [31, 32], carrier suppression before detection [33], and optical carrier suppression and separation (OCSS) [34].

Due to the diversity of the labeling schemes, numerous label erasure techniques have been published. The reader is advised to refer to [35] for a review of these techniques. The packet label is usually erased before the payload proceeds to the switch fabrics, and when the payload is about to exit from the router, a new label is attached.

1.5 Conclusions

The main challenges for OLS are in the areas of label generation and label swapping, optical buffering, optically transparent high-speed switch fabrics, clock recovery for burst-mode label and payload, all-optical wavelength conversion, and packet signal regeneration [35]. In particular, optical buffering and high-speed switch fabrics are the two main research focus areas of this thesis, and they shall be covered in the remaining chapters.

Chapter 2 contains a brief introduction to commonly used optical buffers designed for OPS switches. In Chapter 3, a novel optical buffer that is based on a folded-path architecture is described in details. Then in Chapter 4, the simulation and experimental results pertaining to the performance optimization of this buffer will be discussed. This is followed by Chapter 5 where the focus is on optical switch fabrics, especially multicast-capable ones. In this chapter, a new switch fabric design that is based on a gateless broadcast-and-select architecture is also proposed and then experimentally demonstrated. Next, in Chapter 6, the folded-path buffer will be integrated with the gateless switch fabric, and finally in Chapter 7, the 40 Gbit/s performances of the proposed buffer and switch fabric will be examined.

Chapter 2 Optical Buffering

The optical delay buffer and the switch fabric are two of the most important components in the optical packet switch fabrics. They function together to ensure that the packets get routed to their correct destination without getting dropped out of the network. In this chapter, a short introduction to optical buffering is presented along with a description of the existing implementations of optical buffers. Furthermore, these different buffering technologies will be compared in terms of their advantages as well as drawbacks.

2.1 Optical Buffering in OPS Switches

The optical buffer is a photonic storage medium designed to provide either fixed or variable delays for optical signals. When such buffers are used for optical packet switching (OPS) applications, the delay is usually controlled by the routing processor when performing packet synchronization [9, 36], contention resolution [12, 37-42], and traffic shaping. Optical buffers can be positioned at each of the input or output port of the optical router, or they can be shared by all the input ports as depicted in Figure 2 of Chapter 1.

Optical buffers that are designed for OPS applications have a set of performance requirements. These are:

1. Nanoseconds delay reconfiguration time
2. Dynamic re-configurability
3. Transparency to signal wavelength, bit-rate, modulation format and polarization state
4. Physical compactness
5. Low insertion loss
6. Low power consumption

The most important attribute is the delay reconfiguration time, and it is defined as the total time required by the buffer to change its delay from one value to another. Since an OPS switch fabric usually reconfigures in several nanoseconds, the optical buffer should reconfigure its delay within the same amount of time. In addition, the delay should also be dynamically reconfigurable. This means that even though the packet is already stored in the buffer, the delay can be increased or decreased at any time. Such a feature is useful in a practical OPS router because resource contentions can sometimes end earlier or later than initially predicted. Moreover, when there is a switch failure, this feature enables all packets to be flushed out from the buffer very quickly.

While electrical signals can be easily stored in electronic memories, optical signals are made up of photons, and it is difficult to construct an "optical memory" for storing these chargeless particles of light. There are two methods that are widely used to "store" light: one can either reduce its group velocity or make it travel a longer distance. The former is the technique used by slow-light buffers, and the latter is used by optical delay lines.

2.2 Slow-Light Optical Buffers

The primary motivation behind the development of slow-light buffers is the reduction of the group velocity of light in a special propagation medium. Such buffers operate in a small frequency range of the electromagnetic spectrum where the rate of change of the medium's refractive index with respect to frequency is very high. Consequently, the group velocity of light can be greatly reduced, and values as low as tens of meters per second have been reported [43]. The slow-light phenomenon has been widely reported by many different researchers using a great variety of methods: electromagnetically induced transparency in semiconductors [44], photonic bandgap structures with defects [45, 46], stimulated Brillouin scattering [47, 48] and stimulated Raman scattering [49] effects in optical fibers, and coherent population oscillations in crystals [43]. Compared to optical delay lines, slow-light buffers can be designed to be physically very small [44-46], and they also provide very long delays. Furthermore, the delays available can be adjusted in a continuously variable fashion instead of discrete steps. Even though slow-light buffers possess these few advantages over optical delay lines, their ability to function as buffers in OPS routers is still uncertain. So far, no slow-light buffers can provide a large range of delays while maintaining high-speed, dynamic delay re-configurability for entire packets of high-bit-rate signals. In OPS routers, an optical buffer is expected to provide a range of delays ranging from several nanoseconds to tens, or even hundreds of microseconds. The delay should also be dynamically reconfigurable even when the packet is already being buffered, and this reconfiguration should take place within a few nanoseconds.

2.3 Optical Delay Lines

For optical delay line buffers, the objective is to increase the propagation distance of light in the medium to attain the desired delay. Almost any propagation medium can be used as a delay medium but delay lines that are based on integrated optics waveguides [50] and optical fibers are more practical. Waveguides based buffers can be fabricated precisely and they provide the ease of integration with active components. However, large delays are difficult to achieve because of the high propagation losses. The optical fiber-based delay line buffer is currently the best candidate for actual deployment [7, 9, 36, 50-56] . The advantages of using the optical fiber as a delay medium include large transmission bandwidth, low propagation loss, transparencies to signal modulation formats and polarization states, high cost efficiency, and high reliability. Fiber-based delay lines can be broadly classified into recirculating [50-56], feed-forward [7, 9, 36], and folded-path [57-61]. The first two types will be covered in the following sections, while the last — a new buffer architecture that is proposed as part of this research — will be elaborated in the next chapter.

2.4 Recirculating Buffers

In a recirculating buffer [50-56], a packet traverses a delay-line loop repeatedly until it is ready to be read out from the buffer. As depicted in Figure 3, a packet enters the buffer through an electronically controlled optical gate labeled as GATE 1. Once the packet has fully entered the buffer, GATE 1 is turned OFF, and the packet makes repeated passes over the same delay line until the required delay is achieved. At this time, GATE 2 is turned ON

so that the packet can exit from the loop. Otherwise, this gate will remain OFF for the rest of the time.

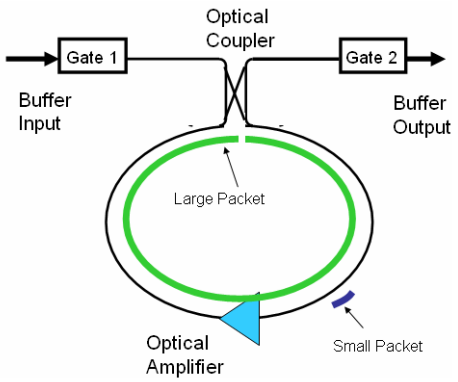

Figure 3. A generic recirculating buffer.

Such buffers have the smallest physical size since the length of the delay that is required is very short. However, due to the losses in the delay line and the switching elements, an optical amplifier is usually required in the loop. Consequently, the accumulation of the amplified spontaneous emission (ASE) noise from the amplifier greatly reduces the number of circulations. Another limitation of recirculating buffers is that the loop length limits the maximum size of the optical packet that can be accommodated [53, 54] (Figure 3), and this happens when the head of the packet overlaps with the tail. If the loop length is increased, smaller packets will on average take too long to emerge from the loop, and thus the random access capability of the buffer is decreased. This problem can be avoided by using wavelength converters in the loop [51, 55, 56], but ASE noise accumulation remains as the performance-limiting factor. By regenerating the signal after every loop, it is possible to increase the number of circulations [52]. However, a precise alignment of the probe signals and the buffered pulses is required. Moreover, the packet size constraint caused by the loop length still exists.

2.5 Feed-forward Buffers

The problems faced by the re-circulating buffers can be avoided by using feed-forward buffers (also known as traveling buffers in some literature). In these buffers, a packet never traverses the same delay line more than once. Examples of such buffers [7, 9, 36] are shown in Figure 4.

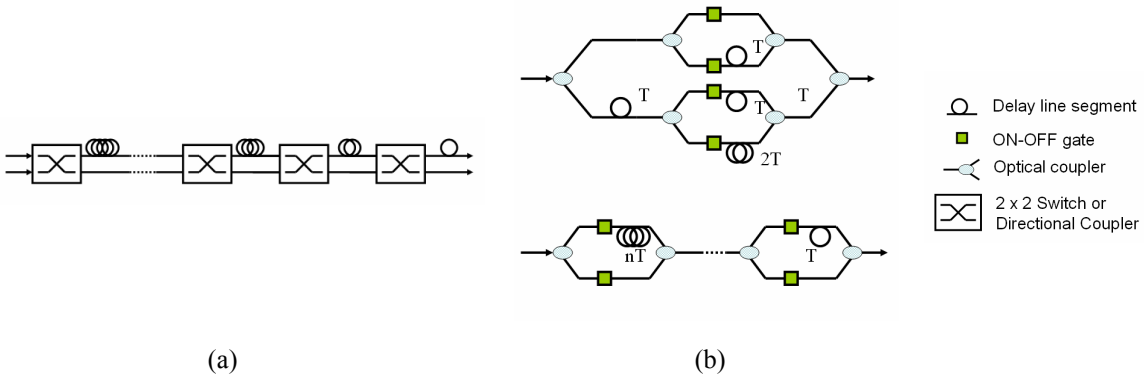

(a) (b)

Figure 4. Feed-forward buffers using: (a) cascaded switches or (b) the broadcast-and-select architecture.

The buffer that is based on the cascaded-switch design [36] uses a high-speed 2 x 2 switch or directional coupler to direct the packet to the appropriate delay line, while the buffer that uses the broadcast-and-select architecture [7, 9] relies on a set of high-speed ON-OFF gates to perform the same function. In both types of buffers, the switching speed of the switches or gates has to be in the order of a few nanoseconds, the same time required for the switch fabric to reconfigure itself. Although feed-forward architectures do not impose a packet size limit like recirculating buffers, they occupy a large physical volume. The broadcast-and-select architecture, in particular, utilizes many delay lines, and if long delays are required, it is obvious that the buffer will become physically very large.

2.6 Conclusions

Various types of optical buffers that are designed for OPS routers have been discussed in this chapter. Although slow-light buffers offer the possibility of a physically compact medium and very long delays resulting from very low group velocity, their delay reconfiguration time is poor, and therefore they are unable to meet the nanoseconds delay reconfiguration time requirement for OPS routers. On the other hand, delay line-based buffers have excellent reconfiguration time, but they are physically much larger because of the use of long fiber delay lines. The lack of physically compact buffers that are able to reconfigure their delays within nanoseconds is the primary motivation for the development of the folded-path delay buffer, and this novel buffer design will be introduced in Chapter 3.

Chapter 3 Dynamically-Reconfigurable Folded-Path Buffer

The motivations behind the development of optical buffers are the subject of discussion in Chapter 2. In this chapter, a novel optical buffer that is based on a folded-path architecture will be introduced [57-61]. The advantages of this buffer versus the other types of fiber-based buffers will be discussed, and various experiments that have been conducted to characterize its performance will also be described. In the final section of this chapter, the folded-path buffer will be modified to allow it to support both buffering and wavelength conversion simultaneously. This is the first time that an optical buffer has been used to perform both of these functions simultaneously.

3.1 The Folded-Path Optical Buffer

Figure 5 shows a generic form of the proposed folded-buffer with *n* sections of delay lines. In each section, there are *m* high-speed on-off gates ($S_{n,0}$ *to* $S_{n,m}$), and these gates can be implemented with high-speed optical switches such as semiconductor optical amplifiers (SOA). Each of the SOA switch is positioned in the middle of a loop-mirror formed by 3 dB couplers, and each reflects an incoming optical signal when provided with bias current in the ON-state.

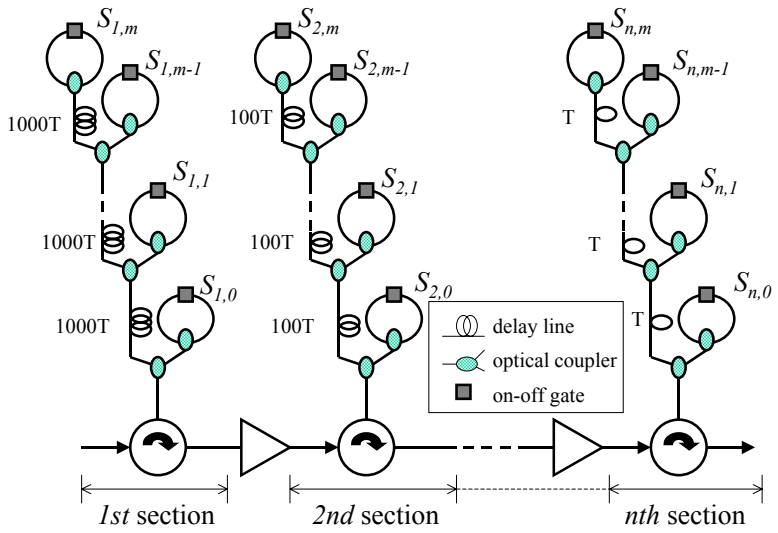

Figure 5. Generic implementation of a compact folded-path optical time delay buffer.

In the OFF-state with no injected current, the incoming optical signals are absorbed. Thus, by switching on the appropriate SOA in a particular section, the desired propagation time delay can be selected. Reconfiguration time of a few nanoseconds, or less, can be achieved by using an SOA with a small free carrier lifetime and a fast electrical driver circuit [62]. Since each of the SOA is operating independently of one another in the time domain, the delay can be readjusted even as the signal or packet is traveling though the buffer. This feature is very useful in certain scenarios such as a switch failure, whereby all packets must exit the buffer immediately.

Unlike the recirculating buffers, the folded-path buffer does not impose limitations on the packet size. In addition, it totally eliminates all the redundant delay line segments used in the broadcast-and-select architectures. For example, Figure 6 shows that to implement a 1T to 4T variable delay buffer, the concatenated-switch type buffer and the broadcast-and-select buffer

require 4T and 7T of delay lines, respectively. On the other hand, the folded-path buffer requires only 2T.

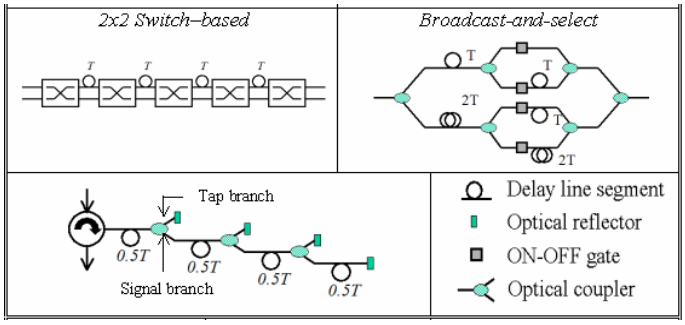

Figure 6. To achieve a 1*T* to 4*T* variable delay, the 2 × 2 switch-based, feed-forward buffer requires a total of 4*T* delay lines, the broadcast-and-select buffer requires 7*T* delay lines, but the folded-path buffer requires only 2*T*.

Compared to the cascaded-switch and the broadcast-and-select architectures, the folded-path buffer also uses less switching elements such as directional couplers or ON-OFF gates. Thus, the number of active components is also expected to be the smallest, and therefore the long term reliability of the buffer will also be higher.

Another advantage of the folded-path buffer is that multiple optical packets can be stored in the buffer at the same time, regardless whether or not they occupy the same wavelength channel. This is achieved through a pipelining technique whereby optical packets can be stored in different delay lines of the same buffer. As depicted in Figure 7(a), packet 1 enters the buffer first, and when it proceeds to the second delay line, packet 2 enters the buffer (Figure 7 (b)). Packet 1 gets reflected by the reflector $S_{1,3}$ and at the same time, packet 2 gets reflected by $S_{1,1}$. Before packet 1 gets completely reflected, packet 2 will have already exit

the buffer (Figure 7 (c)). Pipelining requires complex and precise control of the ON-OFF timing of the reflectors, and this greatly depends on the control algorithm and the processing speed of the electronics.

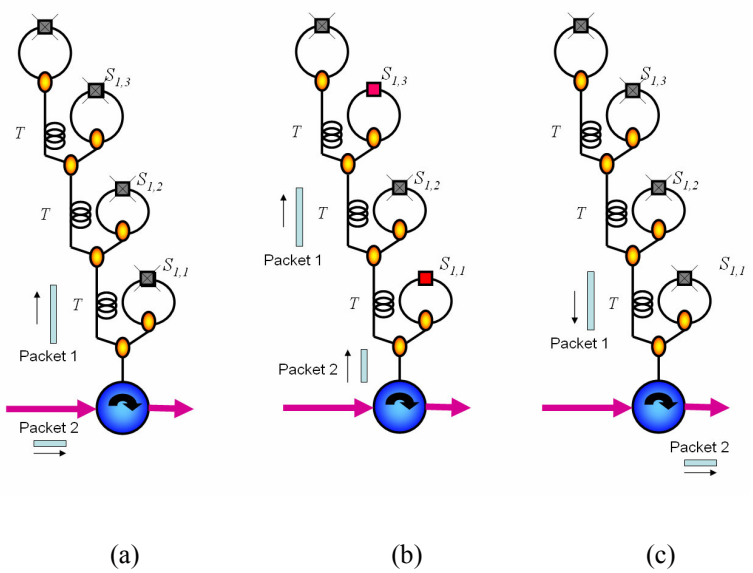

Figure 7. The pipelining technique allows multiple packets to be stored simultaneously in one buffer.

3.2 Time Domain Performance of the Folded-Path Buffer

The experimental setup shown in Figure 8 is used to evaluate the performance of a two-section buffer [57].

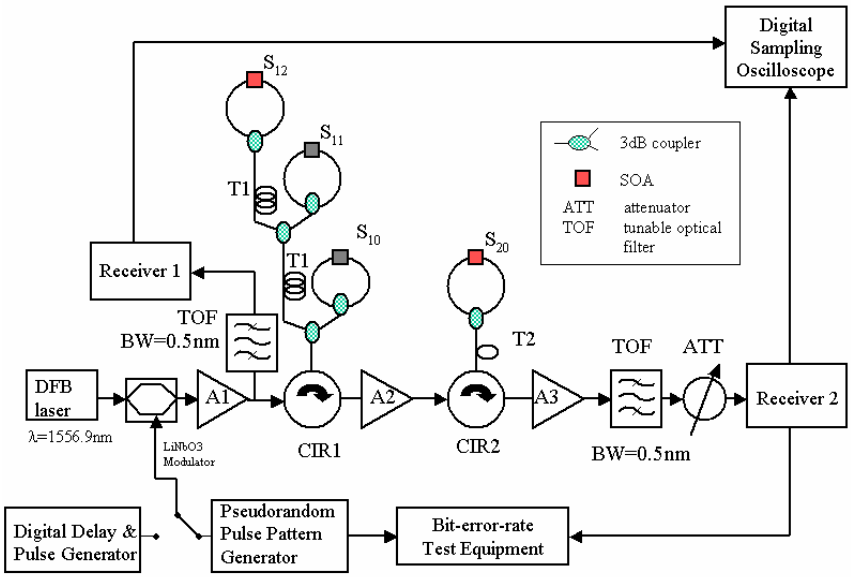

Figure 8. Experimental setup for the performance characterization of a buffer with two sections.

Continuous-wave (CW) light (λ=1556.9 nm) from a distributed feedback laser is modulated by a $LiNbO_3$ external modulator that is driven by a 10 Gbit/s pulse pattern generator with a pseudorandom sequence word length of 2^{31}-1. The NRZ-OOK modulated optical signal enters the buffer with an input power of +5 dBm and traverses two sections of delay lines before exiting. Next, the signal is amplified and bandpass filtered by a tunable optical filter with a 3 dB bandwidth of 0.5 nm, before optical-to-electrical conversion at receiver 2. All amplifiers are erbium doped fiber amplifiers (EDFA) with small signal gain of 30dB and saturated output power of +14dBm.

To implement the delay lines, two SMF-28 fibers (T1) with a total length of 500 m are used in the first section and a single 30 m long SMF-28 fiber (T2) is used in the next. The fibers are connected with the circulators (CIR1 and CIR2) using 3 dB fused fiber couplers. SOA is

used as the ON-OFF gate because of its nanoseconds switching speed, large on-off extinction ratio and wide optical bandwidth [62]. Commercially available SOAs with low polarization dependent gains of 0.3 dB were used. At 1550 nm and with 180 mA of injected current, their average small signal gain and output saturation powers are 10 dB and 5 dBm, respectively. In addition, the return losses of all ports are greater than 45 dB while the ON-OFF extinction ratios are more than 55 dB.

In the first experiment, only the first section of the buffer is used, and the first circulator (CIR1) is directly connected to amplifier A3. SOA S_{12} is provided with a current of 100 mA while the other SOAs are in the OFF-state. From the bit-error-rate (BER) performance shown in Figure 9, the power penalty associated with a single section buffer is 0.6dB at a BER of 10^{-10}, relative to the back-to-back measurement results. For back-to-back measurements, the output of amplifier A1 is connected directly to the input of A3 bypassing CIR1, A2 and CIR2.

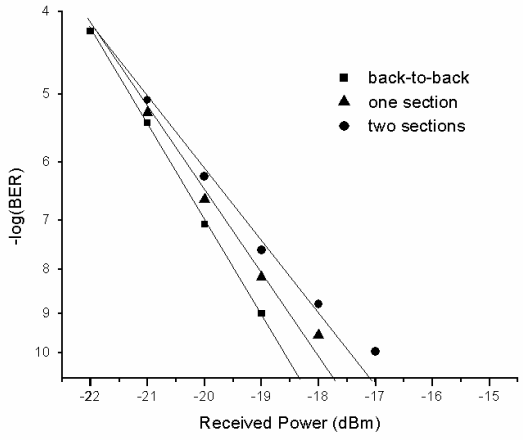

Figure 9. BER performance of the folded-path buffer.

Next, the second section is added and the buffer design is now identical to the one shown in Figure 8 . In this experiment, both S_{12} and S_{20} are in the on-state with injected currents of 100 mA and 80 mA respectively, while the remaining gates are off. From the BER performance shown in Figure 9, it is evident that the addition of another section of buffer only increases the power penalty by another 0.6dB at the same BER. The power penalty is due to cross gain modulation (XGM) induced crosstalk between counter-propagating signals in the SOAs as well as ASE noise from the SOAs and EDFAs. By reducing the current injected into the SOAs, the gain is reduced and the amplifier goes into deep saturation. In this state, distortion on the signal waveform due to gain saturation effect and XGM induced crosstalk will both be reduced.

For time domain measurements, the experiment setup remains the same as the one in Figure 9 except that the pulse pattern generator is replaced by a digital delay and pulse generator which is capable of generating very long digital pulses with arbitrary delays. The output signal from the pulse generator is used to drive the $LiNbO_3$ modulator directly. In addition, receivers 1 and 2 are used to monitor the pulse at the beginning and at the end of the buffers respectively. Figure 10 shows pulse patterns at receiver 1 and 2 superimposed, and it is evident that the input signal is an 80 ns long pulse. With S_{12} and S_{20} in the on-state and the rest of the gates in the off-state, the length of T2 is reduced from 30 m to 0 m. Figure 10 shows that the first section of the buffer added 6230 ns of delay while the second contributed another 370 ns.

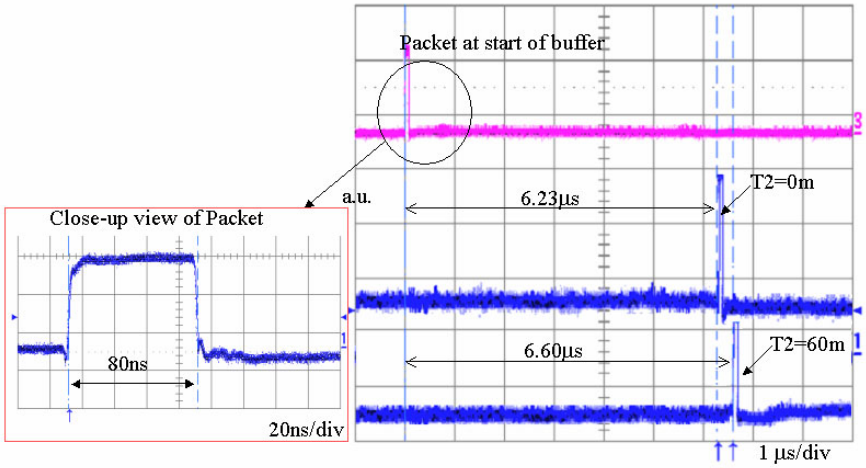

Figure 10. Waveforms at the beginning and at the end of the buffer.

The minimum delay that can be provided depends on the switching time of the ON-OFF gates and the processing speed of the buffer controller logic (typically a small guard time is also added). However the maximum delay time and delay granularity depends on both the depth of the power splitter tree and the number of sections cascaded. In the experiments, power losses in the tree and the limited gain of the SOA restrict the maximum number of delay lines in each section to three but this number can be increased by optimizing the design, and this will be discussed in Chapter 4.

3.3 Signal Waveform Distortion and Crosstalk in the Buffer

One of the drawbacks of using SOAs to amplify non return-to-zero on-off keying (NRZ-OOK) signals is the gain saturation-induced distortion on the signal waveform. Furthermore, if the SOA is placed in a loop-mirror, the signals traveling in opposite directions in the SOA

will suffer from crosstalk caused by cross-gain modulation (XGM). Although these problems are mitigated by using smaller injected current for the SOAs, doing so will lead to a less scalable architecture as a result of an inadequate compensation of the optical power loss in the delay lines. However, both problems can be eliminated if constant intensity modulation formats such as DPSK, also commonly referred to as NRZ-DPSK, is used. A recent experiment involving high bit-rate wavelength multiplexed channels has shown that DPSK is suitable for transmission across long distances with similar performance compared to return-to-zero DPSK (RZ-DPSK) [63]. In order to study the performance of DPSK and NRZ-OOK signals in the buffer, an experimental setup shown in Figure 11 is used [58].

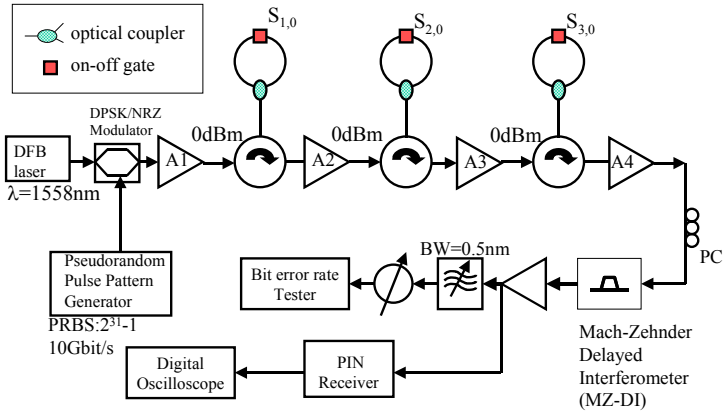

Figure 11. Experimental setup to compare performance of NRZ-OOK and DPSK signals in the buffer.

The buffer consists of three sections with one SOA in each of them. With 180 mA of bias current, the three amplifiers have similar optical characteristics at 1550 nm: small signal gains of 15 dB to 16 dB, output saturation powers of 4.8 dBm to 5.7 dBm, noise figure of 9.8 dB to 10 dB and polarization dependent gains of 0.2 dB. The average signal power at the input ports of each SOA is adjusted using attenuators (not shown in figure) to –3.2 dBm in

order to simulate the worst case when the SOA nonlinear effects on the signal waveform are the strongest. The level of injected current is the same for all three SOAs when they are in the ON-state.

Figure 12 shows the eye diagrams at the receiver for NRZ-OOK and DPSK signals when the injected current varies from 70 mA to 110 mA. At 80 mA, the NRZ-OOK signal suffers from severe pulse shape distortion and XGM-induced crosstalk (Figure 12(b)). However, in the case of DPSK signals (Figure 12(c) and (d)), the eye remain opened and undistorted even when the current is increased from 70 mA to 110 mA, although at 110 mA the noise of the 'zero' and 'one' levels has visibly increased.

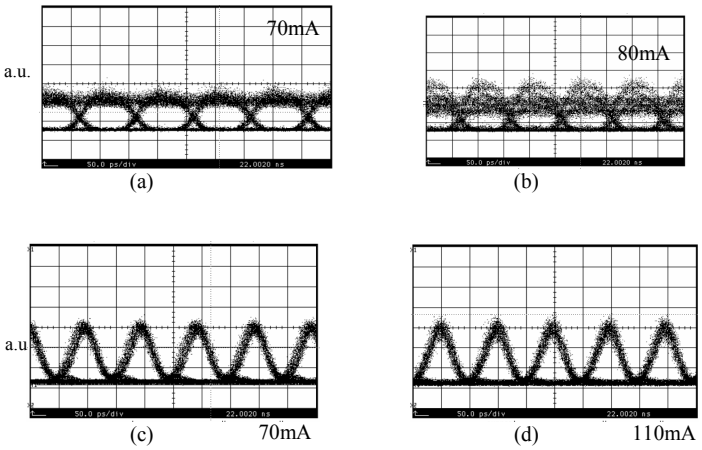

Figure 12. Eye diagrams (50 ps/div) at receiver for various SOA currents (a) NRZ-OOK, 70 mA (b) NRZ-OOK, 80 mA (c) DPSK, 70 mA (d) DPSK, 110 mA.

Thus, to reduce the effect of XGM-induced crosstalk, one can either use a smaller bias current, or use a constant-intensity modulation format. However, using a smaller bias current causes the reflected signal power to be small and the scalability of the buffer is reduced. In

addition, if the choice of modulation format is restricted, the usability of the buffer is too limited. However, both of these problems can be avoided by using a better reflector design, and this will be described in Chapter 4.

3.4 Optical Buffering with Simultaneous Wavelength Conversion

All-optical wavelength conversion is an important aspect of future DWDM optical packet-switched networks since it enables traffic engineering, contention resolution, and provides effective utilization of the vast fiber bandwidth. In existing OPS routers, wavelength conversion and optical buffering are implemented using separate components. However, a modification to the original folded-path design enables both wavelength conversion and buffering to be carried out using a same physical structure [59]. In fact, up to four optical packets occupying four different wavelength channels can be converted simultaneously. Thus, for the first time, an optical buffer is used to provide both time delay and wavelength conversion function for multiple optical packets, simultaneously. The proposed solution can lead to a reduction in the latency in the switch and a lower component count.

Among the various all-optical wavelength conversion methods, only Four-wave mixing (FWM) is transparent to both the signal bit-rate and modulation format. However, one of the drawbacks of FWM is that long interaction lengths are required to achieve high conversion efficiencies. Although recent advances in highly nonlinear (HNL) fibre and photonic crystal fibres (PCFs) [64] have greatly reduced the need for a very long nonlinear medium, several

tens of meters of fibre [64] is still required if these fibers are used. However, this extra fibre can be exploited to provide optical delay in a buffer. Figure 13 shows how a modified version of the original folded-path optical buffer architecture can be used to perform wavelength conversion [59].

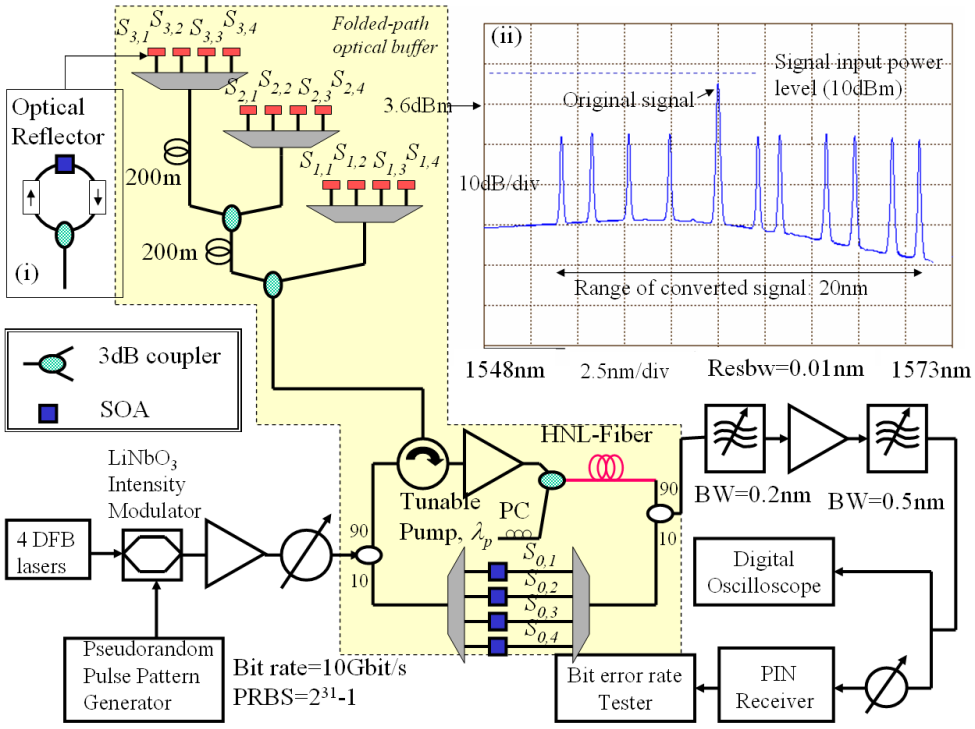

Figure 13. Experimental setup of a multi-wavelength buffer with wavelength conversion capability.

CW light from a DFB laser is modulated using 10 Gbit/s NRZ-OOK, and the resulting signal is sent into the folded-path delay optical buffer. The normal delay line segments are implemented using SMF-28 fibres but the last segment is a HNL fibre that can be used for FWM. The 1 km long fibre has a nonlinear coefficient of 10.5 $W^{-1}km^{-1}$ and a loss of 0.76 dB/km. At 1550 nm, the dispersion slope is 0.019 ps/(nm^2.km), the group velocity dispersion

is -0.19 ps/(nm.km), and the mode field diameter is 3.91 μm. In addition, it's zero dispersion wavelength is at 1561 nm. Optical ON-OFF reflectors are positioned after each delay line segment to reflect the packets when the desired delay is reached. Inset (i) of Figure 13 depicts the structure of a particular implementation of such a reflector using a loop-mirror that can be electrically controlled using an SOA. Such a reflector is known as a unidirectional reflector and it will be described in Chapter 4. From Figure 13, it is evident that an array of such reflectors denoted by $S_{x,y}$ (where x = 1..3 and y = 1..4) have been used to simultaneously reflect packets with different wavelengths. When biased with 180 mA of current, the SOAs have a small signal gains of 15 dB, output saturation powers of 5 dBm, noise figures of 9.9 dB and polarization dependent gains of 0.2 dB at 1550 nm. Due to the wide gain bandwidth of the SOAs, the reflectors can operate with good consistent performance over a wide spectrum.

The wavelength division multiplexer (WDM) is a four-channel interleaver with a channel spacing of 50 GHz. Separate experiments showed that there is very little degradation in performance when multiple packets are reflected together. For four consecutive wavelength channels that are separated by 50 GHz, the extra power penalty is less than 0.5 dB compared to the case when only one channel is reflected. The penalty is mainly caused by interchannel crosstalk. To perform FWM, a tunable laser with wavelength of λ_p is used as the pump. If this pump is turned on, the signals in the buffer are converted. Otherwise, the signals will just experience a delay. A polarization controller (PC) is used to match the pump's polarization state with those of the incoming signal. In practice, polarization independent operation can be easily achieved using polarization diversity schemes [64]. When no delay and wavelength

conversion is required, $S_{0,1}$ to $S_{0,4}$ can be turned on to allow signals to bypass the delay lines altogether.

Inset (ii) of Figure 13 depicts the performance of the FWM process for a single channel. Only one of $S_{3,1}$ to $S_{3,4}$ is turned on and the SOA bias current is 130 mA while its input signal power is -10 dBm. The signal wavelength is fixed at 1561 nm and the pump power is amplified to 12 dBm prior to FWM. The FWM products at various wavelengths, when λ_p is varied, are superimposed on the same figure and it is evident that a flat conversion efficiency of -15 dB can be achieved over a 20 nm range. From Figure 14(a), the maximum power penalty at BER of 10^{-12} is 1.3 dB, and for the cases when the signal undergoes no conversion and no delay, the penalties are 0 dB and 0.2 dB, respectively. Figure 14(b) shows the BER performance of the FWM product of ch1 (at 1563.9 nm) when some or all of $S_{3,1}$ to $S_{3,4}$ are turned ON. The maximum penalty of 1.2 dB (BER=10^{-12}) occurs when all four channels are simultaneously converted. The signal impairment is caused by inter-channel crosstalk and pump power depletion.

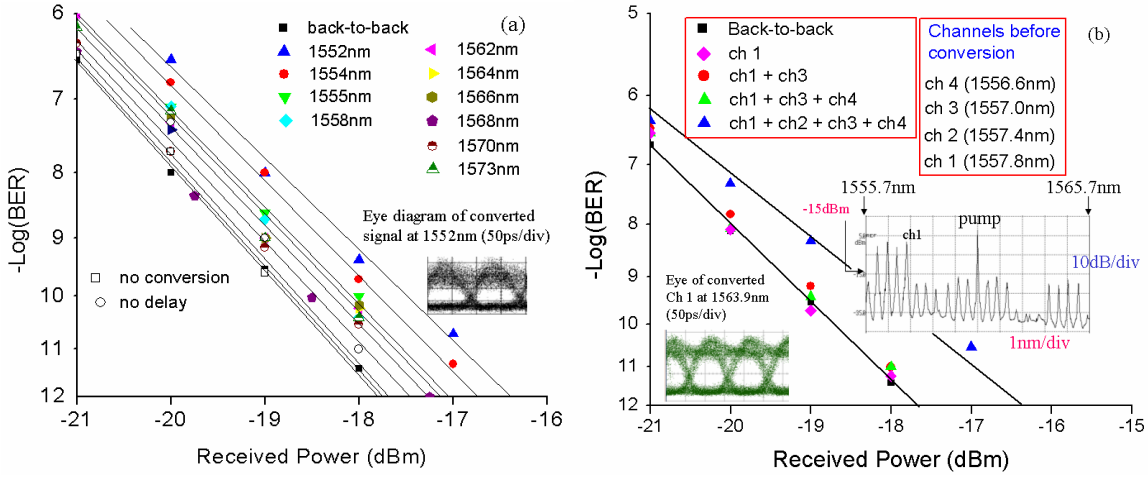

Figure 14. BER performance of the FWM converted signal for (a) 1 channel (b) 4 channels conversions.

Thus, the results in this section demonstrate that the long delay lines in the folded-path buffer architecture, is not necessarily a disadvantage. By exploiting the long interaction length between the pump and the signal, wavelength conversion using FWM can be achieved in the buffer with high conversion efficiencies.

3.5 Conclusions

The physical design, principle of operation, and advantages of the folded-path buffer are described in this chapter. The unique design and concept of this buffer is very different from existing fiber-based buffer architectures based on recirculating loops and feed-forward designs. It relies on optical reflectors that are positioned along a fiber delay tree structure to reconfigure delays experienced by optical packets that are stored in this buffer. By exploiting the bidirectional propagation of light in the delay medium, it is possible to eliminate redundant delay lines and consequently realize a physically compact buffer. Unlike the recirculating buffers, the folded-path buffer does not impose a packet size limitation. Moreover, it does not suffer from excessive ASE noise accumulation commonly found in such delay loops.

The folded-path buffer is dynamically reconfigurable, and it is able to change its delay within several nanoseconds. This is achieved by using high-speed ON-OFF optical reflectors, a concept first proposed in this thesis. By incorporating an SOA optical switch within a fiber loop mirror, a passive optical reflector is transformed into an electrically controllable ON-

OFF reflector because now the bias current of the SOA can be varied to change the reflective property of the loop mirror as desired.

Experimental results show that the folded-path buffer architecture is scalable and flexible. A three-section buffer has been used to store signals with different modulation formats (such as phase and intensity modulation). Although the intensity-modulated format is found to have more degradation due to XGM-induced crosstalk noise, this problem can be corrected by using a better reflector design, and this will be discussed in the next chapter. The folded-path architecture is also shown to be flexible, as it is demonstrated that the design can be modified to support both buffering and wavelength conversion for up to four packets simultaneously. This is achieved by replacing a regular fiber delay line with a highly nonlinear fiber so that a FWM wavelength conversion process can be realized. Experimental results show that the power penalty for converting four 10 Gbit/s is only 1.2 dB at a BER of 10^{-12}. A dual-function buffer is an added advantage for the optical packet router designer as the cost of implementing a separate wavelength converter can be saved.

Chapter 4 Performance Optimization of the Folded-Path Buffer

The optical ON-OFF reflector is the most important component in the folded-path buffer. Its switching speed affects the buffer reconfiguration time, and it also exerts significant influence on the reflected optical signals, affecting both the scalability and flexibility of the buffer architecture. By choosing the best reflector design and using the optimized bias current for the SOA, the range of delay values provided by the buffer can be maximized. The optimization of the folded-path buffer will be discussed in this chapter.

4.1 High-Speed Optical ON-OFF Reflectors

Three different types of ON-OFF optical signal reflectors are proposed [60]: bidirectional, unidirectional, and Faraday reflectors (Figure 15).

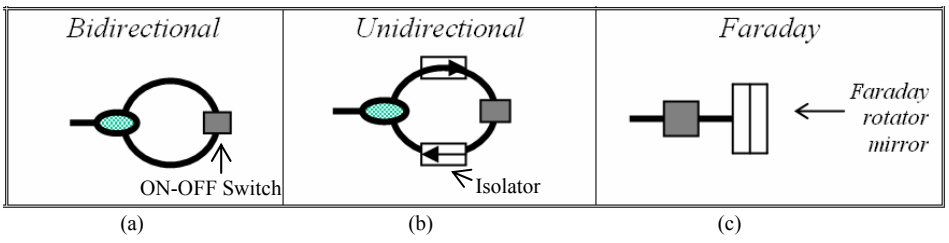

Figure 15. Three proposed designs for ON-OFF reflectors: bidirectional, unidirectional and Faraday.

All three reflectors utilize a high-speed, ON-OFF optical switch to determine their operating state. In the ON-state, the switch is closed, and any incoming signals will be reflected. In the OFF-state, all signals are absorbed in the switch. As explained in the previous section, the SOA is used as the switching device because of its nanoseconds switching speed [62]. In addition, its ON-OFF extinction ratio is typically greater than 50 dB, and this reduces the crosstalk noise from reflectors that are in the OFF state. Three additional advantages can also be obtained by using the SOA. First, the gain can be used to offset some propagation losses in the delay lines. Second, the large amplification bandwidth of the SOA provides signal wavelength transparency. Third, the polarization dependent gain can be designed to be very small.

The delay reconfiguration time of the buffer may be defined as the rise time or fall time of the SOA, depending on whichever is greater (a guard time is normally added too). During the reconfiguration time, the routing processor ensures that the reflector is not being used. From Figure 16, it is evident that the rise and fall time of the SOA (10% to 90% of the output waveform, and vice versa) is less than 10 ns [60].

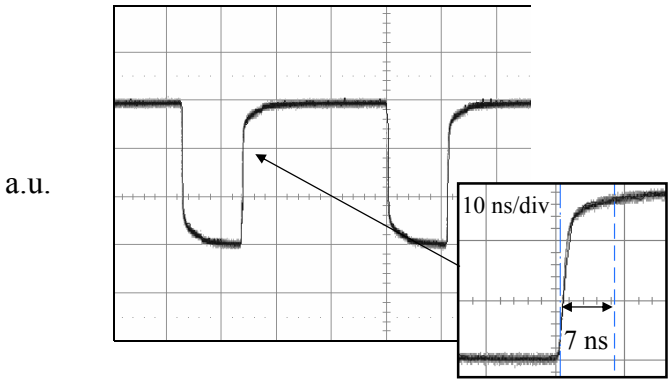

Figure 16. Output waveform from the SOA, displayed using a digital oscilloscope (50 ns/div). The bias current is switched ON and OFF periodically at high speed. Inset: the rise time (10% to 90%) of the waveform is 7 ns (10 ns/div).

The experiment setup shown in Figure 17 is used to evaluate the performance of the reflectors in a single section of the folded-path buffer, and thus, the number of sections, *s*, is set to 1 [60]. Continuous-wave (CW) light (1559.98 nm) from a distributed feedback (DFB) laser is modulated using a $LiNbO_3$ Mach-Zehdner (MZ) intensity modulator to produce non return-to-zero ON-OFF keyed (NRZ-OOK) signals. The modulator is connected to a pseudorandom pulse pattern generator operating at 10 Gbit/s, and the pseudorandom bit sequence (PRBS) length is 2^{31}-1. Next, the modulated signals are amplified using A0, which is an Erbium-doped fiber amplifier (EDFA) with a small signal gain of 33 dB and a noise figure (NF) of 4.7 dB. The amplifier output is then attenuated to 5 dBm to prevent over-saturation of the SOA gain.

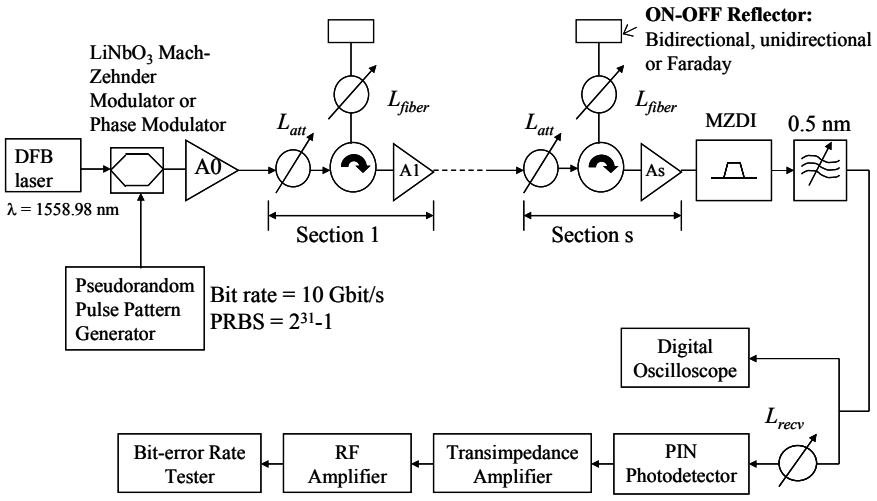

Figure 17. Experiment setup for measuring the BER performance of the reflectors. For NRZ-OOK signals, a $LiNbO_3$ Mach-Zehnder intensity modulator is used, and the Mach-Zehnder delayed interferometer (MZDI) is removed.

After that, the signal enters a 3-port circulator that has an insertion loss of 0.8 dB. Port 2 of the circulator is then connected to another variable attenuator that represents the total insertion losses in the delay lines and the optical couplers. Following that, the signal is then

reflected back to the circulator by a bidirectional, unidirectional or Faraday reflector. The SOA signal input power (P_{in}) and its bias current (I) are both varied in order to study their influences on the performance of the reflectors. Note that P_{in} is defined as the signal power at the connectors of the SOA. When separately measured at 1550 nm, and using I = 180 mA, the SOA has a small signal gain of 15 dB, an output saturation power of 4.8 dBm, and a polarization dependent gain of 0.2 dB. After being reflected, the signal exits the circulator and is amplified by EDFA A1, which has the same performance characteristics as A0. At the receiver, the Mach-Zehnder delayed interferometer (MZDI) is bypassed, and A1 is directly connected to a tunable optical filter, which has a 3 dB bandwidth of 0.5 nm. After filtering, the optical signal is detected using a PIN receiver, and subsequently, the electrical signals are channeled to the bit-error rate (BER) tester. As for back-to-back measurements, the output of A0 is directly connected to the input of A1, and the circulator is bypassed. For all the optical signal-to-noise ratio (OSNR) measurements, the wavelength resolution is 0.05 nm.

When P_{in} = –10 dBm and I = 110 mA, the BER measurements in Figure 18 show that the unidirectional reflector incurs the least power penalty, followed by the bidirectional reflector [60] .

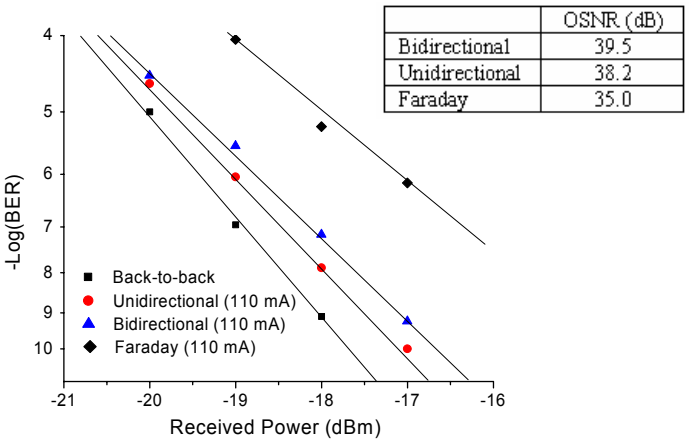

Figure 18. (a) Measured BER performance of NRZ-OOK signals: I = 110 mA and P_{in} = –10 dBm. Inset: OSNR measured at the output of the reflectors when wavelength resolution is 0.05 nm.

Although the OSNR (measured immediately after the reflector) of the latter is higher, the bidirectionally propagating signals in the SOA result in cross-gain modulation (XGM) induced crosstalk noise, and this severely deteriorates its BER performance. The Faraday reflector has the largest power penalty because of two reasons. First, it has the smallest OSNR as the high power of the signal reflected from the FRM reduces the SOA gain by a large value. Second, it has the most severe XGM-induced crosstalk noise, and this is also a result of the strong reflected signal.

Among all the three reflectors, only the unidirectional reflector is not susceptible to XGM-induced crosstalk noise. But like the other reflectors, it is still subjected to waveform distortions caused by the gain saturation effect. From Figure 19, the eye diagrams measured at the receiver show that the waveform distortions become more severe as P_{in} is increased from –10 dBm to –7 dBm [60]. From the same figure, it is also obvious that both the crosstalk and waveform distortion are the worst for Faraday reflector.

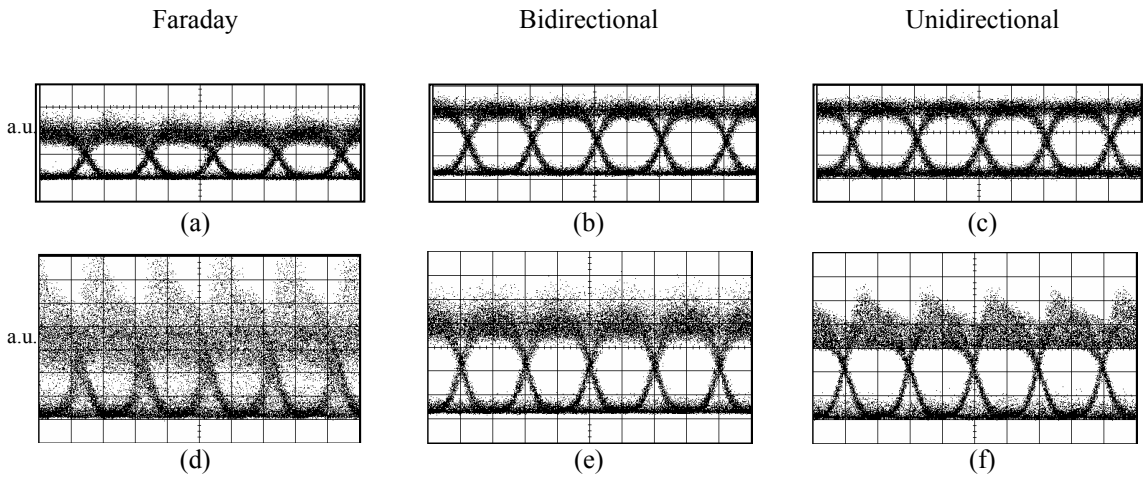

Figure 19. Eye diagrams at the receiver for various reflectors when I = 110 mA for all cases (50 ps/div): (a) Faraday; P_{in} = -10 dBm, (b) bidirectional; P_{in} = -10 dBm, (c) unidirectional; P_{in} = -10 dBm, (d) Faraday; P_{in} = -7 dBm, (e) bidirectional; P_{in} = -7 dBm, and (f) unidirectional; P_{in} = -7 dBm.

Recently, there is renewed interest in using differential phase shift keying (DPSK) as a modulation format for long haul transmission because of its high spectral efficiency [65]. In addition, experiments have also shown that constant intensity DPSK, or NRZ-DPSK, has a similar performance compared to RZ-DPSK [63]. In the case of the optical reflectors, the constant intensity nature of NRZ-DPSK signals results in better performance in the bidirectional reflectors because of a reduction in XGM-induced crosstalk [58]. The experimental setup in Figure 17 is used again to measure the BER performance of the reflectors when the signals are modulated using constant intensity DPSK (s = 1) [60]. However, a $LiNbO_3$ single arm phase modulator now replaces the MZ intensity modulator, and the MZDI is also inserted between amplifier A1 and the optical filter. The MZDI is constructed using commercially available fused fiber couplers, and it has an extra time delay of 50 ps in one of its arms. Note that instead of a balanced detector, a single receiver based on a PIN photodetector is used.

The BER performance (Figure 20) was measured when P_{in} = -10 dBm, and I = 150 mA for both the unidirectional and bidirectional reflectors; for the Faraday reflector, I = 110 mA because for this bias current, the power penalty is the smallest. From Figure 20, it is evident that among the three reflectors, the Faraday reflector has the lowest OSNR of 35 dB, and consequently, its power penalty is the largest. The unidirectional reflector has a slightly better BER performance compared to the bidirectional reflector, although the OSNR of the former is 1 dB smaller than the OSNR of the latter. This anomaly is explained in the next section with aid of a simulation model.

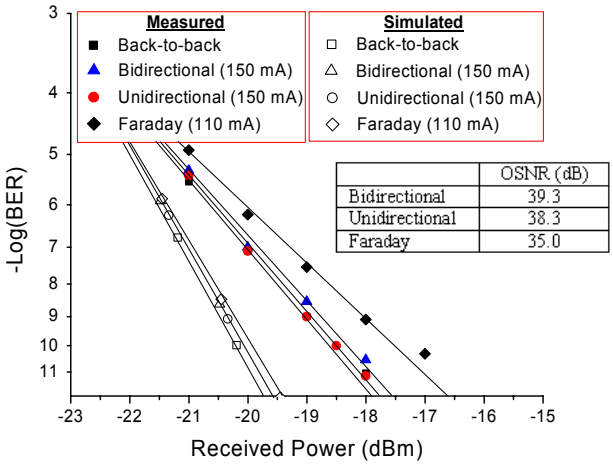

Figure 20. Measured and simulated BER performance of DPSK signals: P_{in} = –10 dBm and the bias currents are indicated within parentheses. Insets: OSNR measured at the output of the reflectors when wavelength resolution is 0.05 nm.

4.2 Simulation Model

A simulation model has been constructed in MATLAB to study the performance of the reflectors in a steady-state condition. There are several objectives for constructing the simulation model. First, it will be used to explain the measured BER performances of the reflectors. Second, it will be utilized in conjunction with measurements to determine the optimal operating condition for the reflectors. Third, it will be used to predict the BER performance of a buffer with multiple sections. The overall simulation setup is similar to the experiment depicted in Figure 17, and it assumed that $s = 1$.

Since the DPSK signals are of constant intensity, a steady-state simulation model for the SOA can be used, and thus, compatibility with the SOA phase noise model can also be ensured [66]. The DPSK signals are represented by a constant-intensity, monochromatic light at 1558.98 nm. In addition, it is assumed that the SOA has completely switched to the ON state, and that it is providing constant gain. The simulation model for the bulk InP-InGaAsP SOA used in all the reflectors is constructed based on the approaches in [67] and [68]. A detailed description of the model can be found in Appendix A.

Since the material properties of the active device were not readily available at the time of simulation, the SOA gain, which in this case is assumed to be polarization independent, is described by a parabolic model given by [69]

$$g(n,\lambda) \approx a_1(n-n_0) - a_2(\lambda - a_3 n - \lambda_1)^2 \qquad (1)$$

where n is the carrier density, n_0 is the carrier density at transparency, λ is the signal wavelength, and a_1, a_2, a_3, and λ_1 are constants. In addition, a_2 is defined as

$$a_2 = \frac{2g_{\max}}{\Delta\lambda^2} \tag{2}$$

where g_{max} is the maximum gain. $\Delta\lambda = \lambda_a - \lambda_b$, where λ_a and λ_b are the upper and lower wavelengths whereby the gain is half its maximum value. In (1) and (2), the constants are $a_1 = 2.48 \times 10^{-20}$ m^2, $a_3 = -2.45 \times 10^{-32}$ m^4, $n_0 = 1.25 \times 10^{24}$ m^{-3}, $\lambda_1 = 1.63 \times 10^{-6}$ m, $g_{max} = 7.18 \times 10^4$ m^{-1}, and $\Delta\lambda = 0.2$ μm. They were obtained by fitting simulated results with measurements of the gain when the power and wavelength of the input signal are both varied. A list of other parameters related to the physical geometry and material properties of the device can be found in Table 1.

Table 1. Parameters used in the simulation model of the SOA

Parameter	Value
Active region length, L	0.65 mm
Active region width, w	0.4×10^{-6} m
Active region thickness, d	0.4×10^{-6} m
Optical confinement factor, Γ	0.45
Refractive index of active region, $n1$	3.22
Refractive index of cladding, $n2$	3.167
Effective index of the guided mode, n_{eff}	3.20
Differential of $n1$ with respect to carrier density, $\frac{dn_1}{dn}$	-1.8×10^{-26} m^{-3}
Intrinsic material loss constant, K_0	6200 m^{-1}
Carrier dependent absorption loss constant, K_1	7500×10^{-24} m^2
Linear radiative recombination coefficient, A_{rad}	3×10^7 s^{-1}
Bimolecular radiative recombination coefficient, B_{rad}	4.6×10^{-16} m^{3}s^{-1}
Linear non-radiative recombination coefficient, A_{nrad}	2×10^8 s^{-1}
Auger recombination coefficient, C_{aug}	3×10^{-41} m^{6}s^{-1}
Input and output facet reflectivity, R	5.0×10^{-5}

Figure 21 shows a good agreement between the simulated and measured SOA gain. The input power of the 1558.98 nm CW signal is varied while the injected current is maintained at 130 mA.

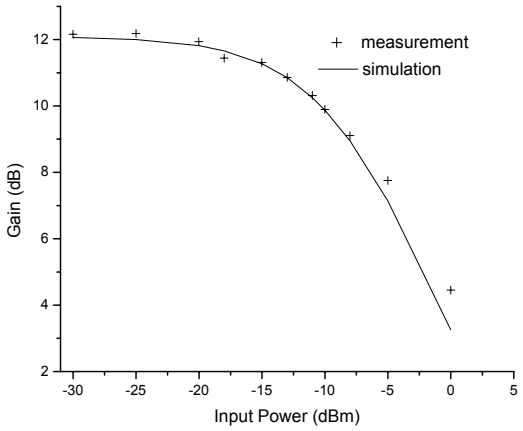

Figure 21. Simulated and measured values for the fiber-to-fiber gain when input power of the 1558.98-nm CW input signal is varied. The SOA is operated at 19 °C and biased at 130 mA.

The phase noise generated in the SOA is a result of a change in the real refractive index brought about by carrier density fluctuations from processes such as intensity noise created from induced emission, non-radiative recombination, and spontaneous emission. The phase noise power spectral density in the linear operation regime of the amplifier is given by [66]

$$S_{\Delta\phi,SOA}(f) = \left(\frac{2\pi\kappa\Gamma}{\lambda w d}\right)^2 \left\{\frac{\left[4G_s\left(G_s-1\right)n_{sp}\tau^2 P_{SOA,in}/h\nu\right]+2N_T\tau}{\left(2\pi f\tau\right)^2+1}\right\} = \frac{C}{\left(2\pi f\tau\right)^2+1} \tag{3}$$

where

$$\kappa = \frac{dn_1}{dn} \tag{4}$$

is the differential of the active region's real refractive index with respect to its carrier density, τ is the carrier lifetime, Γ is the optical confinement factor, h is Planck's constant, and $P_{SOA,in}$, ν, and λ are the signal input power, signal frequency, and signal wavelength, respectively. In addition, N_T denotes the total number of carriers in the amplifier, and n_{sp} represents the spontaneous noise emission factor. In (3), w and d are the width and thickness of the active region, respectively. In addition, the device single pass gain, G_s, is given by

$$G_s(\upsilon) = \exp\left[\int_0^L \left[\Gamma g(n,\nu) - \alpha(n)\right] dz\right] \tag{5}$$

where L is the length of the active region, and z is the signal and noise propagation direction along the length of the active region.

The material loss coefficient, α, in (5), is modeled by [69]

$$\alpha(n) = K_0 + \Gamma K_1 n \tag{6}$$

where K_0 is the intrinsic material loss, and K_1 is the absorption loss associated with the intervalence band absorption. The calculation of the carrier lifetime τ takes into account both the spontaneous emission and non-radiative carrier combination in the linear operation regime of the amplifier, and it is given by

$$\tau(n) \approx \left(A_{nrad} + B_{rad} n \right)^{-1} \tag{7}$$

where A_{nrad} is the linear non-radiative recombination coefficient attributed to traps in the semiconductor, and B_{rad} is the bimolecular radiative recombination coefficient attributed to spontaneous emission. Summing the values of τ in each section of the amplifier and dividing this total by the number of sections will result in an average value of τ that has been used in (3). For both the bidirectional and Faraday reflectors, the phase noise accumulation in opposite directions is assumed to be independent of one another. Because of the symmetry of the bidirectional reflector design, the total phase noise in the reflected signal is obtained by first calculating the phase noise in either direction and then multiplying that value by two. As for the Faraday reflector, the phase noise is calculated by assuming the backward spontaneous emission noise factor is the same as the forward one.

The phase noise variance at the receiver is a sum of the transmitter laser's phase noise and the accumulated SOA phase noise from the reflector. It is given by

$$\sigma_{\Delta\phi}^2 = \sigma_{\Delta\phi,laser}^2 + \sigma_{\Delta\phi,SOA}^2 \tag{8}$$

where

$$\sigma_{\Delta\phi,laser}^2 = 2\pi\Delta f T \tag{9}$$

is the phase noise variance of the laser at the transmitter, Δf is the FWHM laser linewidth, and T is time duration of a bit.

The worst case phase noise variance contribution from the SOA is [66]

$$\sigma_{\Delta\phi,SOA}^2 = \int_0^\infty 4\sin^2\left[\pi f T S_{\Delta\phi,SOA}(f)\right]\, df \le \int_0^\infty 4 S_{\Delta\phi,SOA}(f)\, df = \frac{C}{\tau}. \tag{10}$$

For the bidirectional and Faraday reflectors, the phase noise in the two opposite directions are assumed to be independent, and thus, the total noise variances at the reflector output is simply the sum of the noise variance from each direction. It is also assumed that there is no phase noise contribution from the phase modulator and the EDFAs. In addition, the non-linear phase noise due to the Gordon-Mollenauer effect [70] is not included since the total length of the delay lines in a single buffer is expected to be less than a few kilometers.

After the MZDI, the received signal undergoes optoelectronic conversion using a balanced detector. The MZDI has an extra delay of T seconds in one of its arm, and the insertion loss of the entire interferometer is assumed to be negligible. The balanced detector comprises of a pair of PIN photodiodes, and the voltage waveform after the pre-amplifier is described by [71]

$$\mathrm{v}(t) = \pm \mathrm{v}_n \cos\left[\Delta\phi(t)\right] + n(t) \tag{11}$$

where

$$\mathrm{v}_n = ZR_\lambda P_{sig}. \tag{12}$$

In (12), P_{sig} is the received signal power, Z = 1200 V/A is the transimpedance of the pre-amplifier, and R_λ = 0.8 A/W is the photodiode responsivity. The noise term, *n(t)*, in (11), includes both beat noise and shot noise, and the phase difference over one bit period is given by

$$\Delta\phi(t) = \phi(t) - \phi(t-T). \tag{13}$$

After post amplification, the variance of the Gaussian noise process, *n(t)*, is given by

$$\sigma_n^2 = A_v^2(\sigma_{shot}^2 + \sigma_{sig-sp}^2 + \sigma_{sp-sp}^2 + \sigma_{th}^2) \tag{14}$$

where A_v is voltage gain of the RF post-amplifier. σ_{shot}^2 is the shot noise variance, σ_{sig-sp}^2 is the signal-spontaneous beat noise, and σ_{sp-sp}^2 is the spontaneous-spontaneous beat noise. These noise variances are given by [72]

$$\sigma_{shot}^2 = 2Z^2 eR_\lambda B_e\left[P_{sig} + S_n B_o\right] \tag{15}$$

$$\sigma_{sig-sp}^2 = 2Z^2 R_\lambda^2 P_{sig} B_e S_n \tag{16}$$

$$\sigma_{sp-sp}^2 = Z^2 R_\lambda^2 \left(2B_o - B_e\right) B_e S_n^2 \tag{17}$$

where e is the electronic charge, and B_o = 0.5 nm is the bandwidth of the optical filter, which in this case is assumed to possess a rectangular passband shape. The electrical filter that is positioned after the RF amplifier is also assumed to be rectangular, and it has a bandwidth of $B_e = 0.5B_o$. The noise power spectral density at the receiver, S_n, is attributed to the ASE noise from the SOA and EDFA. It is given by

$$S_n(f) = L_{recv}\left[GL_{fiber}S_{SOA}(f) + (G-1)n_{sp,EDFA}h\nu\right] \tag{18}$$

where L_{recv} is the insertion loss from the variable optical attenuator, and L_{fiber} is the total propagation loss in the delay lines and optical couplers. $S_{SOA}(f)$ is the power spectral density of the ASE from the SOA when only a single polarization is considered. In addition, it is to be noted that for the bidirectional and Faraday reflectors, the total ASE noise is calculated by taking both propagating directions into account.

In (18), G is the EDFA gain that is obtained by solving the transcendental equation [73]

$$G = G_0 \exp\left(-\frac{G-1}{G} \frac{P_{out}}{P_{sat}} \right) \tag{19}$$

where G_0 = 33 dB is the unsaturated small signal gain, P_{out} is the output power of the EDFA, and P_{sat} = 12 dBm is the saturation output power. In (18), the EDFA spontaneous emission factor, $n_{sp,EDFA}$, has a measured value of 1.5. Thermal noise from the RF post-amplifier is also taken into account in (14) by using

$$\sigma_{th}^2 = 4kT_{recv}B_eZF_e \tag{20}$$

where k is the Boltzman's constant, T_{recv} = 313.15 K is the operating temperature of the amplifier, and F_e = 4 dB is its noise figure. The thermal noise of the preamplifier is considered to be negligible.

The probability density function of the total phase noise from the transmitter laser and SOA is assumed to be Gaussian, and it is given by

$$p_{\Delta\phi} = \frac{1}{\sqrt{2\pi}\sigma_{\Delta\phi}} \exp\left(-\frac{\Delta\phi^2}{2\sigma_{\Delta\phi}^2} \right). \tag{21}$$

The probability of error, obtained by considering optimal detection conditions using a zero decision threshold level, is given by [74]

$$P_e = \int_{-\infty}^{\infty} \frac{1}{2} p_{\Delta\phi} erfc\left(\frac{\mathrm{v}_n \cos(\Delta\phi)}{\sqrt{2}\sigma_n} \right) d\Delta\phi \tag{22}$$

where *erfc* is the complementary error function.

4.3 Simulation Results and Discussions

The experimentally measured performances of the unidirectional, bidirectional, and Faraday reflectors will be explained with the aid of the simulation model described in previous section. For the simulation involving the Faraday reflector, I = 110 mA. For those involving the unidirectional and bidirectional reflectors, I = 150 mA. Furthermore, P_{in} = –10 dBm in all the three simulations.

The simulated signal and noise photon rates along the length of the SOA in the Faraday reflector are shown in Figure 22 [60]. It is evident that both the reflected signal and noise continue to be strongly amplified in the backward direction because of the 2 dB insertion loss of FRM is relatively small.

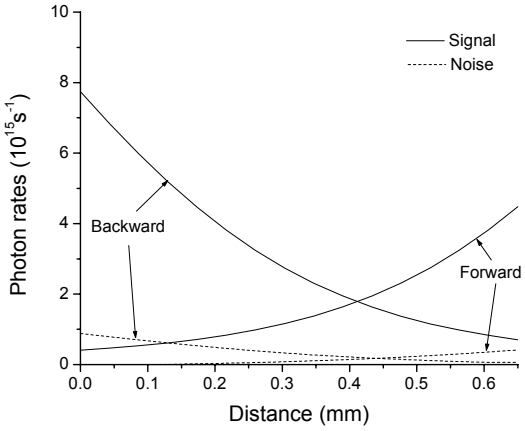

Figure 22. Simulated signal and noise photon rates along the length of the SOA in the Faraday reflector. I = 110 mA and P_{in} = –10 dBm.

The amplifier noise figure in the forward direction for both polarization directions, NF^{+}, is given by [69]

$$NF^{+} \approx 10log_{10}\left[\frac{2(1-R)\eta_{out}\tilde{N}_{j}^{+}(L)}{G_{F}(\nu)}+\frac{\eta_{out}}{G_{F}(\nu)}\right] \tag{23}$$

where $G_F(\nu)$ is the fiber-to-fiber gain, R is the facet reflectivity, and η_{out} is the output coupling efficiency. $\tilde{N}_j^+(L)$ [s^{-1}/Hz] is the frequency normalized, forward propagating, spontaneous emission photon rate of the closest longitudinal cavity mode at the output facet of the amplifier [60]. When compared to the unidirectional and bidirectional reflectors, $G_F(\nu)$ of the Faraday reflector is the lowest because of the large gain saturation caused by the high power of the signal that is reflected back into the SOA by the FRM. Simulations show that NF^{+} is already 13.2 dB in the forward direction alone. In comparison, the noise

figures of the unidirectional and bidirectional reflectors are 11.3 dB and 12.1 dB, respectively ($G_F(\nu)$ is 12.4 dB for the unidirectional reflector and 10.8 dB for the bidirectional reflector). Thus, the noise figure of the Faraday reflector is the highest among all three reflectors.

Simulation results also show that the OSNR of the Faraday reflector is only 34 dB, and this value is at least 2 dB smaller than the OSNRs (in a bandwidth of 0.05 nm) of both the unidirectional and bidirectional reflectors. Figure 23 shows the OSNRs that are measured immediately after the optical signal is being reflected from the three reflectors [60]. In this case, P_{in} = -10 dBm, and the signal is DPSK modulated at 10 Gbit/s. The measurements in Figure 23 also show that the OSNR of the Faraday reflector is the smallest among all the reflectors, and thus, this reaffirms the simulated results. From the simulated BER performance shown in Figure 20, it is evident that this small OSNR and a higher phase noise have both caused the Faraday reflector to incur the largest power penalty. Again, this is in agreement with the measured results shown in the same figure.

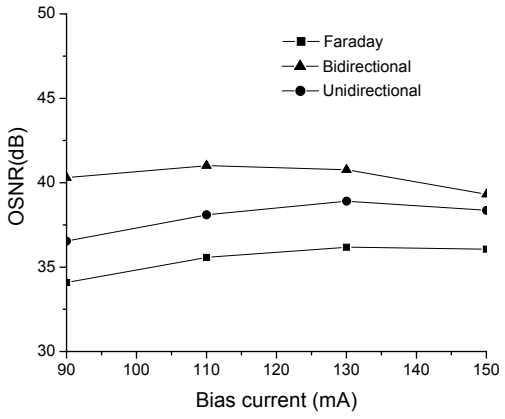

Figure 23. OSNR measured immediately after the reflectors (wavelength resolution of 0.05 nm). The input signal is modulated using DPSK at 10 Gbit/s (P_{in} = -10 dBm).

The simulated SOA gain of the bidirectional reflector is lower compared to that of the unidirectional reflector because of the increased gain saturation resulting from two propagating signals, instead of one. Consequently, simulations show that its OSNR is lower. However, it can be seen from Figure 23 that its measured OSNR is actually higher than that of the unidirectional reflector. This discrepancy is most likely a result of two causes. First, the actual gain saturation might not be as high as that predicted in simulations. Second, because of the birefringence in the loop mirror, the reflected noise power varies according to different polarization states of the noise photons [75]. Thus, the power of the noise might have also decreased slightly after it emerges from the reflector.

Even though the OSNR of the bidirectional reflector is higher, it incurs a larger power penalty, compared to the unidirectional reflector (Figure 20). This could be attributed to a larger phase noise caused by the signals propagating in both directions. Figure 20 shows that the simulated BER performances of the unidirectional and bidirectional reflectors are almost identical. This is because their simulated OSNRs differ only by 0.2 dB. The simulated phase noise of the bidirectional reflector is higher than the unidirectional reflector, but it is not high enough to produce any visible difference in the power penalties.

The performances of all the reflectors are summarized in Table 2. It can be seen that the unidirectional reflector has the best overall performance, in terms of modulation format transparency and power penalty. Therefore, only the unidirectional reflector will be considered in the following sections.

Table 2. Performances of bidirectional, unidirectional, and Faraday reflectors for NRZ-OOK and DPSK signals

	Modulation Format	**Bidirectional Reflector**	**Unidirectional Reflector**	**Faraday Reflector**
Crosstalk (XGM)	NRZ-OOK	Yes	No	Yes
Waveform distortion (gain saturation)	NRZ-OOK	Yes	Yes	Yes
	DPSK	No	No	No
OSNR	NRZ-OOK and DPSK	Highest	Medium	Smallest
Power Penalty	NRZ-OOK and DPSK	Medium	Smallest	Highest

4.4 Optimal Operating Conditions

The BER performance of the folded-path buffer is dependent on the SOA operating conditions such as the bias current level, the active device temperature, and the input signal's average power. A high bias current allows for a greater compensation of the signal attenuation within the fiber delay lines, and thus, longer delay lines can be accommodated. However, if the bias current in the ON-state is too high, then the lifetime of the device will be shortened [76]. Therefore, an optimal bias current level needs to be established.

Figure 24 shows the measured BER performance of the unidirectional reflector when 10 Gbit/s NRZ-OOK and DPSK-modulated signals with are used [60]. The experimental setup is identical to the one in Figure 17 (s = 1). When I is increased from 110 mA to 150 mA, it is evident that the power penalty first attains a minimum value, before it increases again as more bias current is added. Thus, this shows that an optimal current bias exists.

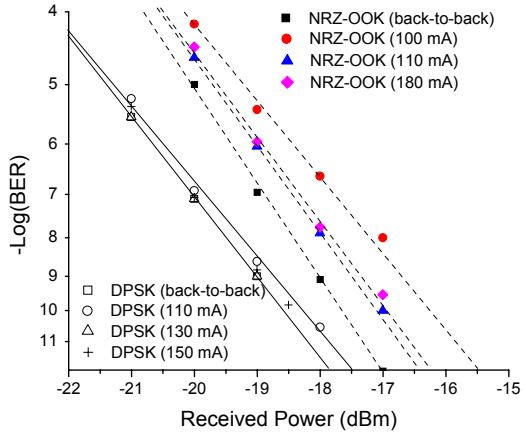

Figure 24. The effect of bias current on the measured BER performance of a unidirectional reflector (P_{in} = -10 dBm) for DPSK and NRZ-OOK signals.

Using the simulation model developed in Section 4.2 for DPSK signals, the change in BER performance is studied when the current is varied Figure 25.

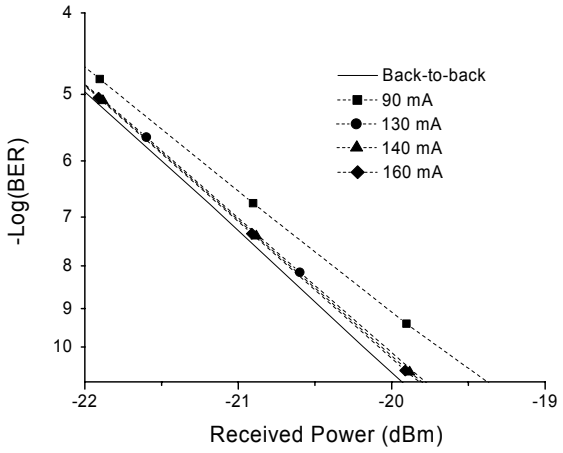

Figure 25. The effect of bias current on the BER performance of a unidirectional reflector (P_{in} = -10 dBm); Simulated results for DPSK signals.

From Figure 25, a similar decrease in power penalty is observed when the current is increased, and this is because the OSNR has become higher at the receiver. However, for I greater than 130 mA, the power penalty continues to decrease, due to an increasing OSNR. Since both simulated and measured OSNRs are expected to continue to increase with current, it is initially believed that the measured BER degradation is due to increased phase noise. Although simulations show that the phase noise becomes larger with higher current, the magnitude of increase is not significant enough to increase the power penalty to the level observed in measurements. When 10 Gbit/s NRZ-OOK signals are used, Figure 24 shows that a similar minimization of power penalty occurring when I = 110 mA. Thus, regardless whether DPSK or NRZ-OOK signals are used, operating the reflectors above very high currents levels, such as 150 mA, degrades the BER performance significantly. Moreover, the

results show that for DPSK signals, the degradation in power penalty is not due to phase noise alone.

In a separate experiment, a 1558.98 nm CW light is used as an input signal for the SOA of a unidirectional reflector [60]. Using an optical spectrum analyzer (OSA), the OSNR of the amplified signal is measured immediately after the SOA. Figure 26 shows the simulated and measured OSNRs at the output of the unidirectional reflector, when both the bias current and the input signal power are varied.

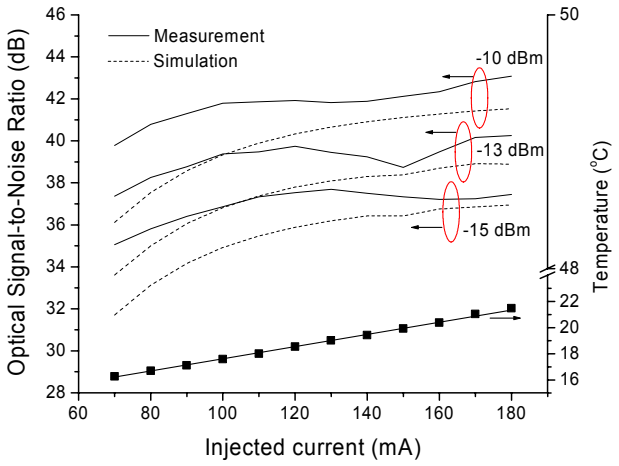

Figure 26. Simulated and measured OSNRs at the output of the SOA when P_{in} of a CW signal is varied. The change in the temperature of the TEC is also shown.

Since the simulation model was optimized for I = 130 mA, there are some discrepancies between the simulated and measured results, especially when I is less than 100 mA. However, for I = 130 mA, the difference between simulated and measured results is less than 1.5 dB. In general, both simulation and measurement results show a common trend: as the current increases, the rate of increase of the OSNR decreases. This is because of a larger leakage

current, higher material losses, and increased Auger recombination [77]. However from Figure 26, it is evident that the measured OSNRs decrease momentarily before increasing again. To investigate this phenomenon further, the particular case of P_{in} = –15 dBm is examined in detail.

When P_{in} = -15 dBm, Figure 27 shows the measured OSNR versus current for two different cases: with and without temperature control.

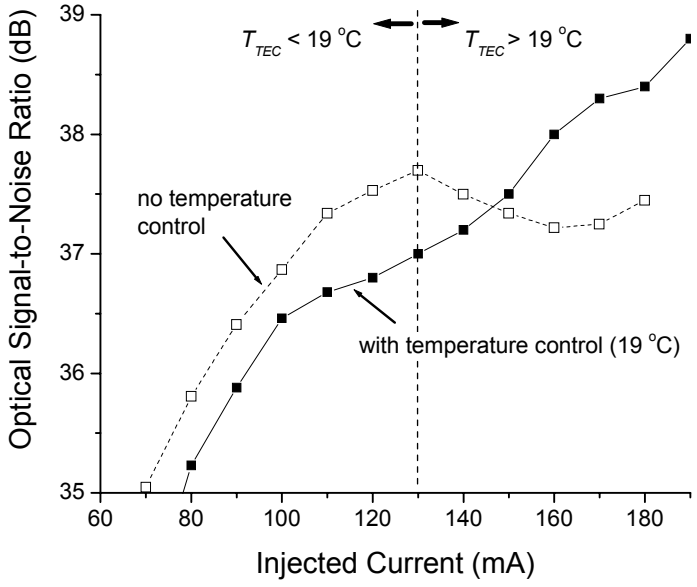

Figure 27. Measured OSNRs for the particular case of P_{in} = –15 dBm. Wavelength resolution is 0.05 nm for all measurements.

When the temperature is controlled, the TEC temperature, T_{TEC}, is held at 19 °C, and in this case, the device temperature now remains constant. It is evident from Figure 27 that when I is in the range of 80 mA to 130 mA, the OSNR is smaller when the temperature is controlled. This implies that when the device temperature is high, the OSNR decreases. In addition,

when I is increased above 130 mA, the dip in the OSNR is not observed, and the OSNR increases monotonically. Therefore, it is believed that the momentary decrease in the OSNR graphs is due to temperature sensitive processes such as Auger recombination. Thus, the degradation in power penalty at high bias currents is due to a combination of temperature sensitive effects and a large phase noise. By taking the different modulation formats and signal input powers into account, the optimal operating current for the SOA used in the unidirectional reflector is determined to be about 130 mA, when no temperature control is implemented.

4.5 Performance of a Buffer with Multiple Sections

To increase the range of delay values provided by the buffer, multiple sections of the folded-path delay line tree can be cascaded (an example of a multi-section buffer is shown in Figure 5). However, the tradeoff is that there is more signal degradation in the form of decreased signal-to-noise ratio. Thus, the performance of a multiple-section buffer must be characterized and compared with that of a single-section buffer. The simulation setup shown in Figure 17 is used to predict the BER performance of a buffer with s multiple sections. In this case, all the reflectors are unidirectional reflectors. Every SOA is biased at 130 mA, and P_{in} = –10 dBm. The linewidth of the transmitter laser is 30 MHz, assuming that a low cost laser is used. Thus, the total accumulated phase noise is $s\sigma_{\Delta\phi}^2$, assuming no contributions from the EDFA and the phase modulator. The simulated BER performance of an s-section buffer is shown in Figure 28 , and when s = 8, a power penalty of less than 2 dB at a BER of

10^{-11} can be achieved. From the same figure, it can be seen that using a laser with a narrower linewidth further reduces the power penalty by 0.3 dB at the same BER.

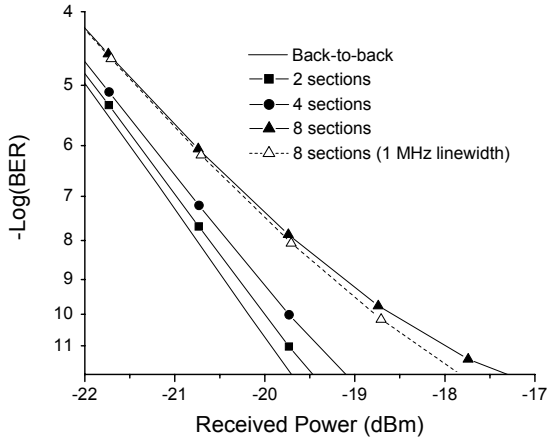

Figure 28. Simulated BER performance of a buffer with multiple sections. The transmitter laser linewidth is 30 MHz if unspecified.

Figure 29 shows an experimental setup to study the degradation in BER performance for DPSK signals when multiple sections of the buffer are cascaded [58]. The variable attenuators represent a total fiber delay line loss of 15 dB from the circulator to the furthest SOA in a single section.

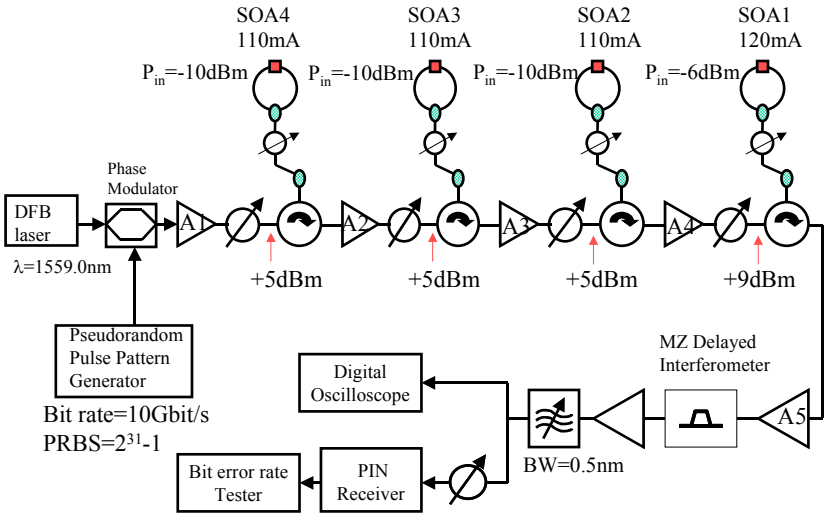

Figure 29. Experimental setup to measure BER performance of a buffer with four sections. In back-to-back measurements, amplifier A1 is directly connected to A5.

It is evident from Figure 30 that at a BER of 10^{-10}, the maximum power penalty for four sections is 1.4 dB. This is 0.4 dB larger than that predicted by the simulation model, and the difference can be attributed to the use of bidirectional reflectors. The eye diagrams at the receiver (inset of Figure 30) after four sections showed a clear opening but with increased noise level in the one and zero levels.

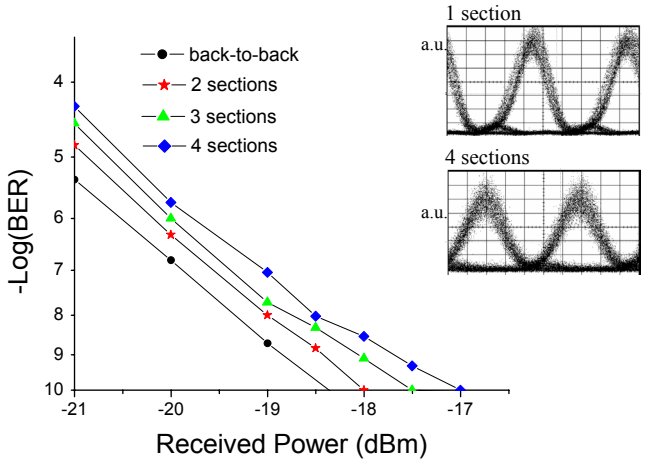

Figure 30. BER performance of a buffer with four sections (insets: eye diagrams at receiver, 20 ps/div).

The total number of delay line segments in the buffer determines the range and resolution of delay values that can be accommodated. While the minimum delay is being limited by the buffer reconfiguration time, the maximum delay time can be increased by using more delay line segments. Alternatively, if the range of delay time is fixed, using more delay line segments increases the time step resolution. To calculate the maximum number of delay segments per section of the buffer, it is first assumed that I = 130 mA and that P_{in} = –10 dBm. Thus, the maximum permissible insertion loss due to the delay lines (L_{fiber}) and the couplers is 15 dB, since the signal power upon entering each section is attenuated to 5 dBm by using

L_{att} (Figure 17). The power distribution tree that can be found in each section of the buffer is similar to the one shown in Figure 31.

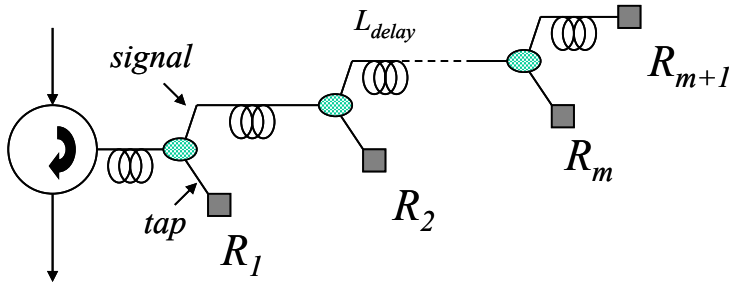

Figure 31. Power distribution tree in each section of the folded-path buffer.

In general, the number of reflectors in a particular section is variable, and they can be denoted by R_1 to R_{m+1}. For each section, the $m+1$ delay lines, each with an insertion loss of L_{delay}, contribute to the total loss, L_{fiber} (Figure 17). Assuming a propagation loss of 0.2 dB/km for each direction in the fiber and a length of 25 m for each delay line segment, the insertion loss per segment is thus 5×10^{-3} dB. The other contributors to L_{fiber} are the couplers. Each of the optical couplers in the power distribution tree has a signal and a tap branch, as shown in Figure 31.

The cumulative insertion losses in the signal and tap branches, as m increases, are shown in Table 3. These losses are attributed to the delay lines and couplers; the losses from the connectors, isolators and the circulators are neglected. The coupling ratio of the fused fiber couplers are denoted by $x:y$, where x and y represent the percentage of the input power in the tap and signal branches, respectively. The typical insertion loss associated with the signal and tap branches of a commercially available fused fiber coupler is shown within parentheses in

Table 3. For the 10:90 coupler (not shown in Table 3), the loss in the signal and tap branches is 0.6 dB and 10.8 dB, respectively. As for the 3 dB coupler (also not shown), it is 3.2 dB for both branches. To obtain the maximum number of delay line segments per section, *m* must be maximized, subject to the condition that the cumulative loss in any of the branches is less than 15 dB. Assuming a coupling ratio of 20:80 for all couplers in the tree, the maximum value of *m* is 4. Similarly, for coupling ratios of 30:70 and 40:60, *m* does not exceed 4. However, using a combination of coupling ratios such as 10:90, 10:90, 20:80, 20:80, 20:80, 30:70 and 40:60, in the same order as their respective positions from the circulator, $m = 7$, and thus, eight delay line segments can be accommodated. To illustrate how the number of delay lines affects the range of delay time, consider a buffer with four sections and eight delay line segments per section. This buffer can provide variable delays up to a maximum of 9.92 μs, if it is assumed that each delay line segment contributes 0.31 μs [57].

Table 3. Cumulative insertion loss in the power distribution tree as *m* increases.
The insertion loss in the signal and tap branches (due to a single coupler) is shown within parentheses.

m	20:80		30:70		40:60		Combination	
	Signal (1.15 dB)	*Tap (7.6 dB)*	*Signal (1.75 dB)*	*Tap (5.5 dB)*	*Signal (2.5 dB)*	*Tap (4.4 dB)*	*Signal*	*Tap*
1	1.16	10.81	1.76	8.71	2.51	7.61	0.61	14.01
2	2.31	11.96	3.51	10.46	5.01	10.11	1.21	14.61
3	3.47	13.12	5.27	12.22	7.52	*12.62*	2.37	12.02
4	4.62	*14.27*	7.02	*13.97*	10.02	15.12	3.52	13.17
5	5.78	15.43	8.78	15.73	12.53	17.63	4.68	14.33
6							6.43	13.38
7							8.94	*14.04*

4.6 Conclusions

The design optimization of the folded-path buffer has been discussed in this chapter. The performances of three different ON-OFF reflectors are compared, and it has been found that the unidirectional reflector has the best overall performance. The primary advantage of this reflector is that it is immune to the crosstalk noise arising from bidirectionally propagating signals in the reflector. Thus, any signals with constant or non-constant time-averaged optical intensity can be accommodated in this reflector.

The other two reflectors, namely the bidirectional reflector and the Faraday reflector, suffer from XGM-induced crosstalk noise since the signals are propagating bidirectionally in the SOA. Moreover, even when constant-intensity phase-modulated signals are used, the phase noise will also be higher than that of the unidirectional reflector. The worst performing reflector is the Faraday reflector because the noise figure of the SOA in such a reflector is the highest.

By studying the characteristics of the SOA in the reflector under various bias currents, it is found that an optimal bias current exists. If the bias current is below this value, the optical signals may not receive enough amplification to compensate for the losses in the delay lines. However, if the current is too high, the device reliability will be reduced. Thus, characterizing the optimal bias current will aid the designer in the selection of the best operating condition for the reflector.

The OSNR of the output signals from the reflectors is found to be affected by the temperature of the SOA in the reflectors. Experimental results show that by increasing the bias current of the SOA, a higher device temperature will result in more Auger recombinations, and thus cause the OSNR to decrease. Therefore, the behavior of the reflector under various bias conditions has to be well understood so that an optimal bias current can be determined. Hence, the experimental results in this chapter will be invaluable in achieving this goal.

The simulation and experimental results in this chapter show that the folded-path buffer can be designed to support a larger number of delay lines by optimizing the reflector design and by cascading more sections of the buffer. Simulation results show that in order to keep the power penalty within 2 dB, a maximum of four sections of the buffer can be cascaded, and each section can contain up to eight delay line segments. This estimation is close to the measured results for an experiment involving 10 Gbit/s DPSK modulated signals. In that experiment, a four-section buffer imposed a power penalty of 1.4 dB (BER of 10^{-10}) on the signals.

When the total number of the delay lines is increased, the range of delay values can be made larger. Conversely, if the range of delay values is fixed, a larger number of delay lines will result in a smaller delay granularity.

Chapter 5 Multicast-Capable Optical Switch Fabric with a Gateless Architecture

The primary functions of a switch fabric will be described in this chapter, along with a review of the most commonly used switch fabrics in OPS routers. After that, the motivation behind the development of multicast-capable fabrics will be discussed. Next, a novel switch architecture that can provide a truly-nonblocking multicast functionality to all the input ports of an optical router will also be introduced. Unlike its predecessors, the proposed architecture does not utilize any electrically-controlled ON-OFF gates. This advantage is expected to result in a significant reduction in the number of components required to implement such kind of switch fabrics.

5.1 Optical Switch Fabrics

The switch fabric of the OPS router is where the space switching of the packets takes place. The premise of using an optical switch fabric is based on the belief that conventional electronic switch fabrics cannot achieve the switching speed and the strict optical transparency required by future OPS networks. A switch fabric designed for OPS should possess the following attributes:

1. Nanoseconds reconfiguration time
2. Low crosstalk and high ON-OFF extinction ratio

3. Transparency to signal wavelength, bit-rate, modulation format and polarization state

4. Highly scalable in terms of port count

5. Low power consumption

6. Physical compactness

In addition, the fabric should also be strictly non-blocking. For OLS, nanoseconds reconfiguration time is required, and this automatically precludes the use of slower switching elements that are based on MEMs [78], thermo-optic effect [79], and liquid crystals [80]. Switches that are based on the electro-optic effect are attractive candidates because a switching time of a few tens of nanoseconds can be achieved. Most of these switches are based on $LiNbO_3$ [81], but other materials [82, 83] have also been used. However, because of the material limitations, these switches typically have very high losses, and thus, the construction of large fabrics can be very challenging. Another category of switching elements is based on the refractive index change brought about by carrier injection in semiconducting materials. Such switching elements typically have a switching time of a few nanoseconds, and the switching mechanism is either based on evanescent coupling between waveguides [84, 85] or the total internal reflection effect [86]. Consequently, the crosstalk, extinction ratio and insertion loss performance can differ greatly depending on individual design. Nevertheless, large switch fabrics on a single substrate have not been experimentally demonstrated.

Space switching can also be carried out using an arrayed waveguide grating router (AWGR) and high-speed wavelength converters in a scheme known as wavelength assisted space

routing [42, 87]. In this scheme, the AWGR acts as the signal interconnect, and the wavelength converter performs the role of the switching element. To route the signal to a particular output port of the AWGR, the signal has to undergo wavelength conversion first. After that, another wavelength conversion operation is sometimes necessary to restore the original wavelength.

Another category of switches is based on the broadcast-and-select architecture [7, 9, 88, 89]. The switching element is usually a high-speed ON-OFF gate such as an SOA, and the interconnection medium is the optical fiber. The switching is performed in two steps. First, all the signals from each input port are broadcasted to every output port using a power distribution network consisting of amplifiers, arrayed waveguide grating and optical fibers. Second, a group of high-speed ON-OFF gates is placed at every output port to either block the signals or allow them to pass through. Using SOAs, nanoseconds switching speeds, low crosstalk and high ON-OFF extinction ratios can be achieved.

5.2 The Need for Optical Multicasting and Broadcasting

Multicasting and broadcasting are important functionalities [90] that can be used by optical switches to perform tasks such as contention resolution or support network applications such as video distribution and on-line gaming. One of the methods for achieving broadcasting/multicasting in the switch fabric utilizes the so called wavelength-assisted routing scheme, whereby a set of tunable lasers AWGR are used together to perform space

switching [87, 91]. The wavelength-assisted routing switch fabric is usually used in hybrid optical routers [91, 92].

The hybrid optical packet router [91, 92] utilizes electronic components for performing 3R (Regeneration, Re-amplification and Retiming) and buffering of the packets, but employs a fully-optical switch fabric for port-to-port space switching. As the technology for optical buffering and all-optical 3R [14] are still in development, a general consensus is that it is more cost and energy efficient to implement these functions using electronic components. But for space switching, optical switch fabrics are still preferred because as data bit-rates continue to increase to 40 Gbit/s and above, it is very difficult to construct electrical interconnects that support large-scale switching and multicasting operations. Thus, optical switch fabrics could be among one of the first few optical components that will be deployed in future generations of commercial high bit-rate routers.

In a hybrid optical router, the optical packets have to be converted to electronic signals before any buffering or signal reconditioning can occur. These optoelectronic conversions are typically carried out in the ingress line cards as depicted in Figure 32.

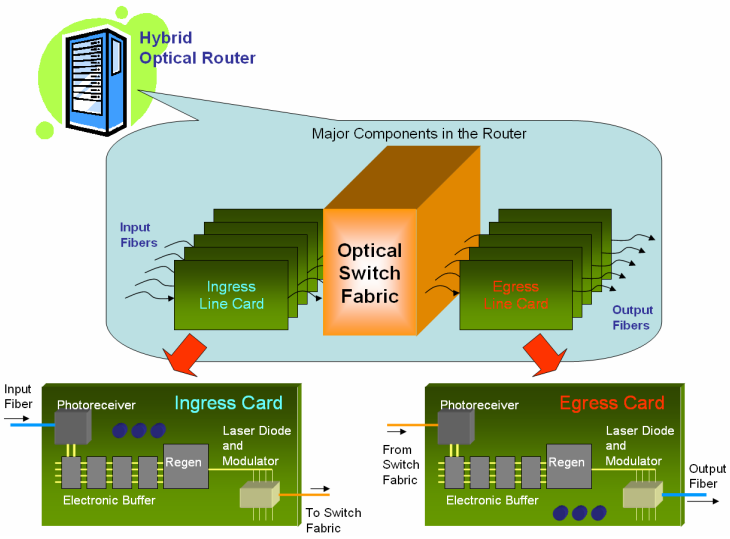

Figure 32. Components in a hybrid-OE router.

The input to an ingress line card is the optical fiber that is carrying the optical packets. Note that even though a WDM demultiplexer is not shown in Figure 32, it may be included in the router to separate the different wavelength channels at the input fiber. The optical packets are converted to electronic signals in a photoreceiver module residing on the ingress card before they can proceed to the electronic buffers and signal regeneration components. Next, the packets are re-converted back to optical form so that the optical switch fabric can be used. To accomplish that, the card may have its own laser source and high-speed data modulator. After the switching is completed, it may be necessary to regenerate the optical signal once again because of excessive losses in the switch fabric. Thus, an egress line card may be used, and its design will be very similar to the ingress line card. Like the ingress line card, the egress card may also contain electronic buffers.

The need for multiple OE conversion processes is clearly one of the biggest disadvantages of the hybrid router because such conversions impose restrictions on the modulation format and data bit-rates of the signal. In true optical packet switching, an OPS router should be able to route any optical packet regardless of the content of its payload, and so optoelectronic conversions of the payload would be unnecessary. Thus, the hybrid router solution is at best only an interim one, because if OPS is fully implemented, the data packet will remain in optical form from the source to destination.

The wavelength-assisted routing scheme is shown in Figure 33. Tunable lasers residing on the ingress cards are used to select the output wavelength of the packets that are to be switched. Based on the cyclic property of the arrayed waveguide grating (AWG) [93], the packets are routed to different output ports when the wavelength is varied. After the packets are routed, they are again converted to electrical signals on the egress cards.

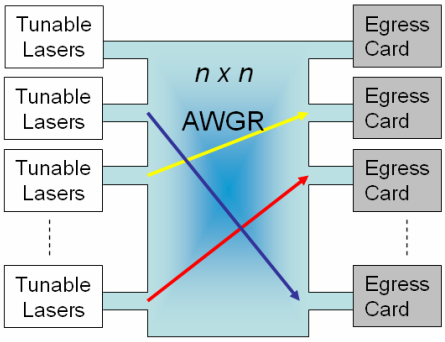

Figure 33. The wavelength-assisted router uses tunable lasers and an AWGR for switching

Although the wavelength-assisted routing scheme is simple and can support high bit-rate signals, it cannot be used for broadcasting or multicasting. This is because for every packet

that enters the AWGR, it has to exit from only one of the output ports of the AWGR. Recently, there are attempts to implement optical multicasting using the wavelength-assisted routing scheme by converting a pair of input and output ports as depicted in Figure 34 [94].

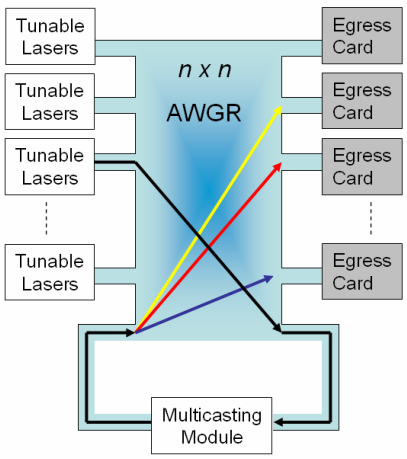

Figure 34. Modifications to the original WA assisted router allows partial multicasting functionality.

The pair of ports is connected to a multicasting module where the optical multicasting or broadcasting is performed. After this process, the content of the original packet will be duplicated onto a set of wavelength channels each occupying a distinct wavelength. These wavelengths are selected in such a way that when the multicasted channels re-enter the AWGR, they can be routed to the appropriate output ports. Unfortunately, because most of the ports of the AWGR are used for routing purposes, the modified design only allows signals from one or some of the input ports to be multicasted at the same time. Since applications such as video streaming usually require repeated multicasting services over an extended period of time, a high blocking probability will occur, and this will certainly decrease the switch performance.

Conversely, switches that are based on a broadcast-and-select architecture can provide multicasting and broadcasting services for every input channel in a truly non-blocking manner [7, 9, 88, 89]. Note that since the switching scheme does not alter the original wavelength of the packets, the architecture can be used in an all-optical router without any modifications. The main drawback of existing broadcast-and-select architectures is that the number of switching elements required grows very quickly when the port count and the number of wavelength increase. Since the SOA has many advantages when it is used as an optical switch, it is usually the preferred choice for the switching element. Although very large fabrics of up to 256 ports have been demonstrated using SOAs as switching elements [95], the power consumption is very high because of the broadcast operation and the power required by the thermoelectric coolers (TECs) and high-current drivers of the SOAs. If there are m wavelength channels per fiber, a switch fabric with n input and n output fibers require $n^2m + m^2n$ switches [89, 95]. Moreover, if gain-clamped semiconductor optical amplifier (SOA) switches are used [89, 95], the fabric is not transparent to the signal bit-rate and modulation format.

The disadvantages of the existing fabrics are the primary motivations for the proposal and development of a new type of broadcast and multicast-enabled switch architecture in this research. The new architecture does not require any optical gates, and the switching technique is expected to be compatible with signals with bit-rates of 40 Gbit/s or higher. The design and performance characteristics of this architecture will be described in the next section.

5.3 The Gateless Multicast-Capable Optical Switch Fabric

To solve the problems encountered by existing multicasting switch fabrics, a new broadcast and multicast-capable switch architecture is proposed and experimentally demonstrated [96]. This architecture eliminates the use of ON-OFF gates, and thus a significant reduction in the number of components in the router can be expected. In addition, for a switch with n input or output fibers and m wavelength channels per fiber, the proposed architecture will only require the same number of lasers ($2n \times m$) as the most basic wavelength-assisted routing scheme. But unlike the latter, the new architecture allows all input channels to be multicasted or broadcasted simultaneously.

The proposed architecture uses a 3-step approach to perform switching: λ pre-shifting, broadcast, and select-and-restore. A specific implementation of the architecture for $n = 4$ is shown in Figure 35, where $\lambda_{x,y}$ represents the original wavelength channel y from the input fiber x, and $\lambda^{k}_{x,y}$ represents this same channel that has been wavelength shifted to the new position k ($k = 1...n$). Note that in this implementation, the router is assumed to have no ingress and egress cards, and a distinction should be made between such all-optical routers and the hybrid ones discussed in the previous chapter. Nonetheless, the proposed architecture can also be used in a hybrid router after slight modifications, and this will be discussed in Chapter 7.

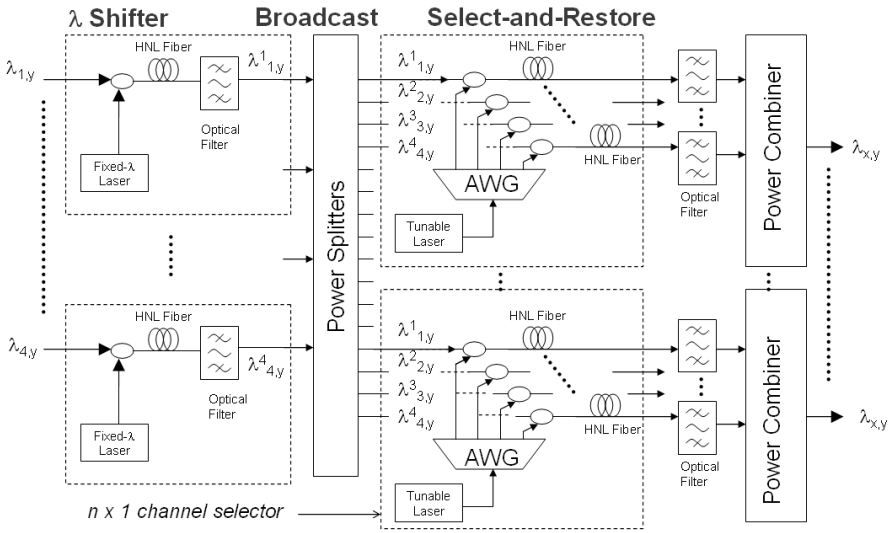

Figure 35. Physical implementation of the proposed multicast/broadcast architecture.

After wavelength demultiplexing (not shown in Figure 35), each wavelength channel undergoes wavelength conversion (WC), and the magnitude of wavelength shift is determined by the position of the input fiber from which the channel originated. As an example, Figure 36 shows 4 channels (with the same center wavelength, $y = 2$) from 4 different input fibers experiencing different shifts in accordance with the position of their input fiber. Since the magnitude of the shift is predetermined, a set of n fixed wavelength lasers can be used for the converter. After the pre-shifting, each channel is then broadcasted to every output fiber, and an $n \times 1$ selector at each of the output fiber selects one of the n channels. Whenever a channel is selected, its original wavelength is also restored.

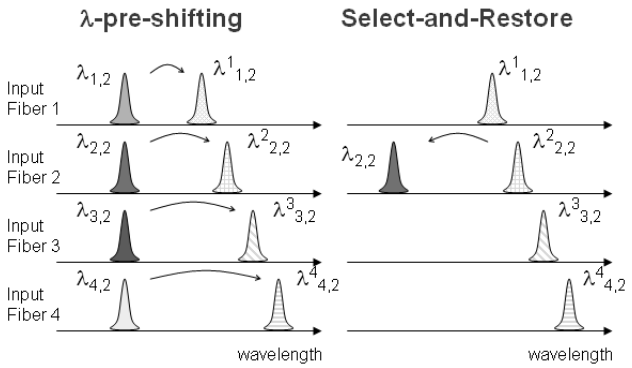

Figure 36. Operating principle. Wavelength channel number 2 from each of the 4 input fibers is shifted to different intermediate wavelengths, depending on the position of the input fiber.

The 4 × 1 selector shown in Figure 35 is implemented using wavelength conversion based on the Four-wave mixing (FWM) process in fiber. At every output fiber, there is a 1 × 4 AWG, and the input port of the AWG is connected to a tunable laser that acts as the pump for the FWM (Figure 35). Each output port of the AWG is then connected to each of the 4 fibers that carry the broadcasted channels, and the center wavelengths of the AWG output channels are matched to the corresponding pump wavelengths that will enable the original wavelength, $\lambda_{x,y}$, to be restored after the FWM process. Whenever the pump is absent, a channel does not undergo wavelength conversion, and the signal will be filtered out by a bandpass filter that has a center wavelength of $\lambda_{x,y}$. However, when a pump is present, the bandpass filter ensures that only the restored channel is present at the output fiber. Thus, any one of the 4 channels can be selected by varying the wavelength of the tunable laser.

5.4 Performance Characterization of the Gateless Multicast Switch Fabric

The experimental setup shown in Figure 37 is used to study the performance of a 4 x 1 switch (m = 1) when different channels are selected [96]. All the input channels are broadcasted to the output fiber, but only one channel is selected each time. FWM wavelength conversion is used in both the pre-shifting and the select-and-restore stages. For the former, a highly nonlinear (HNL) fiber is used, but for the latter, the HNL fiber is replaced by an SOA due to resource constraints.

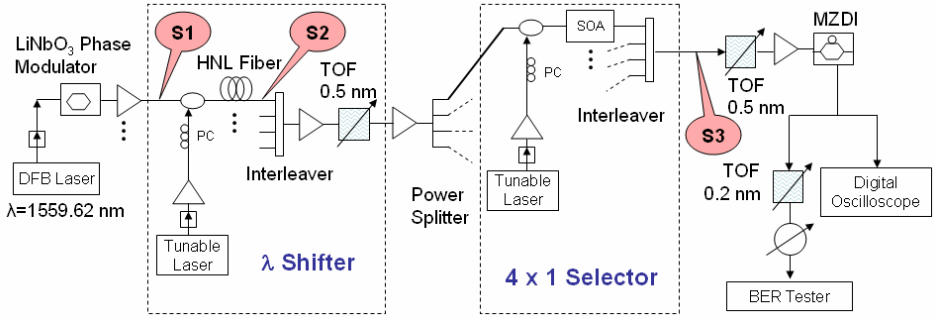

Figure 37. Experimental setup for measuring the performance of a 4 x 1 switch. TOF: Tunable optical filter. PC: Polarization controller.

The 10 Gbit/s DPSK input signals are generated using $LiNbO_3$ phase modulators with CW light from DFB lasers (PRBS = 2^{31} - 1). Upon entering the switch, the wavelengths of the input channels are shifted to 4 different positions using FWM in the HNL fiber. The pump wavelengths for input fibers 1 to 4 are 1560.62 nm (*P1*), 1560.82 nm (*P2*), 1561.02 nm (*P3*), and 1561.42 nm (*P4*), respectively. At the input of the HNL fiber, the average power of the pumps and signals are 8 dBm and 2 dBm, respectively. After FWM, the original signal and the pump are filtered out using a four-channel, 50 GHz interleaver. The pump wavelength of 1561.22 nm is skipped because the converted signal occupies the same channel in the

interleaver as the original signal. In general, this will not be a problem as bandpass filters are used instead of interleavers. After filtering, the signals are amplified, before they are being broadcasted to each of the output fibers using EDFAs and power splitters based on fused-fiber couplers. The pump wavelength is varied from P1 to P4 so that each channel from input fibers 1 to 4 can be selected. The average power of the pump and signal at the SOA input are 8 dBm and 0 dBm, respectively. Next, the selected channel is filtered, amplified and then converted to an intensity modulated signal using a Mach-Zehnder delayed interferometer (MZDI) before it is being photo-detected at the receiver.

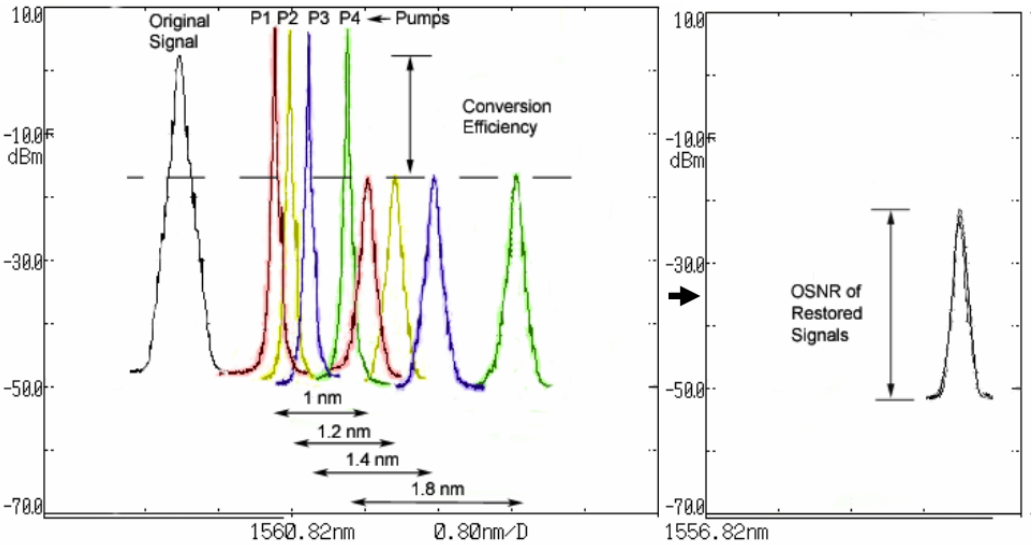

Figure 38. Superimposed spectra. (a) The original signal, the pumps, and the corresponding wavelength-shifted channels. (b) the restored channels. The pump-signal de-tunings ($\Delta\lambda$) are 1 nm, 1.2 nm, 1.4 nm and 1.8 nm. Resolution BW is 0.05 nm.

The spectra of the original signal, the pumps, and the corresponding wavelength-shifted channels are all shown, superimposed in Figure 38(a), while the restored channels are shown in Figure 38(b). The measurements are taken at positions S1, S2, and S3 shown in Figure 37,

respectively. As is evident from the figure, the conversion efficiencies of all the channels are the same, and they are approximately -20 dB. In addition, the optical signal-to-noise ratios (OSNR) of the restored channels are more than 30 dB, and their average powers are -22 dBm. The BER performances of the restored channels are shown in Figure 39, and it is evident that the power penalties of all the channels are between 0.8 dB to 1.5 dB at a BER of 10^{-12}. The worst penalty occurs when the pump and signal de-tuning, $\Delta\lambda$, is 1.8 nm, and this is because in the SOA, the FWM conversion efficiency decreases very quickly when the frequency detuning between the pump and signal increases. However, if the SOA is replaced by a HNL fiber, the conversion efficiency can remain constant over 70 nm [97].

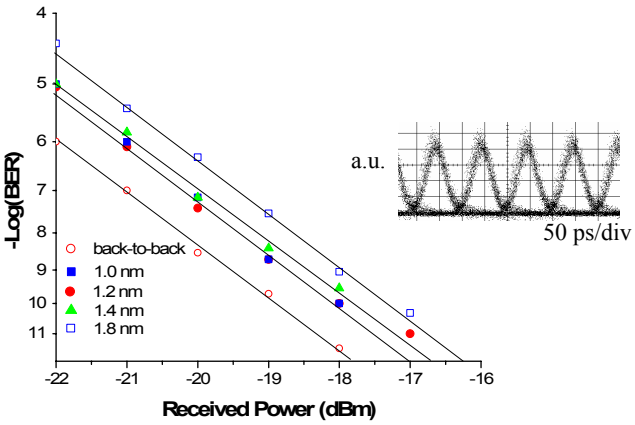

Figure 39. BER performance of the signal at the receiver when different input channels are selected. Inset: eye diagram of the received signal when $\Delta\lambda$ = 1.4 nm.

5.5 Conclusions

In summary, the gateless multicast-capable switch architecture has been experimentally demonstrated to be a viable solution for a switch fabric. The power penalty that it imposes on the input signals can be kept below a commonly acceptable level of 2 dB for all input ports. Since the proposed technique eliminates the need for optical ON-OFF gates and additional wavelength restoration stages that are used in existing broadcast-and-select architectures, a significant reduction in component count can be expected. Moreover, because the FWM wavelength conversion that is utilized in the switching technique is transparent to both the signal bit-rate and modulation format [98], the proposed architecture is expected to be more scalable and flexible than existing designs. Unlike AWGR-based wavelength-assisted routing schemes that are not multicast-capable, the proposed architecture provides multicasting and broadcasting functionalities to all input ports, simultaneously. Moreover, this is accomplished by using only the same number of lasers. In the next chapter, the integration of the folded-path buffer and the gateless switch fabric will be discussed, and in chapter 7, the same architecture will be modified for use in a hybrid router. Its performance at 40 Gbit/s is also experimentally characterized.

Chapter 6 Buffer and Switch Integration

An OPS router is designed to switch, buffer and regenerate optical packets in the most transparent manner regardless of the bit-rate, modulation format and wavelength of these packets. Thus, every component in the switch is expected to fulfill these design criteria even after they have been physically integrated. In this chapter, the folded-path buffer and the gateless multicast-capable switch discussed in previous chapters will be physically integrated into a subsystem to test for compatibility. To reduce noise propagating from the buffer to the switch, a solution based on a fiber bragg grating (FBG) will be proposed and experimentally tested.

6.1 Noise Reduction using Fiber Bragg Grating

When implemented in actual optical routers, the buffer and the switch fabric have to be seamlessly integrated with one another. This means that even when they are integrated, the operation of one component should not adversely affect the performance of the other. Since the folded-path buffer contains optical amplifiers, the propagation of ASE noise from the buffer to the switch fabric is inevitable. To mitigate this problem, FBGs [99] can be positioned in-between the buffer and the switch fabric (Figure 40). FBGs are special fibers with a periodic perturbation of the material refractive index along the direction of light propagation. These perturbations result in the formation of a grating in the fiber so that it will

reflect those wavelengths that satisfy the Bragg phase-matching condition will be reflected, while those that don't will be transmitted. The reader is referred to [99] for more details on FBG.

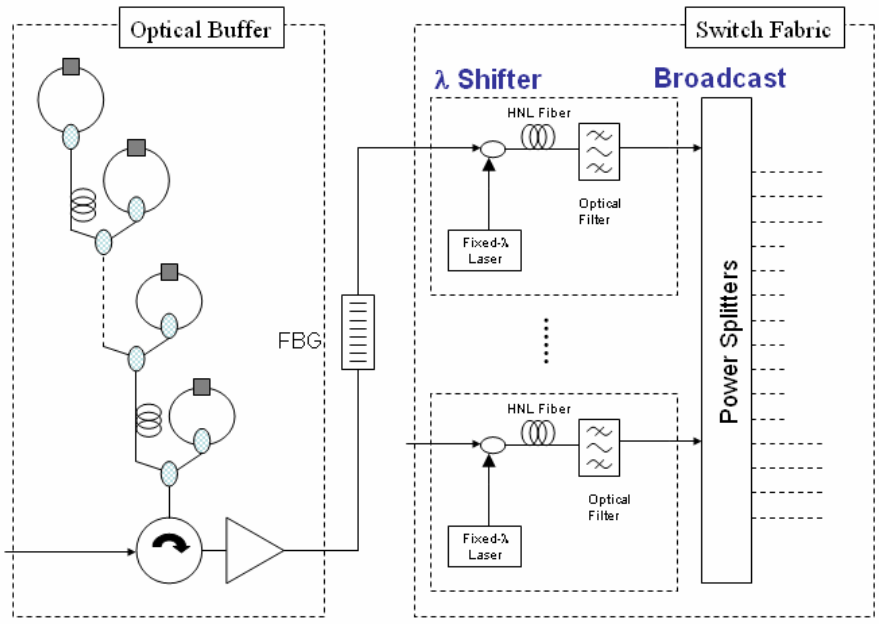

Figure 40. The FBG is inserted between the buffer and the switch fabric to reduce the ASE noise from the buffer.

As depicted in Figure 41, the center of the passband of the FBG can be made to coincide with the center frequency of the intermediate channels so that only the ASE noise within a narrow frequency spectrum centered around the intermediate channels is removed (Figure 41). Depending on the reflectivity of the grating, 95% to 99% of the ASE noise at the pre-shifted channel can be reflected before the signal enters the switch. The main advantage of using FBGs as compared to thin-film based filters is that FBGs usually have very low insertion losses outside their reflection band. Thus, the original channel and the pump will incur lower insertion loss, and this will result in a higher conversion efficiency during the FWM process.

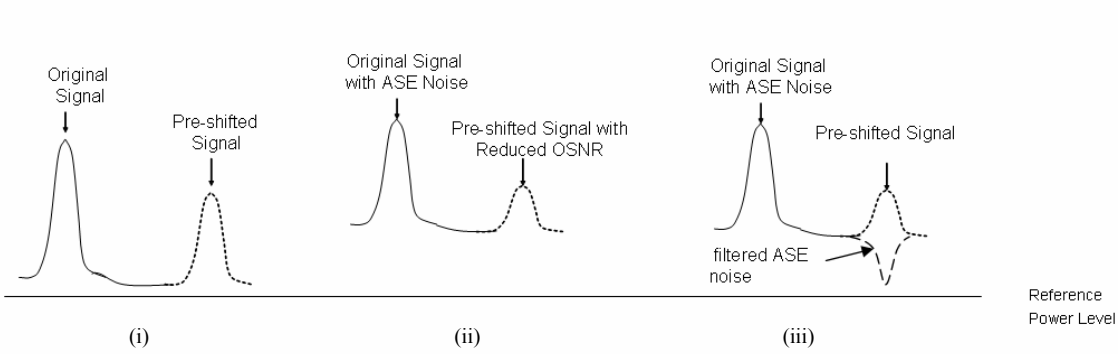

Figure 41. Power spectra of the original and the pre-shifted signal for different scenarios: (i) Without ASE noise from the buffer. (ii) With ASE noise from the buffer. (iii) With ASE noise from buffer but filtered by FBG

The proposed solution is easy to implement, and since the FBGs are passive and low in cost, the practicality of the technique is very high. Furthermore, this technique can also be implemented at the wavelength restoration stage of the switch.

6.2 Experimental Verification of the Proposed Solution

The experiment setup shown in Figure 42 will be used to study the effectiveness of noise reduction using the FBG.

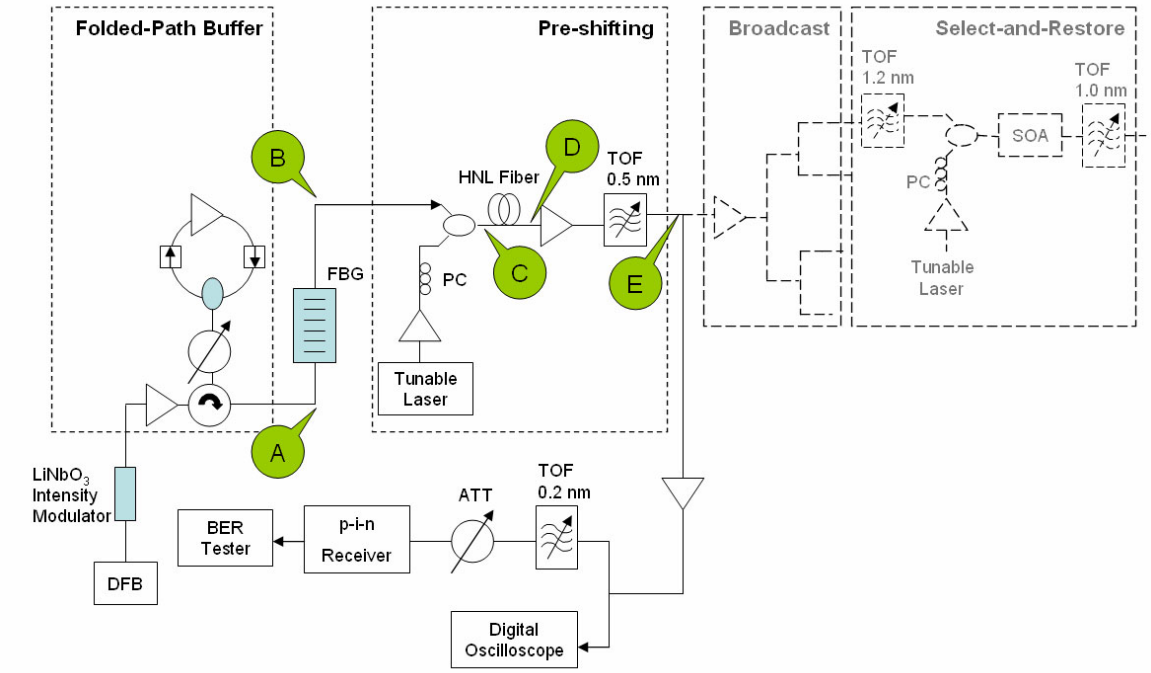

Figure 42. Experimental setup for measuring the performance of the integrated buffer-switch subsystem.

The setup comprises a section of the folded-path buffer and a portion of the gateless multicast switch fabric, and as is evident from Figure 42, the FBG is inserted between the buffer and the switch, at the position indicated by labels A and B. The FBG has an insertion loss of 0.8 dB and its reflectivity is 99% at 1554.66 nm. A 10 Gbit/s NRZ-OOK signal is generated using a $LiNbO_3$ external modulator using CW light from a DFB laser at 1558.56 nm. The modulated signal enters a section of the folded-path buffer and gets reflected from a bidirectional reflector positioned closest to the optical circulator. The SOA in the reflector is biased at 130 mA. Next, the signal passes through the FBG and enters the λ-shifter of the switch fabric. The signal undergoes wavelength conversion via the FWM process in a HNL dispersion shifted fiber. The 1 km long fiber has a nonlinear coefficient of 10.9 $W^{-1}km^{-1}$, a dispersion slope of 0.019 $ps/(nm^2.km)$ at 1550 nm, and a zero dispersion wavelength at 1561

nm. The pump (1556.66 nm) and signal powers before the HNL fiber are 9.6 dBm and 7.1 dBm, respectively. The converted signal at 1554.66 nm is filtered, re-amplified, and then filtered again before it undergoes optoelectronic conversion at the PIN receiver. Since the objective of the experiment is to measure the effectiveness of the FBG, it is not necessary for the signal to undergo another wavelength conversion process at the $n \times 1$ selector; the BER measurements for the converted signal are taken immediately after the λ shifting stage, at position indicated by label E in Figure 42.

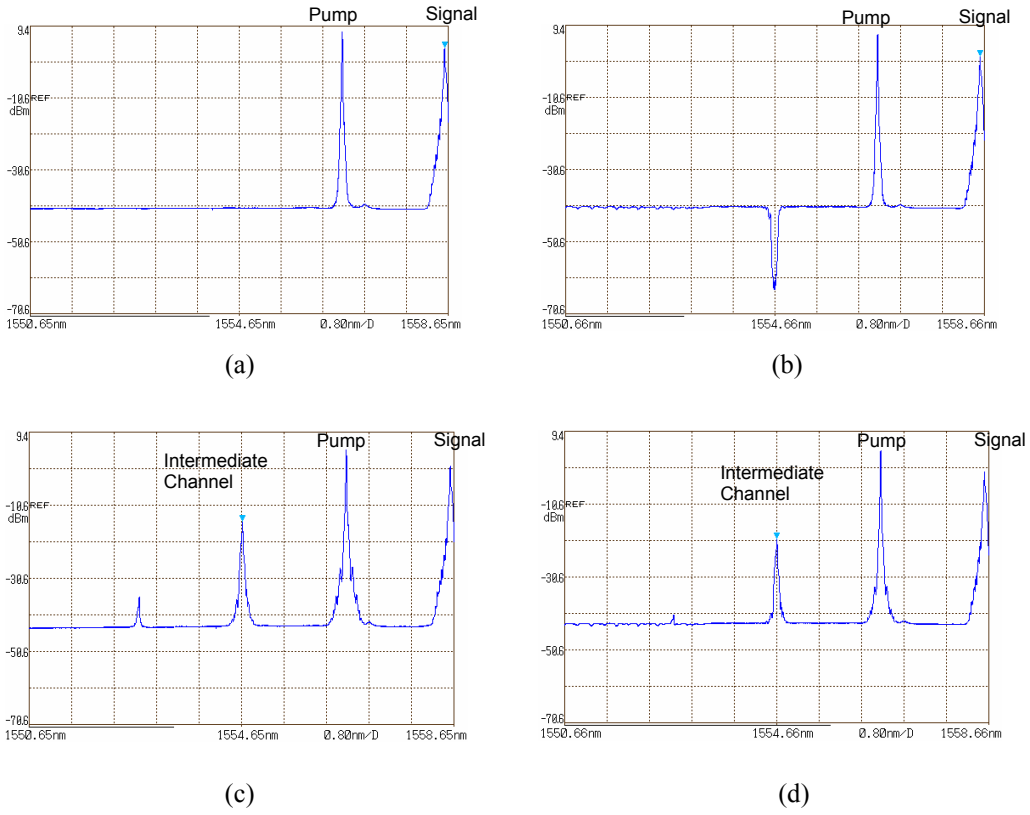

Figure 43. Optical spectra measured at different positions. (a) Before HNL fiber, without FBG. (b) Before HNL fiber, with FBG inserted (c) After HNL fiber, without FBG. (d) After HNL fiber, with FBG inserted.

The optical spectra measured at the position indicated by label C of Figure 42 are shown in Figure 43(a) and (b). By comparing the two figures, it is evident that after the FBG is inserted, the additional insertion loss introduced by the FBG is less than 1 dB. In addition, Figure 43(b) also shows that the reflection loss from the FBG is 23 dB at 1554.66 nm. Figure 43(c) and (d) show the optical spectra measured after the FWM process, at the position indicated by label D of Figure 42. Although the OSNR of the converted signal appears to be smaller after the FBG is inserted (Figure 43(d)), the BER performance depicted in Figure 44 shows that with the introduction of the FBG, the power penalty of the converted signal has actually decreased. This is an indication that the noise in the intermediate channel has actually decreased. Figure 44 also shows the BER performance of the signal at various locations. These measurements are taken immediately after the signal exits from the buffer, at the position indicated by label A in Figure 42 and after FWM at the position indicated by label D. Thus, it can be seen that with the introduction of the FBG, the power penalty can be reduced.

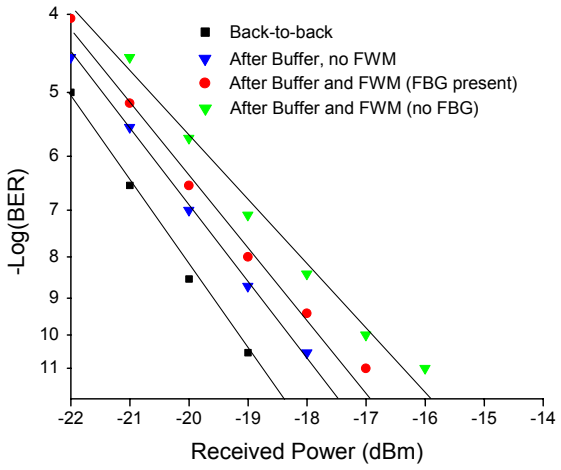

Figure 44. BER measurements of the converted signal, with and without the FBG inserted between the buffer and the switch.

6.3 Conclusions

In summary, the introduction of the FBG in-between the buffer and the switch has been shown to be effective in mitigating the negative effects of the ASE noise from the folded-path buffer. The technique works by reflecting part of the noise that has been transmitted from the buffer away from the switch before the actual switching occurs. For 10 Gbit/s signals, a 0.9 dB reduction in power penalty can be achieved. For practical OPS routers, the reflection profile of the FBG can be customized to take into account the differences in signal modulation formats and data bit-rates. In the next chapter, the performance of the folded-path buffer and the gateless multicast-capable switch at 40 Gbit/s will be examined in details.

Chapter 7 Performance of the Buffer and Switch at 40 Gbit/s

The folded-path buffer and the gateless multicast-capable switch fabric have been discussed individually in the previous chapters. These are critical components in an OPS router, and they exert tremendous influence on the signal integrity of the packet payload. One of the most important performance criteria is that these components must be transparent to the bit-rate and modulation format of the payload; both the buffer and switch fabric are expected to be compatible with payload bit-rates of at least 40 Gbit/s in the near future. The focus of this chapter is on the performance of the folded-path buffer and the gateless multicast-capable switch architecture at 40 Gbit/s. First, the performance of the ON-OFF reflectors will be experimentally characterized for three types of 40 Gbit/s signals that are modulated using different formats. Next, the concept of a hybrid optical router is introduced, and the gateless multicast-capable architecture will be modified so that it can be used as the fabric of such a router. In addition, the feasibility of this proposal will be examined via an experiment involving the switching of 40 Gbit/s signals.

7.1 Performance of ON-OFF Reflectors at 40 Gbit/s

The ON-OFF optical reflectors are the most critical component in the folded-path buffer, and their design and operating performance have been discussed in detail in Chapter 4. In this

section, an experiment that is designed to determine the performance of the reflectors at 40 Gbit/s will be described.

The experimental setup shown in Figure 45 is used to measure the performance of three different types of 40 Gbit/s signals as they pass through a folded-path buffer with only one section. The ON-OFF reflector is constructed using the bidirectional design as described in Chapter 4. The performances of the unidirectional and the Faraday reflectors can be inferred from the experiment results involving the bidirectional reflector.

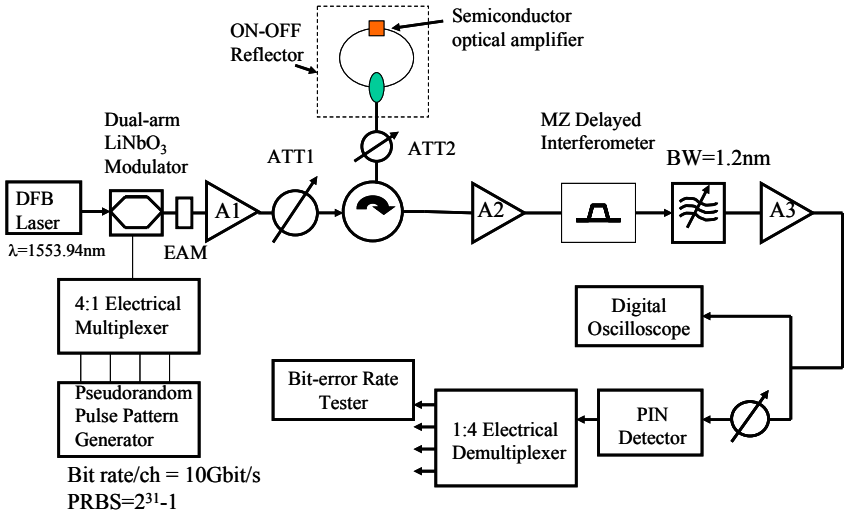

Figure 45. Experiment setup for measuring the performance of a single section of the folded-path buffer. The MZDI has an extra delay of 25 ps in one of its arm, and only one of its outputs is connected to the detector.

Continuous-wave (CW) light from a DFB laser is modulated using a dual-arm $LiNbO_3$ modulator, and depending on the bias voltage, ON-OFF-keyed (OOK) or differential phase shift keyed (RZ-DPSK) signals can be obtained. The modulator is driven by a 40 Gbit/s signal from a 4:1 electrical multiplexer. The multiplexer combines four 10 Gbit/s signal

channels from the pattern generator, and each channel has a PRBS length of 2^{31}-1. To generate RZ-OOK and RZ-DPSK signals, an electro-absorption modulator (EAM) that is driven by a 40 GHz sinusoidal RF signal is added after the $LiNbO_3$ modulator to act as a pulse carver. Next, the 40 Gbps optical signal is amplified, and then attenuated to 5 dBm to prevent large gain saturation in the SOA. Another attenuator (ATT2) is placed before the reflector to simulate the losses in the delay lines. In this experiment, only one reflector will be examined, and ATT2 is set so that the input power to the SOA is -10 dBm. This represents the actual attenuation loss in a buffer with 8 delay lines. After being reflected, the signal is filtered, detected and demultiplexed for BER measurements. Prior to photo-detection, the RZ-DPSK signal passes through a Mach-Zehnder delayed interferometer (MZDI); for NRZ-OOK and RZ-OOK measurements, the MZDI is removed. When separately measured at 1550 nm (and with bias current of 180 mA), the bulk type InP-InGaAsP SOA in the reflector has a small signal gain of 15 dB, output saturation power of 4.8 dBm, noise figure of 10 dB and polarization dependent gain of 0.2 dB. Throughout the experiment, the SOA bias current is maintained at 130 mA.

The measured BER performance for all the three 40 Gbit/s signals are shown in Figure 46. It is evident that the NRZ-OOK signal has the worst performance as it exhibits an error floor at BER of 10^{-9}. From the eye diagram of the signal measured at the receiver (Figure 47(b)), it can be seen that a high level of noise can be seen at the "1"s. This is predominantly a result of the effect of cross-gain modulation (XGM)-induced crosstalk when the signals propagate bidirectionally in the SOA.

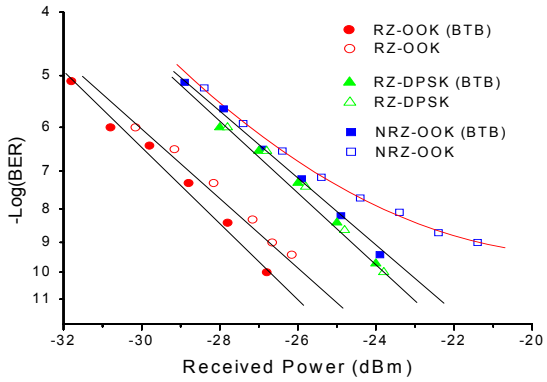

Figure 46. Measured BER performance of 40 Gbit/s signals. BTB: back-to-back measurements.

For RZ-OOK modulated signals, the influence of this crosstalk is reduced, as evident from the eye diagram in Figure 47(d). In this case, the value of the spatially averaged carrier density in the SOA fluctuates less from its mean value, because the carrier density variations cannot keep up with changes in the signal waveform.

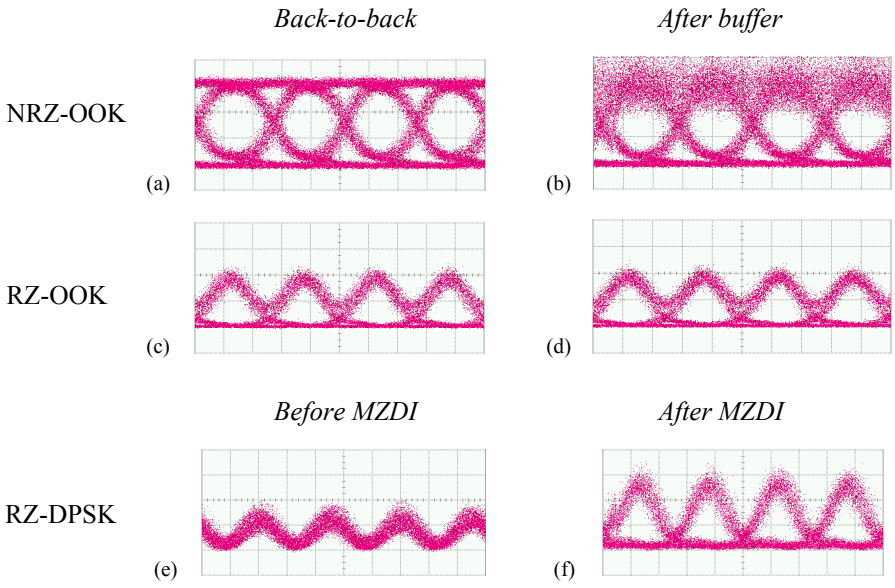

Figure 47. Measured eye diagrams (10 ps/div). (a) NRZ-OOK (back-to-back), (b) NRZ-OOK (after buffer), (c) RZ-OOK (back-to-back), (d) RZ-OOK (after buffer), (e) RZ-DPSK (before MZDI) and (f) RZ-DPSK (after MZDI).

Thus, there is correspondingly less fluctuations in the SOA gain, and the crosstalk is reduced. Figure 46 shows that error-free measurements can be obtained, and at a BER of 10^{-9}, the power penalty is less than 1 dB. The RZ-DPSK modulated signal has the best BER performance when compared to RZ-OOK and NRZ-OOK signals. In fact from Figure 46, the measured power penalty is negligible.

The phase noise in the SOA is caused by changes in the refractive index brought about by carrier density fluctuations, and these fluctuations result from intensity noise caused by induced emissions, non-radiative recombination and spontaneous emissions [66]. From the eye diagram of the RZ-DPSK signal measured before the MZDI (Figure 47 (e)), it is evident that the intensity fluctuation of the signal waveform is small and highly repetitive. It is possible that such small and rapid changes in the intensity may not have generated enough carrier density fluctuations that will lead to a phase noise that is large enough to be measured using the power penalty. This implies that the phase noise can be further reduced by using NRZ-DPSK signals, because for such signals, the waveform intensity is constant.

Thus, from the experimental results in this section, the folded-path buffer should be compatible with DPSK signals with bit-rates that are equal or greater than 40 Gbit/s. For NRZ-OOK signals, operating the buffer at 40 Gbit/s requires the use of a better reflector design such as the unidirectional reflector in order to eliminate the XGM-induced crosstalk noise [60]. From the simulation and experimental results presented in Chapter 4, the Faraday reflector is expected to have the worse performance even at 40 Gbit/s, and this can be attributed to the large noise factor in the SOA.

7.2 A Multicast-Capable Hybrid Optical Packet Switch

As discussed in Chapter 5, optical multicasting is poised to be an important function for future OPS routers, and in the same chapter, the concept of a hybrid optical router is also introduced. Existing proposals of the hybrid router [91, 92] utilizes an AWGR for switching. Unfortunately, such a design does not enable any multicasting or broadcasting functions within the switch fabric. Even if the design is modified to allow optical multicasting [94], such a service may not be available to all ports at all times. The gateless multicast-capable architecture that is discussed in Chapter 5 can provide truly non-blocking optical multicasting to all input ports. In this section, it will be slightly modified so that it will be compatible with a hybrid optical router.

The multicast-capable gateless switch architecture that is described in Chapter 5 can be easily implemented in a hybrid optical packet router. In the original architecture, the first step is a pre-shifting stage where the wavelengths of the incoming channels are shifted to different values so that each channel can be uniquely identified. However, this step can be eliminated since every ingress line card contains a laser, and the lasing wavelengths can be selected in such a manner so that no two lasers share a common wavelength. Thus, in this way, packets originating from different cards can be differentiated from one another.

Figure 48 depicts how an $n \times n$ switching fabric for a hybrid router can be designed using the gateless switch fabric [100].

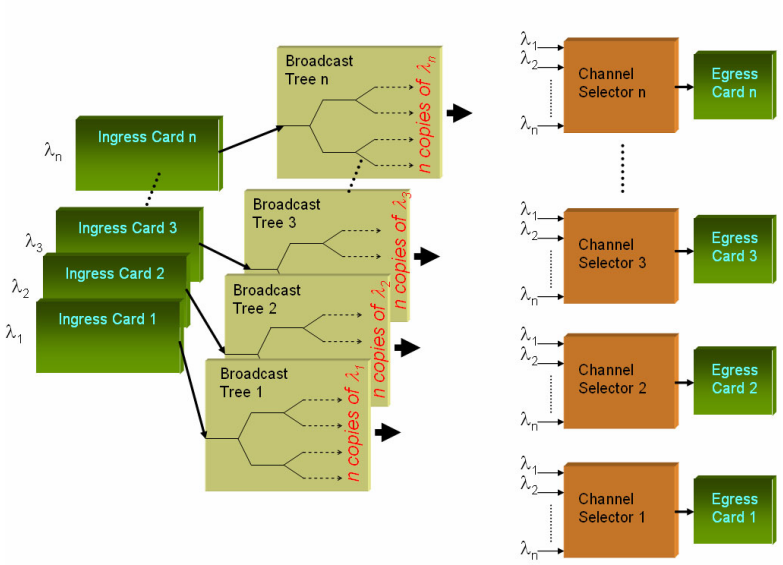

Figure 48. Implementing the gateless architecture in a hybrid router reduces the number of steps in the architecture.

The n distinct ingress cards are each assigned a unique wavelength so that n consecutive wavelength channels from λ_1 to λ_n are used. The inter-channel spacing is a parameter that can be optimised depending on a number of factors such as the port count, the properties of the channel selectors, and the tolerance for loss in the power splitting tree. The laser on each ingress card will be modulated so that the information carried in the payloads can be converted to optical signals. Next, each of the modulated signals from every card will enter a power splitter tree. Such a passive device can be easily constructed using fused-fiber couplers connected in a tree like structure. The power splitter tree performs the broadcast function as described in Chapter 5. If there are n output cards, the splitting ratio of the tree will be 1:n. After the signal is duplicated n times in the tree, each will be distributed to the n respective channel selectors.

From Figure 48, it is evident that each channel selector will see the n different signals (λ_1 to λ_n) from all ingress cards. Out of these n channels, only one can be selected at one time, and this is because of the technique that is used to implement the channel selector. As described in Chapter 5, the channel selector comprises an AWG, a tunable laser, a power combiner and a set of HNL fibers; the selection process is based on the FWM wavelength conversion in the HNL fiber and thus, only one channel can be selected at any time. If two or more channels are to be switched to the same egress card, a contention will occur and the buffers will have to be used to resolve the problem. An alternative solution would be to use some other techniques to implement the channel selector, so that two or more channels can be selected simultaneously. Thus, in such systems, the buffers will not be required.

After the channels are being selected, they will proceed to the egress cards where they may undergo further signal reconditioning or additional buffering. An advantage that can be gained by implementing the gateless architecture in a hybrid router is that a wavelength restoration stage is not required. In the original architecture, wavelength restoration is performed simultaneously with the channel selection because after that, the packet will exit the router and proceed to the next destination. But if egress cards are used, the optical packets from the switch fabric will be converted to electrical signals once again before exiting from the router. Thus, if a tunable or fixed-wavelength laser is present at the egress card, the wavelength restoration can be performed by tuning and then selecting an appropriate lasing wavelength through this laser. Therefore, the wavelength of the switched packet from the fabric is no longer a concern.

With this new scheme, there are two advantages that can be gained. First, the power combiners can be replaced by AWGs, and this will result in lower insertion losses. Second, there is now a larger range of wavelengths available for designating the pump of the channel selector. Such flexibility is important in the FWM wavelength conversion process, since the conversion efficiency usually decreases as the pump-signal detuning increases [101, 102]. By keeping the signal-pump detuning small, more intermediate channels can be accommodated, and this will result in a higher port count.

7.3 Experimental Characterization of the Hybrid Packet Switch at 40 Gbit/s

An experiment has been devised to characterize the performance of the buffer-switch subsystem at 40 Gbit/s. Figure 49 shows the experimental setup for measuring the static switching performance of a 4 x 4 fabric based on the gateless broadcast-and-select architecture discussed in Chapter 5. It is assumed that the optical signals entering such a router would already have been converted to electrical signals, buffered and then regenerated at the input ports. Typically, these ports are implemented in the form of ingress line cards as discussed in Section 7.2. Furthermore, it is also assumed that after switching, the signal will be photodetected at the egress line card, regenerated, and then converted back to optical form before leaving the router. Since the switching principle is the same for all ports, only one input and one output fiber will be selected for measurement (Figure 49).

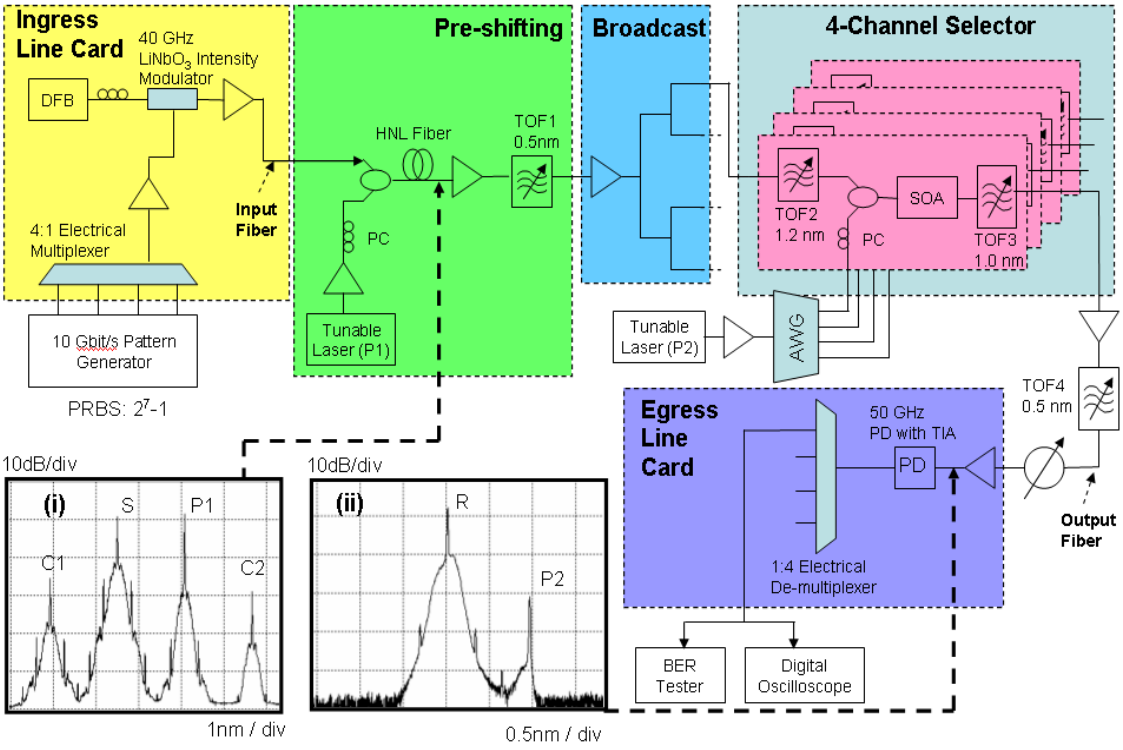

Figure 49. Experimental setup for 40 Gbit/s measurements. Insets (i) and (ii): Optical spectra measured at various points.

A 40 Gbit/s electrical signal is first generated by combining four 10 Gbit/s signals (PRBS of 2^7-1) using an electrical multiplexer. The multiplexed signal is then used to modulate a CW light (1556.5 nm) from a DFB laser using a 40 GHz $LiNbO_3$ intensity modulator. The next step is to differentiate this input signal (S) from the other three, assuming that all of them occupy the same wavelength channel initially. This is achieved by performing a wavelength conversion so that the wavelength of this input channel is shifted to a new value. The same procedure will have to be applied to the other three channels, but each of the converted signals occupies different channels, and the channels have to be in consecutive order with fixed channel spacing. The channel spacing is a design parameter that has to be optimised.

Note that as mentioned in Section 7.2, this pre-shifting step can be eliminated if it is assumed that each line card has a laser and a modulator, and that no lasing wavelengths are identical. Nevertheless, in this experiment it will be shown that even if the pre-shifting stage is applied, the power penalty remains small.

Four-wave mixing is chosen as the wavelength conversion technique for the pre-shifting stage since it is transparent to the bit-rate and modulation format of the signals. In this experiment, a highly nonlinear fiber is used as the medium for FWM. The 1 km long fiber has a nonlinear coefficient of 10.9 $W^{-1}km^{-1}$, a dispersion slope of 0.019 ps/(nm^2.km) at 1550 nm, and a zero dispersion wavelength at 1561 nm. Inset (i) of Figure 49 depicts the optical spectra of the 1558.1 nm pump (P), the signal channel (S), and the converted channels (C1 and C2) measured at the output of the HNL fiber. In the full implementation of the switch, the same FWM wavelength conversion will have to be carried out in the other three HNL fibers for the remaining input signals. After FWM, the pump, the original signal, and the converted signal C2 are filtered out, leaving only C1, the intermediate channel.

The next step is to broadcast C1 to all the output ports. The signal is first amplified using an EDFA before entering a 1:4 power divider. Such power dividers can be easily constructed from fused-fiber couplers. This broadcast procedure will have to be carried out for all the other intermediate signals in the switch so that eventually, each output port will see all the four intermediate channels. As shown in Figure 49, only one out of the four output ports is selected for measurement. Furthermore, at every output port only one out of the four input channels can be selected at any time. In broadcast-and-select architectures [89, 95], SOAs are

used as ON-OFF gates to select one of these channels. But as mentioned in [96], the same function can be achieved without using any of these gates.

The gateless channel selection scheme utilizes a wavelength conversion step followed by optical filtering. In this case, FWM is also used for wavelength conversion, but because of resource constraints, a bulk type InP-InGaAsP SOA is used as the conversion medium in place of a HNL fiber. The SOA is biased at 250 mA, and it has a small signal gain of 15 dB and output saturation power of 5 dBm at 1550 nm. As depicted in Figure 49, a tunable laser that is used as the pump (P2) for the FWM process is connected to an arrayed waveguide grating (AWG). The output of the AWG is in turn connected to every SOA via a 3 dB coupler. Each of the four intermediate channels is also connected to one SOA to facilitate the FWM process. When the wavelength of the laser is changed, the pump (P2) appears at the input port of different SOAs. Wherever the pump (now 1554 nm) is present, wavelength conversion is performed in the SOA, and a copy of the intermediate channel (labeled as R in inset (ii) of Figure 49) is obtained. A bandpass filter (TOF3) positioned after the SOA filters out the pump and the intermediate channel leaving only R to proceed to the detector. For the remaining SOAs, since no pump is present, the intermediate channels will be filtered out and only noise will be present after the filters.

Since this switch fabric is now part of an electronic router, it does not matter if the final wavelength of the switched channel is different from its original. Thus, there is no need to restore the original wavelength of the signal. In addition, the power combiners that are previously required in the original gateless multicast architecture [96] are now unnecessary.

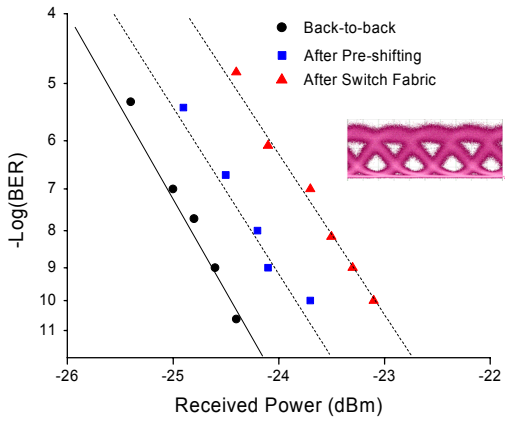

Figure 50. BER performance for 40 Gbit/s NRZ-OOK signal. Inset: eye diagram after two wavelength conversions (10 ps/div).

Instead, the output of the SOAs can be connected to an AWG, provided that the channel spacing of the AWG matches the channel separation of the intermediate signals. The replacement of the power combiner with an AWG will result in better OSNR at the detector and thus improving the scalability of the design. Note that the AWG is not included in this experiment, but its effect is simulated by a tunable bandpass filter (TOF4) with a 3 dB bandwidth of 0.5 nm and a loss of 5 dB.

At the egress line card, a 50 GHz photodetector with a preamp is used to detect the signals. Figure 50 shows that BER performance of the switch at 40 Gbit/s. After the pre-shifting stage, the converted signal incurred a power penalty of 0.6 dB at BER of 10^{-9}. After both wavelength conversions, the power penalty becomes 1.4 dB at the same BER, and no error floor is observed. From inset (ii) of Figure 49, the OSNR of the received signal is more than 50 dB.

7.4 Conclusions

The 40 Gbit/s performance of the folded-path buffer and the gateless multicast-capable switch is discussed in this chapter. An experiment involving a folded-path buffer with bidirectional ON-OFF reflectors shows that the reflector is compatible with 40 GBit/s signals that are modulated using RZ-OOK and NRZ-DPSK formats. For NRZ-OOK signals, an error floor is observed in the BER measurements, and this is due to the XGM-induced crosstalk noise in the SOA of the reflector.

The very low power penalty incurred by the NRZ-DPSK signals in the buffer is a strong indication that the folded-path buffer can support signals with bit-rates that are even greater than 40 Gbit/s. Since the experiment is conducted using bidirectional reflector, it is strongly believed that a better performance can be obtained by using the unidirectional reflectors because the latter has lower phase noise and an almost non-existent XGM-induced crosstalk noise.

For the gateless switch architecture, a proposal to modify the original design for adaptation to a hybrid optical router was described and experimentally tested. Experimental results show that after switching, the power penalty is 1.4 dB at a BER of 10^{-9}, and this is within an acceptable range for 40 Gbit/s signals. Moreover, the OSNR of the switched signal is 50 dB, and this shows that the port count of the switch can be increased. Many advantages can also be obtained by using the gateless switch architecture in the hybrid router. Besides providing the truly-nonblocking multicasting and broadcasting functions that existing AWGR-based

fabrics are not able to, the presence of lasers on both the ingress and egress cards in such routers helped to reduce the number of components required to implement the architecture. Thus, both the folded-path buffer and the gateless multicast-capable architecture are well suited for near-term and long-term future optical routers operating at 40 Gbit/s and beyond.

Chapter 8 Conclusions and Future Work

Accomplishments

A novel optical buffer and a multicast-capable optical switch fabric have been proposed and experimentally demonstrated. The optical buffer is based on a unique folded-path power distribution tree comprising optical couplers and fiber delay lines. By exploiting the bidirectional propagation of light in this structure, redundant delay lines that are commonly found in feed-forward optical buffers are eliminated. As a result, the folded-path buffer is the most physically compact feed-forward buffer demonstrated to date. This is attractive to system designers because the cost and space required for its implementation can be reduced.

A unique feature of the folded-path buffer is the high-speed optical ON-OFF reflectors. It is the first time that a concept of an electrically controllable loop-mirror optical reflector is proposed and experimentally demonstrated. Using the SOA as an optical ON-OFF switch, the reflector can be switched ON or OFF within nanoseconds, and by deploying many of such reflectors in the folded-path delay tree, the delay provided by the buffer can be dynamically reconfigurable. The nanoseconds reconfigurability is an important requirement for components in an optical packet router, and experimental results showed that the folded-path buffer can reconfigure its delay in less than 10 ns.

The switching characteristics and the design of the ON-OFF reflectors exert a significant influence on the performance of the buffer. Three different types of reflectors have been studied: unidirectional, bidirectional and Faraday. The performance of the Faraday reflector is the worst because of the high noise factor and the XGM-induced crosstalk noise caused by bidirectionally propagating signals in the SOA. The bidirectional reflector also suffers from the crosstalk problem but it has a relatively lower noise factor. The unidirectional reflector has the best performance since it is immune to XGM-induced crosstalk. Moreover the phase noise from this reflector is also the smallest since the signals only propagate unidirectionally in the SOA.

Based on simulation and experimental results, the performance of the unidirectional reflector is further optimized. In particular, it has been found that an optimal bias current exists for the SOA in the reflector. If the current is too low, the reflector does not provide enough gain to compensate for the losses in the folded-path tree. On the other hand, excessive currents will result in a reduced device lifetime. Experimental results also show that temperature control within the SOA can cause a difference in the OSNR of the signals that are reflected because of Auger recombinations in the SOA. The optimization of bias current will enable the designer to maximize the performance of the buffer by reducing the ASE noise and increasing the range of delays that can be provided.

Simulations and measurement results indicate that the buffer architecture is scalable and flexible. Up to four sections of the buffer have been cascaded and the experiment results show that both intensity and phase-modulated signals can be accommodated in the buffer.

The power penalty incurred by a signal that is stored in such multi-section buffer is also within an acceptable value. In addition, design optimization shows that up to eight delay lines can be used in a single section and four sections of the buffer can be cascaded if the power penalty of the buffer is to be kept within 2 dB. Thus, a total of 32 delay lines can be used and consequently, the range of delay values can be very large: from a few nanoseconds to tens of microseconds. Alternatively, if desired, the range of delay can be kept small so that the delay granularity will be higher.

To demonstrate the flexibility of the folded-path architecture, the original design is modified to include both buffering and wavelength conversion capabilities. This has been realized by replacing one of the delay lines in the buffer with a highly nonlinear fiber. Using this fiber and a pump laser, the four-wave mixing wavelength conversion technique is used to simultaneously convert the wavelengths of four optical packets in the buffer. This is also the first time that a multi-functional buffer has been experimentally demonstrated.

A gateless multicast-capable optical switch fabric is proposed as part of this research. Although there are existing switch fabrics that can perform optical multicasting, they do not allow all the input ports to use this functionality at all times. Only broadcast-and-select architectures provide optical multicasting or broadcasting for all ports in a truly-nonblocking manner, but a very large number of ON-OFF optical gates are required. The gateless switch architecture proposed in this thesis demonstrated that it is possible to provide optical multicasting services to all ports at all times without using a single ON-OFF gate. Through a dual stage wavelength shifting process, incoming wavelength channels can be identified,

broadcasted and selected. A four-port switch fabric using this concept has been experimentally demonstrated at 10 Gbit/s, and the worst case power penalty is 1.5 dB at a BER of 10^{-12}.

The folded-path buffer and the gateless switch fabric are also integrated by using a noise reduction technique involving an FBG. By aligning the center wavelength of the FBG with the wavelength of the intermediate channel, some of the ASE noise from the buffer can be reflected away from the switch fabric before the switching takes place. Experimental results show that the ASE noise from the buffer has been suppressed, resulting in a smaller power penalty for the switched signal. Compared to thin film filters, using the FBG has the advantage of a smaller insertion loss outside the reflection band. Consequently, the FWM process used in the switch can have better conversion efficiency because the signal power is higher.

For a functional OPS router, the proposed buffer and switch are expected to support signals with bit-rates of 40 Gbit/s or higher. Experimental results show that the bidirectional ON-OFF reflectors in the buffer imposed no power penalty on constant-intensity phase modulated signals at 40 Gbit/s. However, for intensity-modulated signals, the XGM-induced crosstalk noise results in very large power penalties, and thus the unidirectional reflector should be used instead.

The multicast-capable switch architecture is modified for use in a hybrid optical router. In this case, some components that are required in the original architecture can be eliminated,

and this results in an even more cost efficient and physically compact switch fabric. A 40 Gbit/s intensity-modulated signal is used to test the performance of a four-port gateless multicast-capable switch in a hybrid router. Experimental results show that error-free switching can be achieved with 1.4 dB of power penalty at BER of 10^{-9}.

Future Work

The research work presented in this thesis offers alternatives for implementing the optical buffer and a multicast-capable switch fabric. However, many challenges must be overcome before the proposed solutions can be implemented in a practical optical router. The following are some areas that could benefit from further research:

1. For small delay values, the length of the fiber delay lines in the folded-path buffer is still within reasonable values, when viewed in terms of the ease of product packaging and storage. However, for long delays above a few microseconds, the physical size of the buffer becomes highly impractical. A potential solution is to replace the fiber delay lines with interconnects that are based on the slow-light technology [43-49]. The new buffer would still be reconfigurable and yet its physical size can be much smaller.

2. The folded-path buffer utilizes an SOA in the optical ON-OFF reflector for switching. In a WDM environment, the number of SOA required increases rapidly as the number

of wavelength channels scales up. Thus, an alternative low-power and low-cost optical switch is required. However, the switch must be able to turn ON and OFF within several nanoseconds. Moreover, the ON-OFF extinction ratio should also be greater than 50 dB.

3. The folded-path architecture can be used with integrated optical waveguides to form a buffer on a much smaller scale. The fiber delay lines can be replaced by integrated optical waveguides, and multimode interference (MMI) splitters [103, 104] can be used in place of the fused-fiber couplers. Even the optical circulators can be implemented using integrated optics [105], and because the buffer architecture is based on a folded-path topology, the resulting design will reduce the required area occupied by the delay lines by half. Thus, the fabrication yield is expected to be better as the chip area is now smaller.

4. The gateless multicast-capable switch fabric utilizes highly nonlinear fibers that are 1 km in length. An alternative is to use highly nonlinear photonic crystal fibers that are much shorter [64]. By doing so, the time the packet spends in the router can be tremendously reduced, and this will result in lower end-to-end network latencies.

5. The broadcast-and-select concept used by the gateless multicast-capable switch fabric has a major drawback even though it is easy to implement: all packets are continuously broadcasted to all output ports even though some ports may not be the intended destination for the packets. Thus, power wastage in the fabric is high. The

ideal solution would be to construct a dynamically reconfigurable broadcast tree to channel the optical power to only the required output ports. The energy consumed by such a tree should be smaller than that wasted by the passive splitter tree.

Conclusions

The above results demonstrate that both the folded-path buffer and the gateless switch fabric can be readily implemented with existing optical components, and that good performances can be obtained by optimizing these components. From the experimental results, both designs are shown to be transparent to the modulation format and bit-rate of the incoming signals up to 40 Gbit/s. Moreover, the flexibility of both designs has also been demonstrated. The folded-path buffer is modified to support both buffering and wavelength conversion functions simultaneously. In addition, the gateless multicast architecture can be simplified for use in a hybrid optical router. Thus, with such flexibility and scalability, the folded-path buffer and the gateless switch fabric are viable solutions for the terabit all-optical packet routers of the future.

Appendix

In this chapter, the simulation model for the bulk InP-InGaAsP SOA that is discussed in Chapter 4 will be described in details. The device geometry is assumed to be similar to that described in [106], and the active region is divided into smaller sections of equal length (Δz) along the signal propagating direction, z. It is found that dividing the active region into 15 sections is a good compromise between simulation speed and accuracy. The carrier density in each section is described by the rate equation [67]

$$\begin{aligned}\frac{dn(z)}{dt} &= \frac{I}{edLw} - R\left(n(z)\right) \\ &- \frac{\Gamma}{dw}\left\{g\left(n(z),\nu\right)\left[N_s^+(z) + N_s^-(z)\right]\right\} \\ &- \frac{2\Gamma}{dw}\left\{\sum_{j=0}^{N_j-1} g\left(n(z),\nu_j\right)\left[N_j^+(z) + N_j^-(z)\right]\right\}\end{aligned} \tag{24}$$

where *R(n)*, the carrier recombination rate, is given by

$$R(n) = \left(A_{rad} + A_{nrad}\right)n + \left(B_{rad}\right)n^2 + C_{aug}n^3 \tag{25}$$

, where A_{rad} and C_{aug} are the linear radiative and Auger recombination coefficients, respectively (see Table II for their values). Under steady-state conditions, $\frac{dn(z)}{dt} = 0$, and the carrier density for each section is obtained after solving the rate equation iteratively. When the change in *n(z)* is smaller 0.01%, the iteration is stopped. In (24), all of the current that is injected into the SOA is assumed to flow through the active region of the device. Leakage

current is neglected, as its calculation requires detailed knowledge of material properties such as doping concentrations, which are not available at the time of simulation [107]. In the same equation, *g(n, ν)* is the parabolic gain described in (1) while $N_s^+ = \left|E_s^+\right|^2$ and $N_s^- = \left|E_s^-\right|^2$ are the signal photon rates at the section boundaries. The complex-valued traveling-waves, E_s^+ (forward propagating) and E_s^- (backward propagating), are obtained by solving their wave propagation equations for every section. The solutions to these equations at the section boundaries are given by

$$E_s^+(i+1) = E_s^+(i)\exp\left(-j\beta\Delta z\right). \exp\left\{\frac{1}{2}\left[\Gamma g\left(n(i),\nu\right) - \alpha\left(n(i)\right)\right]\right\} \tag{26}$$

$$E_s^-(i) = E_s^-(i+1)\exp\left(-j\beta\Delta z\right). \exp\left\{\frac{1}{2}\left[\Gamma g\left(n(i),\nu\right) - \alpha\left(n(i)\right)\right]\right\} \tag{27}$$

where $E_s^{\pm}(i)$ refers to the wave at the start of the *i*th section, $j = \sqrt{-1}$, and β is given by

$$\beta = \frac{2\pi n_{eff}\nu}{c_0} \tag{28}$$

where n_{eff} is the effective index of the guided mode in the waveguide, and c_0 is the speed of light in vacuum. Applying boundary conditions that are determined by the signal input power and the facet reflectivities, the forward traveling wave for each section boundary is calculated

first, progressing from $z = 0$ to $z = L$. After that, the backward traveling wave is calculated in the reverse order.

The inclusion of spontaneously emitted noise in the rate equation of (24) is via the normalized noise photon rates, N_j^+ and N_j^-, in both transverse electric (TE) and transverse magnetic (TM) polarization modes, thereby resulting in a factor of 2 in the last term of (24). As in [67, 68], the spontaneous emission is represented by noise photons at discrete frequencies that are determined by longitudinal cavity modes. These frequencies, ν_j, where $j = 0..N_j\text{-}1$, are separated from each other by the same frequency spacing, and they span the entire gain bandwidth of the SOA. The solutions to the wave equations for spontaneous emission in each section of the amplifier can be expressed as

$$N_j^+(i+1) = \exp\left(\gamma_{i,j}\Delta z\right)\left\{\frac{U_j R_{sp}\left(n(i),\nu_j\right)}{\gamma_{i,j}}\left[1-\exp\left(-\gamma_{i,j}\Delta z\right)\right] + N_j^+(i)\right\} \tag{29}$$

$$N_j^-(i) = \exp\left(\gamma_{i,j}\Delta z\right)\left\{\frac{U_j R_{sp}\left(n(i),\nu_j\right)}{\gamma_{i,j}}\left[1-\exp\left(-\gamma_{i,j}\Delta z\right)\right] + N_j^-(i+1)\right\} \tag{30}$$

where

$$\gamma_{i,j} = \Gamma g\left(n(i),\nu_j\right) - \alpha\left(n(i)\right) \tag{31}$$

and U_j, the normalization factor, is given by [67]

$$U_j = \left\{ 1 + \left[\frac{4G_s\left(\nu_j\right)R}{\left[1 - RG_s\left(\nu_j\right)\right]^2} \right]^2 \right\}^{-0.5} . \tag{32}$$

Following the notation for the signal photon rates, $N_j^{\pm}(i)$ in (29) and (30) refer to the normalized noise photon rates at the start of the *i*th section. In the same equations, R_{sp} is the spontaneously emitted noise given by

$$R_{sp}\left(n(i), \nu_j\right) \approx \Gamma g\left(n(i), \nu_j\right) \Delta\nu \tag{33}$$

where $\Delta\nu$ is the spacing between the noise resonance frequencies. In the calculation of R_{sp}, the gain coefficient in [67], which does not include material absorption, has been approximated by the net gain, $g\left(n, \nu_j\right)$, which includes both the material gain and absorption. This is because the material bandgap energy that is used to compute the original gain coefficient is unavailable. For the wavelength range of 1540 nm to 1570 nm considered for all simulations in this paper, this approximation is expected to result in only small underestimation of the output ASE noise. This is because the material absorption is more significant at shorter wavelengths [108].

It is to be noted that for the calculation of the noise figure in (23), the frequency-normalized form of N_j^+ is given by

$$\tilde{N}_j^+(L) = \frac{N_j^+(L)}{\Delta\nu}. \tag{34}$$

In (24), both the signal and noise photon rates are recalculated each time the value of *n(z)* changes. After *n(z)* converges, the output ASE spectral density is then obtained according to [67].

References

[1] E. G. Rawson and R. M. Metcalfe, "Fibernet: multimode optical fibers for local computer networks," *IEEE Trans. Comm.*, vol. 26, no. 7, pp. 983-990, Jul. 1978.

[2] S. Tamura, S. Nakano, and K. Okazaki, "Optical code-multiplex transmission by Gold sequences," *IEEE. J. Lightwave Technol.*, vol. LT-3, no. 1, pp. 121-127, Feb. 1985.

[3] P. Pruncal, M. Santoro, and T.R. Fan, "Spread spectrum fiber-optic local area network using optical processing," *IEEE. J. Lightwave Technol.*, vol. LT-4, no. 5, pp. 547-554, May 1986.

[4] P. Pruncal, D. J. Blumenthal, and P. A. Perrier, "Photonic switch with optically self-routed bit-switching," *IEEE Commun. Mag.*, vol. 25, no. 5, pp. 50-55, 1987.

[5] D.J. Blumenthal, P.R. Pruncal, L. Thylen, and P. Granestrand, "Performance of 8x8 LiNbo3 switch matrix as a giga-hertz self routing switching node," *Electron. Lett.*, vol. 23, no. 25, pp. 1359-1360, 1987.

[6] P. E. Green *et al.*, "All-optical Packet-switched Metropolitan-Area network proposal," *IEEE J. Lightwave Technol.*, vol. 11, no. 5/6, pp. 754-763, May/June 1993.

[7] F. Masetti *et al.*, "High speed, high capacity ATM optical switches for future telecommunication transport network," *IEEE J. Select. Areas Commun.*, vol. 14, no. 5, pp. 979-997, June 1996.

[8] C. Guillemot *et al.*, "Transparent optical packet switching: The European ACTS KEOPS project approach," *IEEE J. Lightwave Technol.*, vol. 16, no. 12, pp. 2117-2134, Dec. 1998.

[9] P. Gambini *et al.*, "Transparent optical packet switching: network architectures and demonstrators in the KEOPS project," *IEEE J. Lightwave Technol.*, vol. 16, no. 7, pp. 1245-1259, Sept. 1998.

[10] D. J. Blumenthal *et al.*, "All-optical label swapping networks and technologies," *IEEE J. Lightwave Technol.*, vol. 18, no. 12, pp. 2058-2075, Dec. 2000.

[11] B. Meagher *et al.*, "Design and implementation of ultra-low latency optical label switching for packet-switched WDM networks," *IEEE J. Lightwave Technol.*, vol. 18, no. 12, pp. 1978-1987, Dec. 2000.

[12] L. Dittmann *et al.*, "The European IST project DAVID: A viable approach toward optical packet switching," *IEEE J. Select. Areas Commun.*, vol. 21, pp. 1026-1040, Sept. 2003.

[13] N. Wada, H. Harai, and F. Kubota, "40Gbit/s, multi-hop optical packet routing using optical code label processing based packet switch prototype," in *Proc. IEEE / OSA Optical Fiber Commun. Conf. (OFC)* Atlanta, 2003, paper FO7.

[14] O. Leclerc *et al.*, "Optical regeneration at 40 Gb/s and beyond," *IEEE J. Lightwave Technol.*, vol. 21, no. 11, pp. 2779-2790, 2003.

[15] W. L. Ha, R. M. Fortenberry, and R.S. Tucker, "Demonstration of photonic fast packet switching at 700Mbit/s data rate," *Electron. Lett.*, vol. 27, no. 10, pp. 789-790, 1991.

[16] W. Wang, L. G. Rau, and D. J. Blumenthal, "160Gb/s variable length packet / 10Gb/s- label all-optical label switching with wavelength conversion and unicast/multicast operation," *IEEE J. Lightwave Technol.*, vol. 23, no. 1, pp. 211-218, Jan. 2005.

[17] R. Takahashi and H. Suzuki, "1-Tb/s 16-bit all optical serial-to-parallel conversion using a surface-reflection optical switch," *IEEE Photon. Tech. Lett.*, vol. 15, no. 2, pp. 287-289, 2003.

[18] H. Uenohara, T. Seki, and K. Kobayashi, "Investigation of high-speed wavelength routing and bit-error-rate performance of an optical packet switch with an optical digital-to-analog conversion-based header processor," *IEEE Photon. Tech. Lett.*, vol. 16, no. 3, pp. 951-952, Mar. 2004.

[19] M. Hickey and L. Kazovsky, "The STARNET coherent WDM computer communication network: Experimental transceiver employing a novel modulation format," *IEEE J. Lightwave Tech.*, vol. 6, pp. 876-884, May 1994.

[20] J. Zhang, N. Chi, P.V. Holm-Nielsen, C. Peucheret, and J. Jeppesen, "A novel optical labeling scheme using a FSK modulated DFB laser integrated with an EA modulator," in *Proc. IEEE / OSA Opt. Fiber Commun. Conf. (OFC)*, Atlanta, GA, 2003, paper TuQ5.

[21] N. Chi at al., "Experimental demonstration of cascaded transmission and all-optical label swapping of orthogonal IM/FSK labeled signal," *Electron. Lett.*, vol. 39, no. 8, pp. 676-678, Apr. 2003.

[22] N. Chi et al., "Optical label swapping and packet transmission based on ASK/DPSK orthogonal modulation format in IP-over-WDM networks," in *Proc. IEEE / OSA Opt. Fiber Commun. Conf. (OFC)*, Atlanta, GA, 2003, paper FS2.

[23] Y. M. Lin, M. C. Yuang, S. L. Lee, and W. I. Way, "Using superimposed ASK label in a 10Gbit/s multihop all-optical label swapping system," *IEEE J. Lightwave Tech.*, vol. 22, no. 2, pp. 351-361, Feb. 2004.

[24] E. N. Ellas, N. Skarmoutsos, and D. Syvridis, "An optical FSK-based label coding technique for the realization of the all-optical label swapping," *IEEE Photon. Tech. Lett.*, vol. 14, no. 10, pp. 1472-1474, Oct. 2002.

[25] N. Deng, Y. Yang, C. K. Chan, W. Hung, and L. K. Chen, "Intensity-modulated labeling and all-optical label swapping on angle-modulated optical packets," *IEEE Photon. Tech. Lett.*, vol. 16, no. 4, pp. 1218-1220, Apr. 2004.

[26] C. Chow and H. K. Tsang, "Optical packet label using polarization shift keying (PolSK) label and amplitude shift keying (ASK) payload," in *Proc. IEEE / OSA Opt. FIber Commun. Conf. (OFC) 2005*, Anaheim, CA, Mar. 2005, paper OME73.

[27] C. J. Moss *et al.*, "Experimental results for fast, high-capacity optical switching architectures," in *Proc. Topical Meet. On Photonics in Switching*, Palm Springs, CA, 1993, paper PWB4-1.

[28] A. Okada, "All-optical packet routing in AWG-based wavelength routing networks using out-of-band optical label," in *Proc. IEEE / OFC Optical Fiber Commun. Conf. (OFC)*, Washington, D.C., 2002, paper 216-217.

[29] Z. Zhu, V. J. Hernandez, M. Y. Jeon, J Cao, Z. Pan, and S.J. Ben Yoo, "RF photonics signal processing in subcarrier multiplexed optical-label switching communications systems," *IEEE J. Lightwave Technol.*, vol. 21, no. 12, pp. 3155-3166, Dec. 2003.

[30] G H. Smith and D. Novak, "Broad-band millimeter-wave (38GHz) Fiber-wireless transmission system using electrical and optical SSB modulation to overcome dispersion effects," *IEEE Photon. Tech. Lett.*, vol. 10, no. 1, pp. 141-143, Jan. 1998.

[31] A. Budman, E. Eichen, J. Schalafer, R. Olshansky, and F. McAleavey, "Multigigabit optical packet switch for self-routing network with subcarrier addressing," in *Proc. IEEE / OSA Optical Fiber Commun. Conf. (OFC)*, San Jose, CA, 1992, paper TuO4.

[32] S. F. Su, A. R. Bugos, V. Lanzisera, and R. Olshansky, "Demonstration of a multiple-access WDM network with subcarrier-multiplexed control channels," *IEEE Photon. Tech. Lett.*, vol. 6, pp. 461-463, Mar. 1994.

[33] H.J. Lee, V. Hernandez, V. K. Tsui, and S. J. B. Yoo, "Simple, polarization-independent, and dispersion-insensitive SCM signal extraction technique for optical switching systems applications," *Electron. Lett.*, vol. 37, no. 20, pp. 1240-1241, Sept. 2001.

[34] J. Yu and G. K. Chang, "A novel technique for optical label and payload generation and multiplexing using optical carrier suppression and separation," *IEEE Photon. Tech. Lett.*, vol. 16, pp. 320–322, Jan. 2004.

[35] G. K. Chang *et al.*, "Enabling technologies for next generation broadband optical access and core networks," *Proc. of IEEE*, vol. 94, no. 5, pp. 892 – 910, May 2006**.**

[36] P. R. Pruncal, "Optically processed self-routing, synchronization, and contention resolution for 1D and 2D photonic switching architectures," *IEEE J. Quantum Electron.*, vol. 29, pp. 600-612, 1993.

[37] M. J. Mahony, D. Simeonidou, D. K. Hunter, and A. Tzanakaki, "The application of optical packet switching in future communication networks," *IEEE Comm. Magazine*, pp. 128-135, Mar. 2001.

[38] J. Spring and R. S. Tucker, "Photonic 2x2 packet switch with input buffers," *Electron. Lett.*, vol. 29, no. 3, pp. 284-285, 1993.

[39] I. Chlamtac *et al.*, "CORD: contention resolution by delay lines," *IEEE J. Select. Areas Commun.*, vol. 14, pp. 1014-1029, June 1996.

[40] D. K. Hunter, W. D. Cornwell, T. H. Gilfedder, A. Franzen, and I. Andonovic, "SLOB: a switch with large optical buffers for optical packet switching," *IEEE J. Lightwave Technol.*, vol. 16, pp. 1725-1736, Oct. 1998.

[41] Z. Haas, "The "Staggering Switch": An electronically controlled optical packet switch," *IEEE J. Lightwave Technol.*, vol. 11, pp. 925-936, May / June 1993.

[42] W. D. Zhong and R. S. Tucker, "Wavelength routing-based photonic packet buffers and their applications in photonic switching systems," *IEEE J. Lightwave Technol.*, vol. 16, no. 10, pp. 1737-1745, 1998.

[43] M. S. Bigelow, N. N. Lepeshkin, and R. W. Boyd, "Observation of Ultraslow Light Propagation in a Ruby Crystal at Room Temperature," *Phy. Rev. Lett.*, vol. 90, no. 11, pp. 113903-1 - 4, Mar. 2003.

[44] C. J. Chang-Hasnain, J. Kim P. C. Ku, and S. L. Chuang, "Variable optical buffer using slow light in semiconducting nanostructures," *Proc. of IEEE*, vol. 91, pp. 1884-1897, 2003.

[45] M. Scalora *et al.*, "Ultrashort pulse propagation at the photonic band edge: large tunable group delay with minimal distortion and loss," *Phy. Rev. E*, vol. 54, no. 2, pp. R1078-1081, Aug. 1996.

[46] S. Lan, S. Nishikawa, H. Ishikawa, and O. Wada, "Design of impurity band-based photonic crystal waveguides and delay lines for ultrashort optical pulses," *J. Appl. Phy.*, vol. 90, no. 9, pp. 4321-4327, Nov. 2001.

[47] Y. Okawachi, M. A. Foster, J. E. Sharping, and A. L. Gaeta, "All-optical slow-light on a photonic chip," *Opt. Express*, vol. 14, no. 16, pp. 2317-2322, Mar. 2006.

[48] K. Y. Song, M. G. Herráez, and L. Thévenaz, "Observation of pulse delaying and advancement in optical fibers using stimulated Brillouin scattering," *Opt. Express*, vol. 13, no. 1, pp. 82-88, Jan. 2005.

[49] J. E. Sharping, Y. Okawachi, and A. L. Gaeta, "Wide bandwidth slow light using a Raman fiber amplifier," *Opt. Express*, vol. 13, no. 16, pp. 6092-6098, Aug. 2005.

[50] S. Yegnanarayanan, P. D. Trinh, F. Coppinger, and B. Jalali, "Compact silicon-based integrated optic time delays," *IEEE Photon. Tech. Lett.*, vol. 9, pp. 634-635, May 1997.

[51] T. Kawanishi, S. Oikawa, K. Higuma, and M. Izutsu, "Electrically tunable delay line using an optical single-side-band modulator," *IEEE Photon. Tech. Lett.*, vol. 14, no. 10, pp. 1454–1456, Oct. 2002.

[52] R. J. Manning, I. D. Phillips, A. D. Ellis, and A. E. Kelly, "10Gbit/s all-optical regenerative memory using single SOA-based logic gate," *Electron. Lett.*, vol. 35, no. 2, pp. 158-159, Jan. 1999.

[53] R. Langenhorst *et al.*, "Fiber loop optical buffer," *IEEE J. Lightwave Technol.*, vol. 14, no. 3, pp. 324-335, Mar. 1996.

[54] E. J. Murphy, T. F. Adda, W. J. Minford, R. W. Irvin, E. I. Ackerman, and S. B. Adams, "Guided-wave optical time delay network," *IEEE Photon. Technol. Lett.*, vol. 8, pp. 545-547, Apr. 1996.

[55] T. Sakamoto, K. Noguchi, R. Sato, A. Okada, Y. Sakai, and M. Matsuoka, "Variable optical delay circuit using wavelength converters," *Electron. Lett.*, vol. 37, no. 7, pp. 454-455, Mar. 2001.

[56] T. Sakamoto, A. Okada, O. Moriwaki, M. Matsuoka, and K. Kikuchi, "Performance analysis of variable optical delay circuit using highly nonlinear fiber parametric wavelength converters," *IEEE J. Lightwave Technol.*, vol. 22, no. 3, pp. 874-881, Mar. 2004.

[57] Y. K. Yeo, J. Yu, and G. K. Chang, "A dynamically reconfigurable folded-path time delay buffer for optical packet switching," *IEEE Photon. Tech. Lett.*, vol. 16, no. 11, pp. 2559–2561, Nov. 2004.

[58] Y. K. Yeo, J. Yu, and G. K. Chang, "Performance of DPSK and NRZ-OOK signals in a novel folded-path optical packet switch buffer," in *Proc. IEEE / OSA Optical Fiber Commun. Conf. (OFC) 2005*, Anaheim, Mar. 2005, paper OWK3.

[59] Y. K. Yeo, A. Chowdhury, J. Yu, and G. K. Chang, "Dynamically Reconfigurable Optical Buffer with Integrated, Simultaneous Wavelength Conversion Capability for Multi-wavelength Packets," in *Proc. Eur. Conf. Optical Communications (ECOC)*, Sept. 2005, paper Th2.4.5.

[60] Y. K. Yeo, J. Yu, and G. K. Chang, "Performance characterization and optimization of high-speed, ON-OFF optical signal reflectors in a folded-path time-delay buffer," *IEEE J. Lightwave Technol.*, vol. 24, no. 1, pp. 365-379, Mar. 2006.

[61] Yong-Kee Yeo, Jianjun Yu, and Gee-Kung Chang, "Performance of 40Gbps Signals in a Folded-Path Optical Delay Buffer," in *Proc. IEEE LEOS Annual Meeting 2005*, Sydney, Australia, Oct. 2005, paper MG2.

[62] A. Ehrhardt *et al.*, "Semiconductor laser amplifier as optical switching gate," *IEEE J. Lightwave Technol.*, vol. 11, pp. 1287-1295, Aug. 1993.

[63] G. Charlet *et al.*, "WDM Transmission at 6Tbit/s capacity over transatlantic distance, using 42.7Gb/s differential phase-shift keying without pulse carver," in *Proc. IEEE /*

OSA Optical Fiber Commun. Conf. (OFC) 2004, Washington, D. C., 2004, paper PDP36.

[64] K. K. Chow, C. Shu, Lin Chinlon, and A. Bjarklev, "Polarization-insensitive widely tunable wavelength converter based on four-wave mixing in a dispersion-flattened nonlinear photonic Crystal fiber," *IEEE Photon. Tech. Lett.*, vol. 17, no. 3, pp. 624-626, Mar. 2005.

[65] C. Xu, X. Liu, and X. Wei, "Differential phase-shift keying for high spectral efficiency optical transmissions," *IEEE J. Select. Topics Quantum Electron.*, vol. 10, no. 2, pp. 281-293, Mar. / Apr. 2004.

[66] K. Kikuchi, C. Zah, and T. P. Lee, "Measurement and analysis of phase noise generated from semiconductor optical amplifiers," *IEEE J. Quantum Electron.*, vol. 27, no. 3, pp. 416-422, Mar. 1991.

[67] M. J. Conelly, "Wideband semiconductor optical amplifier steady-state numerical model," *IEEE J. Quantum Electron.*, vol. 37, no. 3, pp. 439-447, Mar. 2001.

[68] D. Marcuse, "Computer model of an injection laser amplifier," *IEEE J. Quantum Electron.*, vol. QE-19, no. 1, pp. 63-73, Jan. 1983.

[69] M. J. Conelly, *Semiconductor Optical Amplifiers*, Boston: Kluwer Academic Publishers, 2002.

[70] J. P. Gordon and L. F. Mollenauer, "Phase noise in photonic communications systems using linear amplifiers," *Opt. Lett.*, vol. 15, no. 23, pp. 1351-1353, Dec. 1990.

[71] K. Kikuchi and T. P. Lee, "Design theory of electrically frequency-controlled narrow-linewidth semiconductor lasers for coherent optical communication systems," *IEEE J. Lightwave Technol.*, vol. 5, pp. 1273-1276, 1987.

[72] N. A. Olsson, "Lightwave systems with optical amplifiers," *IEEE J. Lightwave Technol.*, vol. 7, no. 7, pp. 1071-1082, Jul. 1989.

[73] E. Desurvire, *Erbium-doped Fiber Amplifiers: Principles and Applications*, New York: Wiley Interscience, 1994.

[74] J. J. O. Pires and J. R. F. da Rocha, "Performance analysis of DPSK direct detection optical systems in the presence of interferometric intensity noise," *IEEE J. Lightwave Technol.*, vol. 10, no. 11, pp. 1722-1730, Nov. 1992.

[75] D. B. Mortimore, "Fiber loop reflectors," *IEEE J. Lightwave Technol.*, vol. 6, no. 7, pp. 1217-1224, July 1988.

[76] H. Mawatari *et al.*, "Reliability and degradation behavior of semiconductor optical amplifiers integrated with spot-size converters," in *Proc. CLEO Pacific Rim '99*, Sept. 1999, paper 1157-1158.

[77] G. P. Agrawal and N. K. Dutta, *Long Wavelength Semiconductor Lasers*, New York: Van Nostrand Reinhold, 1986.

[78] P. De Dobbelaere, K. Falta, S. Gloeckner, and S. Patra, "Digital MEMS for optical switching," *Communications Magazine, IEEE*, vol. 40, no. 3, pp. 88-95, 2002.

[79] A. Himeno, K. Kato, and T. Miya, "Silica-based planar lightwave circuits," *Selected Topics in Quantum Electronics, IEEE Journal of*, vol. 4, no. 6, pp. 913-924, 1998.

[80] N. K. Shankar, J. A. Morris, C. P. Yakymyshyn, and C. R. Pollock, "A 2 x 2 fiber optic switch using chiral liquid crystals," *Photonics Technology Letters, IEEE*, vol. 2, no. 2, pp. 147-149, 1990.

[81] E. J. Murphy *et al.*, "16 x 16 strictly nonblocking guided-wave optical switching system," *IEEE J. Lightwave Technol.*, vol. 14, no. 3, pp. 352-358, 1996.

[82] R. Krahenbuhl *et al.*, "Low-loss polarization-insensitive InP-InGaAsP optical space switches for fiber optical communication," *IEEE Photon. Tech. Lett.*, vol. 8, no. 5, pp. 632-634, 1996.

[83] K. Nashimoto *et al.*, "PLZT Electro-optic waveguides and switches," in *Proc. IEEE / OSA Optical Fiber Commun. Conf. (OFC)*, 2001, paper PD10-1–3.

[84] G. Wenger *et al.*, "A completely packaged strictly non-blocking 8x8 optical matrix switch on InP/InGaAsP," *IEEE J. Lightwave Technol.*, vol. 14, no. 10, pp. 2332-2337, 1996.

[85] S. Yu, M. Owen, R. Varrazza, R.V. Penty, and I. H. White, "High speed optical packet routing demonstration of vertical coupler crosspoint space switch array," in *Proc. CLEO 2000*, May 2000, paper 256-257.

[86] C. Sato *et al.*, "High-speed waveguide switches for optical packet-switched routers and networks," in *Proc. IEEE / OSA Optical Fiber Commun. Conf. (OFC)* Washington, D.C., 2004, paper MF53.

[87] D. K. Hunter *et al.*, "WASPNET: A wavelength switched packet network," *IEEE Commun. Mag.*, pp. 120-129, Mar. 1999.

[88] F. Masetti *et al.*, "Design and performance of a broadcast-and-select photonic switch architecture," in *Proc. Eur. Conf. Optical Communications (ECOC)*, 1996, paper 309-312.

[89] D. Chiaroni *et al.*, "First demonstration of an asynchronous optical packet switching matrix prototype for multiterabitclass routers/switches," in *Proc. Eur. Conf. Optical Communications (ECOC)*, Oct. 2001, paper 60-61.

[90] G. N. Rouskas, "Optical layer multicast: rationale, building blocks, and challenges," *IEEE Network*, pp. 60-65, Jan. 2003.

[91] J. Gripp *et al.*, "Optical switch fabrics for ultra-high-capacity IP routers," *IEEE J. Lightwave Tech.*, vol. 21, no. 11, pp. 2839-2850, Nov. 2003.

[92] D. Klonidis, C. Politi, M. O'Mahony, and D. Simeonidou, "Fast and widely tunable optical packet switching scheme based on tunable laser and dual-pump four-wave mixing," *IEEE Photon. Tech. Lett.*, vol. 16, no. 5, pp. 1412-1414, May 2004.

[93] M. K. Smit and C. Van Dam, "PHASAR-based WDM-devices: Principles, design and applications," *Selected Topics in Quantum Electronics, IEEE Journal of*, vol. 2, no. 2, pp. 236-250, 1996.

[94] Z. Pan *et al.*, in *Proc. IEEE / OSA Opt. Fiber Commun. Conf. (OFC) 2005*, Anaheim, Mar. 2005, paper OTuC8.

[95] A. Araki *et al.*, "Highly scalable optoelectronic packet-switching fabric based on a wavelength-division and space-division optical switch architecture for use in photonic code node," *OSA J. Opt. Networking*, vol. 2, no. 7, pp. 213-228, Jul. 2003.

[96] Y. K. Yeo, J. Yu, and G. K. Chang, "A broadcast and multicast-enabled switch architecture using a gateless channel selection scheme," in *Proc. IEEE / OSA Optical Fiber Commun. Conf. (OFC) 2006*, Anaheim, CA, Mar. 2006, paper OTuG7.

[97] S. Watanabe *et al.*, in *Proc. Eur. Conf. Optical Communications (ECOC)*, Sept. 1998, pp. 85-87.

[98] G. P. Agrawal, *Nonlinear Fiber Optics*, 3rd ed, San Diego, CA: Academic Press, 2001.

[99] K. O. Hill and G. Meltz, "Fiber Bragg grating technology fundamentals and overview," *IEEE J. Lightwave Tech.*, vol. 15, no. 8, pp. 1263-1276, Aug. 1997.

[100] Y. K. Yeo, J. Yu, and G. K. Chang, "A 40Gbit/s Gateless Multicast-Capable Optical Switch Fabric," in *Proc. International Conference on Photonics in Switching*, Greece, Oct. 2006, paper P.01.

[101] S. Diez *et al.*, "Four-wave mixing in semiconductor optical amplifiers for frequency conversion and fast optical switching," *IEEE J. Quantum Electron.*, vol. 3, no. 5, pp. 1131-1145, Oct. 1997.

[102] T. Durhuss, B. Mikkelsen, C. Joergensen, S. L. Danielsen, and K. E. Stubkjaer, "All-optical wavelength conversion by semiconductor optical amplifiers," *IEEE J. Lightwave Tech.*, vol. 14, no. 6, pp. 942-954, June 1996.

[103] R. Ulrich and T. Kamiya, "Resolution of self-images in planar optical waveguides," *J. Opt. Soc. Amer.*, vol. 68, pp. 583–592, 1978.

[104] L. B. Soldano and E. C. M. Pennings, "Optical multi-mode interference devices based on self-imaging: Principles and applications," *IEEE J. Lightwave Technol.*, vol. 13, pp. 615–627, 1995.

[105] T. Zaman, X. Guo, and R. J. Ram, "Integrated Optical Circulator in InP," in *Proc. IEEE Conf. on Lasers & Electro-Optics (CLEO)*, 2005, paper 1321-1323.

[106] C. Deguet *et al.*, "Homogeneous buried ridge stripe semiconductor optical amplifier with near polarization independence," in *Proc. Eur. Conf. Optical Communications (ECOC)*, Nice, France, 1999.

[107] T. Ohtoshi, K. Yamaguchi, and N. Chinone, "Analysis of current leakage in InGaAsP / InP buried heterostructure lasers," *IEEE J. Quantum Electron.*, vol. 25, no. 6, pp. 1369-1375, June 1989.

[108] S. L. Chuang, *Physics of Optoelectronic Devices*, New York: Wiley Interscience, 1995.